Influence of Rare Earth (Y) Ion Substitution on the Structural, Electrical and Magnetic Properties of Cobalt-Zinc Ferrites

By

MITHILA DAS

A thesis submitted in partial fulfillment of the requirement

for the degree of

MASTER OF PHILOSOPHY IN PHYSICS

Department of Physics

CHITTAGONG UNIVERSITY OF ENGINEERING AND TECHNOLOGY

2019

CERTIFICATION

The thesis titled "**Influence of Rare Earth (Y) Ion Substitution on the Structural, Electrical and Magnetic Properties of Cobalt-Zinc Ferrites**" submitted by Mithila Das, Roll No. 15MPHY002F, Session 2015-2016 has been accepted as satisfactory in partial fulfillment of the requirement for the degree of Master of Philosophy (Physics) on April, 2019.

BOARD OF EXAMINERS

1.
Prof. Dr. Md. Mohi Uddin — Chairman (Supervisor)
Department of Physics
Chittagong University of Engineering & Technology
Chattogram-4349.

2.
Dr. Mohammed Nazrul Islam Khan — Member (Co-Supervisor)
Principal Scientific Officer,
Materials Science Division
Atomic Energy Centre Dhaka (AECD)
4, Kazi Nazrul Islam Avenue, Ramna, Dhaka.

3.
Head — Member (Ex-Officio)
Department of Physics
Chittagong University of Engineering &Technology
Chattogram-4349, Bangladesh.

4.
Prof. Dr. Md. Abdur Rashid — Member
Department of Physics
Chittagong University of Engineering & Technology
Chattogram-4349, Bangladesh.

5.
Prof. Dr. Md. Faruque - Uz - Zaman Chowdhury — Member
Department of Physics,
Chittagong University of Engineering & Technology
Chittogram-4349, Bangladesh.

6.
Prof. Dr. Abu Talib Md. Kaosar Jamil — Member (External)
Department of Physics
Dhaka University of Engineering & Technology, Gazipur-1700.

CANDIDATE'S DECLARATION

It is hereby declared that this thesis or any part of it has not been submitted elsewhere for the award of any degree or diploma.

Signature of the Candidate

....……..

(Mithila Das)

Dedicated to my
Supportive husband
Rajib Kanti Biswas

CONTENTS

List of Tables

List of Figures

List of Abbreviation

Energy Loss Per Unit Volume =	P_e
Intrinsic rotational permeability =	μ_r
Wall Permiability =	μ_w
Bohr mgneton =	μ_B
Bragg's angle =	θ
X-ray Density =	ρ_x
Bulk density =	ρ_B
Coercivity =	H_C
Grain diameter =	D
Wall energy =	γ
Direct Current =	DC
Alternating current =	AC
Sintering Temperature =	T_s
Magnetic quantum number =	m_l
Magnetic induction =	B
Hysteresis loss =	P_{hyst}
Exchange integral =	J_{ij}
Miller indices of the crystal planes =	h, k, l
Lattice parameter =	a
Volume of unit cell =	V_{cell}
Cross-sectional area of toroids =	S
Curie temperature =	T_C
DC resistivity =	ρ_{dc}
Dielectric constant =	ϵ'
Diffraction angle =	θ
Face centered cubic =	fcc
Frequency =	f

Rare Earth =	RE
Imaginary part of initial permeability =	μ''
Impedance =	Z
Inductance =	L
Initial permeability =	μ'
Inter planner spacing =	d
Loss factor =	$\tan\delta$
Magnetization =	M
Magnetic field =	H
Field Effect Scanning electron microscopy =	FESEM
Vibrating sample magnetometer =	VSM
Nelson-Riley function =	$F(\theta)$
Number of turns =	N
Boltzmann constant =	K_B
Permeability of in free space =	μ_0
Relative quality factor =	RQF
Absolute temperature =	T
Permeability in free space =	μ_0
Activation Energy =	E_a
Remanent Induction =	M_r
Resistance =	R
Resistivity =	ρ
Saturation magnetization =	M_S
Saturation induction =	M_r
Oersted =	Oe
Susceptibility =	χ
X-ray diffraction =	XRD

Acknowledgements

First and foremost, I would like to thank the Almighty for giving me the strength, knowledge, ability and opportunity to undertake this research study and complete it satisfactorily.

This thesis is the outcome of the efforts and supports of great many people, and my words can never express the gratitude I feel inside. Apart from the academic excursion I made, my life has been deeply enriched and influenced by the association of these compassionate people.

I am deeply indebted to my supervisor Dr. Md. Mohi Uddin, Professor & Head, Department of Physics, Chittagong University of Engineering and Technology (CUET). He guided me all the way with his characteristic wisdom and patience and bore all my limitations with utmost affection. Indeed, without his unfathomable support this work would not have been possible.

I feel a deep sense of gratitude to my co-supervisor Dr. Mohammed Nazrul Islam Khan, Principle Scientific Officer, Materials Science Division, Atomic Energy Centre, Dhaka (AECD), a man known for his altruism and great insights in material science. His penetrating discussions on different aspects of my work had been a great stimulation.

I want to express my sincere gratitude to Md. Ashraf Ali, Assistant professor, Department of Physics, Chittagong University of Engineering and Technology (CUET) for cordial inspiration and suggestions during the progress at each step of this work.

I am grateful to my respectable teacher Prof. Dr. Md. Adbur Rashid, Prof. Dr. Faruque-Uz-Zaman Chowdhury, Prof. Dr. Mohammad Belal Hossen, Swapan Kumar Roy, Nusrat Jahan, H.M.A.R. Maruf, Dr. Animesh Kumar Chakarborty, Syeda Karimunnesa, Dr. Md. Mukter Hossain of Department of Physics, CUET who provided very useful guidance along the way.

I am immensely grateful to all the people at the Materials Science Division of AEC, Dhaka for their lab facilities, Specially Dr. Sheikh Manjura Hoque (CSO and Head, Materials Science Division of AECD). The openhanded and warm supports of Zarna Begum, Alhamra Parveen, Halima Sadia and Nazmunnahar Begum, Md. Kamrul Hasan indeed made this work possible.

I would like to thank Md. Sohel, Siyara Bibi, Trayee Barua, Farhana Sultana, Anny Chowdhury, Priangka Borua due to their friendly co-operation.

Finally, I wish to express my gratitude to my parents, parents-in-laws and spouse had been very patient and understanding and made great sacrifices during the whole course of this study.

Abstract

A series of rare earth Y^{3+} ion substituted Co-Zn ferrites $Co_{0.5}Zn_{0.5}Y_xFe_{2-x}O_4$ (x=0.00 to 0.08 in step of 0.02), have been synthesized by conventional double sintering technique from the oxide powders of Co, Zn, Fe and Y. The XRD, FESEM, EDS, DC resistivity, dielectric measurements, VSM, Curie temperature (T_c) analysis have been used to investigate structural, morphological, electrical and magnetic properties. Single phase of cubic spinel structure has been confirmed up to x<0.06, and a small amount of secondary phase $YFeO_3$ has also been detected for x>0.06. The lattice parameter initially decreases than increase with yttrium concentrations. The FESEM image shows the grains and grains boundaries are distinct and uniformly distributed and the purity has also been endorsed from the EDS spectra. The average grain size decreases at x= 0.02 and then increases with Y substitution. The long range mobility of charge carriers and presence of localized charge carriers with retreat from the Debye-like behavior in the compositions have been explored using electric modulus and impedance. The magnetic strength diminishes owing to existence of magnetic dilution in the A-B interactions subsequent the T_c declines with the x contents. The value of saturation magnetization decreases with increasing Y^{3+} contents that indicates the domain wall motion become tougher due to substitution of foreign ions Y^{3+} that possess larger ionic radius. Therefore, the Y^{3+} substituted $Co_{0.5}Zn_{0.5}Y_xFe_{2-x}O_4$ (x=0.00 to 0.08 in step of 0.02) ferrites with high resistivity and low losses has implications to be used in high frequency and power supply devices applications.

Chapter 1 : General Introduction

1.1 What are the Ferrites?

1.2 History and application of Ferrites

1.3 Literature review and motivation

1.3.5 Overview of present compound

1.3.6 Literature review of Co-Zn Ferrite

1.3.7 Literature review of Yttrium doped Ferrite

1.3.8 Motivation

1.4 Objectives with specific aims

1.5 Arrangement of the Thesis

References

Chapter 1: General Introduction

1.1 What are the Ferrites?

Ferrites are the important class of ceramic magnetic oxides materials which show the property of electrical insulator and magnetic conductor with large number of applications in various fields. Ferrite belongs to a class of ferri-magnetic materials as proposed by L. Neel [1]. It is a type of ceramic compound composed of iron oxide (Fe_2O_3) combined chemically with one or more additional metallic elements. They are the ferri-magnetic materials those can be magnetized or attracted to a magnet, and are electrically nonconductive.

A ferrite is formed by the reaction of ferric oxide (iron oxide or rust) with any metals, including cobalt, zinc, magnesium, aluminum, barium, manganese, copper, nickel, or even iron itself. It is usually described by the formula M (Fe_xO_y), where M represents the metal that forms divalent bonds, such as any of the elements mentioned earlier. For instance, the Cobalt ferrite is of $CoFe_2O_4$, and Zinc ferrite is of $ZnFe_2O_4$.

The general chemical formula of ferrites may be written as AB_2O_4, where A and B represent different metal cation.

1.2. History and Application of Ferrites

The history of ferrites (magnetic oxides) began centuries before the birth of Christ with the discovery of stones that would attract iron. The most plentiful deposits of these stones were found in the district of Magnesia in Asia minor, hence the mineral's name became magnetite (Fe_3O_4). In 1909, Hilpert published the first methodical study of the

relation between the chemical and magnetic properties of a number of binary ion oxides. The relation between the chemical composition, the saturation magnetization and the Curie temperature has been conducted by the Forestier in France and Hilpert and Wille in Germany at around 1928. The discovery of modern ferrites is ascribed to Kato and Takei; who examined some cobalt ferrites in the 1930s. Magnetic oxides were also studied in Japan between 1932 and 1935. Magnetic oxides were studying by Snoek in the Netherlands and Takei in Japan by in 1937 and 1939, respectively. Snoek and his co-workers at the Philips research laboratories in the Netherlands studied one of the most important properties loss factor (loss factor is the loss tangent divided by the permeability), which led Snoek to the development of the first soft ferrites for commercial application. Neel (1948) published the first explanatory theories on the origin of magnetism in ferrites. Guillaud and his co-workers made further examination on the technology of ferrites. The first edition of soft ferrites announced in 1969. By that time, ferrites have become established as an important class of magnetic materials.

Naturally occurring magnetite is a weak ‘hard’ ferrite. ‘Hard’ ferrites possess a magnetism which is essentially permanent. In time, man-made ‘hard’ ferrites with superior properties were developed but producing an analogous ‘soft’ magnetic material in the laboratory proved elusive.

Ferrites have following applications:

- Ferrites have an importance in engineering and technology because they possess spontaneous magnetic moment below the Curie temperature just as iron, cobalt, nickel.
- Due to very low eddy current losses, ferrites are used as a core of coils in microwave frequency devices and computer memory core elements.
- Due to relatively low permeability and flux density compared to iron, ferrites are not suitable for the use in high field and high power applications, such as motors, generators and power transformers, but they can be used in low field and low power applications.
- Ferrites are used as ferromagnetic insulators in electrical circuits.
- Ferrites like ZnO find low frequency applications in timers. They are also used as switches in refrigerators, air conditioners, etc.
- Ferrites are used as magnetic head transducer in recording.

1.3. Literature Review and Motivation

1.3.1. Overview of present compound

The interesting magnetic properties of ferromagnetic spinel of the general formula AB_2O_4 originate mainly from the magnetic interactions between cations with magnetic moments that are situated in the tetrahedral (A) and the octahedral (B) sites. $CoZnFe_2O_4$ has a mixed spinel type of structure. The $ZnFe_2O_4$ is a normal spinel with all Fe^{3+} ions in the B sites and Zn^{2+} ions in the A sites, whereas $CoFe_2O_4$ has an inverse spinel structure

with Co^{2+} ions mainly in the B sites and Fe^{3+} ions distributed almost equally between the A and B sites [2].

Due to the remarkable properties of Co-Zn ferrite such as large magneto-crystalline anisotropy, moderate saturation magnetization, high coercivity, low eddy current loss, high electrical resistivity, chemical stability, high dielectric constant and low manufacturing cost etc. [3,4], they have versatile applications like satellite communication, antenna cores, coolant, ferro-fluids, biosensor, high frequency device, magnetic switches, crystal photonics, chemical drug delivery, read/write head of high speed digital tapes, transformer cores, hyperthermia for cancer treatment, magneto-caloric refrigeration, gas sensor, contrast enhancer in MRI (Magnetic Resonance Imaging) and photo catalysis etc. [5-9]. The electrical and dielectric properties of ferrites depend on several factors such as structural distortion, synthesis procedure, sintering temperature and dopant etc. [10]. Besides several types of synthesis procedures, solid state reaction technique is reasonably good to develop bulk ferrite material [11-15]. The properties of ferrite material dramatically change when partial substitution is made in the iron site of Co-Zn ferrite by some transition metal or rare earth elements.

1.3.2 Literature Review of Co-Zn Ferrite

Meaz et al. [16] have studied $Co_{0.4}Zn_{0.6+X}Ti_XFe_{2-2X}O_4$, (X = 0.1, 0.2, 0.3, and 0.4) ferrites prepared by the standard ceramic method. They have reported the effect of Ti ions substitution on the AC electrical conductivity and dielectric properties at different frequencies and temperatures as well. They found that the electrical conductivity

decreases with increasing Ti ions and mechanism explained using the polaron conduction mechanism. The dielectric constant and dielectric loss have also been explained by the Rezlescu model and Koops phenomenological theory.

Ibrahim et al. [17] have been synthesized the $Co_{0.5-x}Mn_xZn_{0.5}Fe_2O_4$ (x= 0.0 to 0.5 in steps of 0.1) ferrites by the co-precipitation method. They have measured the average crystallite size of about 5–8 nm. The FTIR measurements between 400 and 4000 cm^{-1} have also been confirmed the intrinsic cation vibrations of the spinel structure. The Mőssbauer spectral shows that the substitution of magnetic Mn^{2+} is responsible for the increase in the intensity of the central paramagnetic doublet. The variable sample magnetometer (VSM) illustrates that the Curie point, the coercivity and saturation magnetization decrease with increasing Mn content up to 0.4.

The nickel substituted cobalt zinc nano-ferrites ($Co_{0.6}Zn_{0.4}Ni_xFe_{2-x}O_4$, x=0.2, 0.4, 0.6, 0.8 and 1.0) has been prepared by sol gel method [18]. Two absorption bands in the range of 400-600 cm^{-1} corresponding to the M-O bond in the tetrahedral and octahedral clusters have also been confirmed by the FT-IR. The lattice constant increases with increasing in the nickel substitution, thus altering the unit cell volume. The saturation magnetization rises with increasing Ni concentration up to x=0.4, and a decrease there after. The results have been explained using Neel's collinear two-sub-lattice model and three sub-lattice non-collinear model suggested by Yafet and Kittel. DC resistivity was found to be decreased with increased in temperature due to semiconductor nature of nano-ferrites.

A series of ferrite with a chemical composition of $Co_{0.7}Zn_{0.3}Gd_xFe_{2-x}O_4$ (x = 0.0 to 0.1) were prepared by sol-gel auto-combustion method [19]. Elastic properties were determined from the infrared spectroscopy. Debye temperature, wave velocities, elastic constants were found to be increased with increasing Gd^{3+} substitution. Dielectric properties such as dielectric constant and dielectric loss were studied as a function of Gd^{3+} content and frequency. Dielectric constant decreased with the increase in frequency and Gd^{3+} content and that was explained by the Maxwell-Wagner interfacial polarization which in accordance with Koops phenomenological theory. Real and imaginary part of the impedance was also studied as a function of resistance and Gd^{3+} content. The behavior of impedance is systematically discussed on the basis of resistance-capacitance circuit model.

The effect of Mo doping on the structural and dielectric properties of Co-Zn spinel ferrite has been investigated by Pradhan et al. [20]. The frequency and temperature dependence of dielectric constant are studied and the dielectric dispersion is due to Maxwell-Wagner type polarization in agreement with Koop's phenomenological theory. The contribution of grain and grain boundary at high and low frequency, respectively are evident in the dielectric constant. The variation of dielectric loss tangent with both the temperature and frequency has also been studied.

1.3.3 Literature Review of Yttrium Doped Ferrite

Marija et al. [21] were prepared Yttrium- and indium-doped zinc-ferrite nanoparticles by a co-precipitation method. The influence of doping level on the structure and the

conductivity of the samples was investigated. It was found that the Y-doped zinc-ferrite nanoparticles, with a single spinel phase and a size of a few nanometers, are formed in the whole range of yttrium concentration. However, In-doped zinc-ferrite nanoparticles were formed for all investigated In concentrations, but only the samples of $In_xZn_{1-x}Fe_2O_4$ with $x.\leq 0.15$ are single-phase and at $x \geq 0.20$ a secondary phase - cubic $In(OH)_3$, is observed. The variation of the electrical conductivity with yttrium and indium doping are explained by taking into consideration the different role of these ions in the spinel structure and the electron hopping mechanism.

The $Ni_{0.6}Zn_{0.4}Y_{2x}Fe_{2-2x}O_4$ soft spinel ferrites were prepared via double sintering ceramic route [22]. The influence of Y^{3+} cations on the structural, morphological, electrical and dielectric properties was investigated. X-ray diffraction (XRD) confirmed the formation of single phase spinel structure for $0\leq x\leq 0.06$ and thereafter a small peak of orthorhombic phase ($FeYO_3$) appeared for $x>0.06$. The incorporation of yttrium altered the lattice constant. The variation in lattice constant with respect to the Y^{3+} contents was non-linear in nature and might be attributed to larger ionic radius of Y^{3+} as compare to Fe^{3+} cations and solubility limit of substituted cations. Fourier transform infrared (FTIR) spectra showed two strong absorption bands around 600 cm^{-1} and 400 cm^{-1} that confirmed the spinel structure. The dc electrical resistivity was found to be increased from 5.67×10^5 to 8.48×10^8 Ω cm with the increased of Y^{3+} contents. The dielectric constant and dielectric loss tangent were significantly impeded by increasing the yttrium contents.

Stergiou et al. [23] analyzed the electromagnetic properties of rare earth substituted Ni-Co and Ni-Co-Zn cubic ferrites in the microwave band, along with their performance as microwave absorbing materials. Ceramic samples with compositions of $Ni_{0.5}Co_{0.5}Fe_{2-x}R_xO_4$ and $Ni_{0.25}Co_{0.5}Zn_{0.25}Fe_{2-x}R_xO_4$ (R=Y and La, x=0, 0.02), fabricated using the solid state reaction method. They observed the magneto-crystalline anisotropy reduced and created crystal in-homogeneities in the sample due to rare earth ion substitution. Moreover, permittivity is increased with the increase in Y and La content, due to the enhancement of the dielectric orientation polarization. Regarding the electromagnetic wave attenuation, the prepared ferrites exhibit narrowband return losses (RL) by virtue of the cancellation of multiple reflections, when their thickness equals an odd multiple of quarter-wavelength. Interestingly, the zero-reflection conditions are satisfied in the vicinity of the ferromagnetic resonance.

Franco et al. [24] were synthesized nanoparticles (NPs) of $CoY_xFe_{2-x}O_4$ ($0 \leq x \leq 0.04$) by combustion reaction method in order to study the effect of Y^{3+} ions (x) on the dielectric properties. It was found that the relative dielectric permittivity (έ) measured in a broad range frequency of 100-2 MHz at room temperature. The έ increased with increasing Y^{3+} ions and decreased with the frequency, being 200 (83), and 998 (320) at 100 Hz (1KHz) for x = 0 and x = 0:04, respectively. The experimental data could be fitted to the Cole-Cole model and the relaxation time (τ) was found to be increased with increasing Y^{3+} ions concentration. The results were discussed in the terms of space charge polarization and ions distribution over tetrahedral A-site and octahedral B-sites of the spinel structure

and cation vacancies due to the presence of Y^{3+} ions in the spinel structure of cobalt ferrites.

Sm_2O_3, Gd_2O_3, Ce_2O_3 or Y_2O_3 doped Mn-Zn ferrites have been prepared by traditional ceramic technology [25]. They report a small amount of Sm_2O_3, Gd_2O_3, Ce_2O_3 or Y_2O_3 significantly improve the microstructure and magnetic properties of the studied samples. The single spinel phase structure maintains with the doping of oxides up to 0.07 wt%. A small amount of oxides doping significantly increased the permeability and reduced the coercivity and magnetic core loss. The optimized doping amount for the Sm_2O_3 or Gd_2O_3 is of 0.01 wt%, while for Ce_2O_3 or Y_2O_3 is of 0.03 wt%. A further increase of doping content will lead to reduce the soft magnetic properties. The ferrite sample with 0.01 wt% Sm_2O_3 exhibits the good magnetic properties with permeability, loss, and coercivity of 2586, 316 W/kg, and 24 A/m, respectively, at 200 mT and 100 kHz.

1.3.4 Motivation

The commercial importance of the spinel ferrite is well known, so the interest about these materials generate is no big surprise. The parameters that can sensibly modify the properties of ferrites are method of preparation, composition, substitution, sintering temperature, sintering time and rate of sintering [26, 27]. Strategies will now need to be identified to probe and develop their properties in suitable conditions for technological applications. Even though a few works has been reported on the Co-Zn ferrites, to the best of our knowledge, the effect of Y^{3+} ions substitution on the $Co_{0.5}Zn_{0.5}Fe_2O_4$ ferrites prepared by double sintering method has not been studied yet. So that, in this research we encourage to synthesis the $Co_{0.5}Zn_{0.5}Y_x\ Fe_{2-x}O_4$ (x = 0.00, 0.02, 0.04, 0.06, 0.08)

ferrites using double sintering technique and investigate the variation of structural, morphological, electrical and magnetic properties of Y^{3+} substitution on the Co-Zn ferrites.

1.4 Objectives with specific aims and possible outcome

The main objectives of the present work is to synthesize $Co_{0.5}Zn_{0.5}Y_xFe_{2-x}O_4$ [x=0.0, 0.02, 0.04, 0.06, 0.08] ferrites by using solid state reaction technique.

The objectives of the research works are as follows:

- Preparation of $Co_{0.5}Zn_{0.5}Y_xFe_{(2-x)}O_4$ (x=0.0, 0.02, 0.04,0.06, 0.08) using standard ceramic technique.
- Study of the structural properties of the samples e.g., lattice parameter, density and porosity of the samples.
- Study of the surface morphology by the field emission scanning electron microscopy (FESEM).
- Magnetic properties, i.e., M-H loop, saturation magnetization of the samples by the vibrating sample magnetometer (VSM).
- Determination of AC electrical transport properties, i.e., dielectric constants, AC electrical resistivity, complex impedance spectra by the impedance analyzer.

1.5 Arrangement of the Thesis

The thesis has been configured into six chapters that are as follows:

Chapter 1 : Introduction

In this chapter, introduction of Co-Zn ferrites and organization of thesis have been discussed. Background information to understand the aims and objectives of this investigation and reviews of recent reports has also been discussed.

Chapter 2 **:**Theoretical Background

A brief description of different theories necessary to understand magnetic materials as well as ferrites, classification of magnetism and ferrites, super exchange interaction, mechanism of permeability have been discussed in this chapter.

Chapter 3 **:** Compositions and Method

The details of the sample preparation are presented in this chapter.

Chapter 4 : Experimental technique

Study of different properties of $Co_{0.5}Zn_{0.5}Y_xFe_{(2-x)}O_4$ (x=0.0, 0.02, 0.04,0.06, 0.08) are illustrated in this chapter.

Chapter 5 **:** Results and Discussion

The results of various investigations of $Co_{0.5}Zn_{0.5}Y_xFe_{(2-x)}O_4$ (x=0.0, 0.02, 0.04,0.06, 0.08) ferrites and a brief discussion have been discussed.

Chapter 6 **:** Conclusions

Conclusions of the study are summarized in this chapter.

References

[1] L. Néel, Ann. De Phys. 3 (1948) 137.

[2] F.V .W oude and G.A.Swuatzk y, Phys. Rev. B 4 (1971) 3159.

[3] A. S. Fawzi, A. D. Sheikh and V. L. Mathe, J. Alloys Compd. 493 (2010) 601-608.

[4] C. W. Nan, N. Cai, L. Liu, J. Zhai, Y. Ye and Y. Lin, J. Appl. Phys. 94 (2003) 5930-5936.

[5] A. Thakur, P. Thakur and J. H. Hsu, J. Appl. Phys. 111 (2012) 07A305-1-07A305-3.

[6] S. Singhal, J. Singh, S. K. Barthwal and K. Chandra, J. Solid State Chem.178 (2005) 3183-3189.

[7] K. Muthuraman, S. Alagarsamy, M. A. Banu and V. Naidu, Int. J. Comput. Appl. 32 (2011) 18-27.

[8] D. R. Mane, D. D. Birajdar, S. Patil, S. E. Shirsath and R. H. Kadam, J. Sol-Gel Sci.Technol.58 (2011) 70-78.

[9] M. Hashim, S. Kumar, S. E. Shirsath, R. K. Kotnala, J. Shah and R. Kumar, Mater. Chem. Phys. 139 (2013) 364-374.

[10] K. K. Bharathi and C. V. Ramana, J. Mater. Res. 26 (2011) 584-591.

[11] J. Liu, C. G. Duan, W. G. Yin, W. N. Mei, R. W. Smith and J. R. Smith, J. Chem. Phys.119 (2003) 2812-2818.

[12] A. A. Kadam, S. S. Shinde, S. P. Yadav, P. S. Patil and K. Y. Rajpure, J. Magn. Magn. Mater. 329 (2013) 59-64.

[13] S. B. Patil, R. P. Patil, J. S. Ghodake and B. K Chougule, J. Magn. Magn. Mater. 350 (2014) 179-182.

[14] M. Ishaque, M. A. Khan, I. Ali, H. M. Khan, M. A. Iqbal, M. U. Islam and M. F. Warsi, Ceram. Int. 41 (2015) 4028-4034.

[15] K. S. Nalwa, A. Garg and A. Upadhyaya, Mater. Lett. 62 (2008) 878-881.

[16] T.M. Meaz, S.M. Attia, A.M. Abo El Ata, Journal of Magnetism and Magnetic Materials 257 (2003) 296–305.

[17] Ibrahim Sharifi, H. Shokrollahi, Journal of Magnetism and Magnetic Materials 334(2013)36–40.

[18] Santosh Bhukal, Sandeep Bansal and Sonal Singh, Solid State Phenomena 232 (2015) 197-211.

[19] R.A. Pawar, S.S. Desai, S.M. Patange, S. S. Jadhav, K.M. Jadhav, Physica B: Physics of Condensed Matter 510 (2017) 74-79.

[20] A. K.Pradhan, P. R. Mandal, K. Bera, S. Saha, T. K. Nath, , Physica B: Physics of Condensed Matter 525 (2017) 1-6.

[21] M. Maletin, E. G. Moshopoulou, S. Jankov, S. Rakic and V. V. Srdic, Solid State Phenomena 128 (2007) 101-106.

[22] M. Ishaque, M. A. Khan, Irshad Ali, M. Athair, H. M. Khan, M. A. Iqbal, M.U. Islam, M. F. Warsi, Materials Science in Semiconductor Processing 41 (2016) 508–512.

[23] C. Stergiou, Journal of Magnetism and Magnetic Materials 426 (2017) 629-635.

[24] A. Franco Jr., H.V.S. Pessoni, T.E.P. Alves, Materials Letters 208 (2017) 115-117.

[25] X. C. Zhong, X. J. Guo, S. Y. Zou, H. Y. Yu, Z. W. Liu, Y. F.Zhang and K. X. Wang, AIP ADVANCES 8 (2018) 047807.

[26] A. Verma, T.C. Goel, R. G. Mendiratta, M. I. Alam, Mater. Sci. Eng. B 60 (1999) 156.

[27] B. P. Rao, P.S.V. S. Rao, K.H. Rao, IEEE Trans. Magn. 33 (6) (1997) 4454.

Chapter 2 : Theoretical Background

Chapter 2: Theoretical background

2.1 Magnetism

Magnetism, phenomenon associated with magnetic fields, which arise from the motion of electric charges. This motion can take many forms. It can be an electric current in a conductor or charged particles moving through space, or it can be the motion of an electron in an atomic orbital. Magnetism is also associated with elementary particles, such as the electron, that have a property called spin [1].

On other word, magnetism is one aspect of the combined electromagnetic force. It refers to physical phenomena arising from the force caused by magnets, objects that produce fields and attract or repel other objects.

All materials experience magnetism, some more strongly than others. Permanent magnets, made from materials such as iron, experience the strongest effects, known as ferromagnetism. With rare exception, this is the only form of magnetism strong enough to be felt by people. [2].

2.2 The source of magnetism

All atoms are made up of a nucleus made of protons and neutrons which are held together tightly by a strong force and electrons that are thought of as revolving around the nucleus bound by an electric force. The electron also rotates or spins around its own axis. The spinning of the electrons produce a magnetic dipole. This is one of

fundamental properties of an electron that it has a magnetic dipole moment, i.e., it behaves like a tiny magnet.

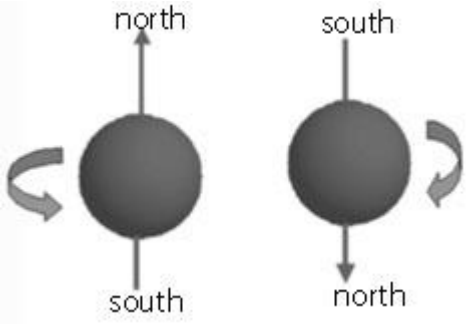

Fig 2.1: Spin of electrons with its own axis

If the majority of electrons in the atom spin in the same direction, a strong magnetic field is produced. The direction of the electrons spin determines the direction of magnetic field. If the same number of electrons in the atom spins in opposite directions, the electron spins will cancels out. Thus, the magnetism will also be cancelled.

Generally, magnetism arises from two sources:

- Electric current.
- Spin magnetic moments of elementary particles.

The magnetic moments of the nuclei of atoms are typically thousands of times smaller than the electrons' magnetic moments. So they are negligible in the context of the magnetization of materials. Nuclear magnetic moments are very important in other contexts, particularly in nuclear magnetic resonance (NMR) and magnetic resonance imaging (MRI).

Ordinarily, the enormous numbers of electrons in materials are arranged such that their magnetic moments (both orbital and intrinsic) cancel out. This is due, to some extent, to electrons combining into pairs with opposite intrinsic magnetic moments as a result of the Pauli Exclusion Principle, or combining into filled subshells with zero net orbital motion. In both cases, the electron arrangement is so as to exactly cancel the magnetic moments from each electron. Moreover, even when the electron configuration is such that there are unpaired electrons and/or non-filled subshells, it is often the case that the various electrons in the solid will contribute magnetic moments that point in different, random directions, so that the material will not be magnetic.

However, sometimes—either spontaneously, or owing to an applied external magnetic field—each of the electron magnetic moments will be, on average, lined up. Then the material can produce a net total magnetic field, which can potentially be quite strong [3].

2.3 Classification of magnetism

Depending upon the magnetic properties like susceptibility, magnetism has been classified into five groups.

1. Diamagnetism
2. Paramagnetism
3. Ferromagnetism
4. Anti-ferromagnetism
5. Ferrimagnetism

2.3.1 Diamagnetism

Diamagnetic materials exhibit a type of magnetism known as diamagnetism. Materials which are weakly repelled to the magnet or external magnetic field are called diamagnetic materials. Diamagnetic materials have all the paired electrons, i.e., the electrons occupy the same orbital of an atom but orbiting and spinning in opposite direction and thus diamagnetic materials have no net magnetic moment or magnetic field strength. When diamagnetic materials are place in the magnetic field of magnet, It creates a slight magnetic field that opposes the external magnetic field. Diamagnetic materials produce the weak magnetic field as the result of change in orbital motion of electrons due to the external magnetic field.

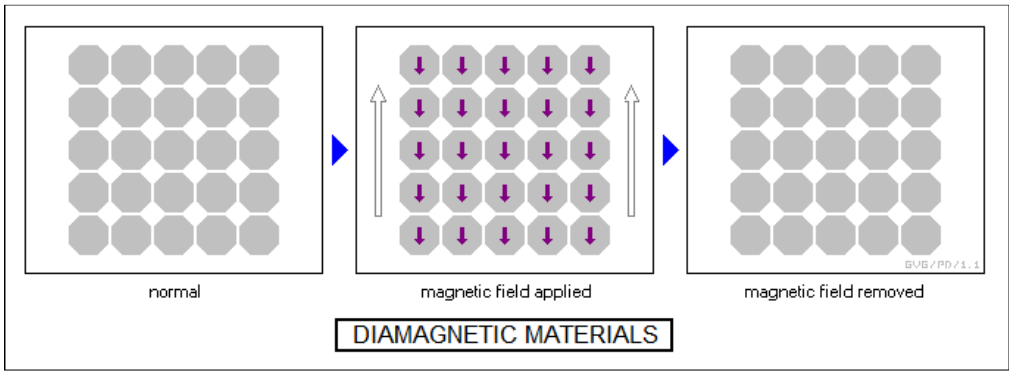

Fig. 2.2: Magnetic ordering of Diamagnetic Materials

In other word, the diamagnetic materials are repelled by a magnet. In presence of non-uniform magnetic field the diamagnetic materials move from stronger to weaker part of the magnetic field. The susceptibility of diamagnetic material is negative. If we plot M vs H, we see:

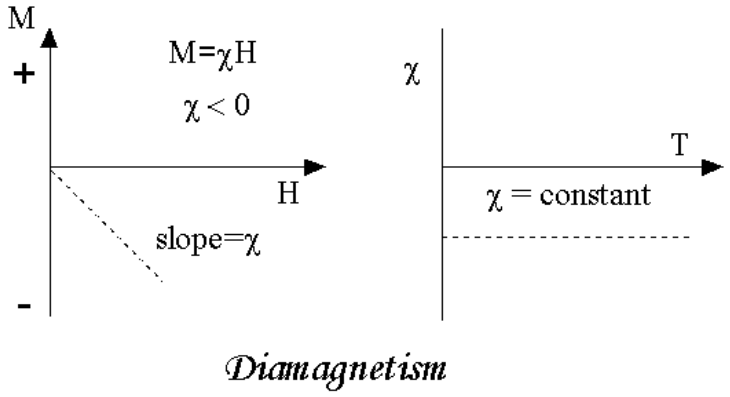

Fig. 2.3: Magnetization vs. applied field and temperature independent susceptibility of Diamagnetic materials.

2.3.2 Para-magnetism

The paramagnetic materials are weakly attracted by a magnet. If the paramagnetic material is placed in external magnetic field then it experiences a weak force. The direction of this force is towards to higher magnetic field. Examples of paramagnetic materials are Aluminum, Chromium, Copper sulphate, Manganese, Palladium, Platinum, Potassium and Tungsten etc.

In absence of external applied field the atomic moments are randomly oriented giving rise to zero magnetization. In the presence of external magnetic field the atomic moments try to align themselves along the field direction giving a positive magnetization.

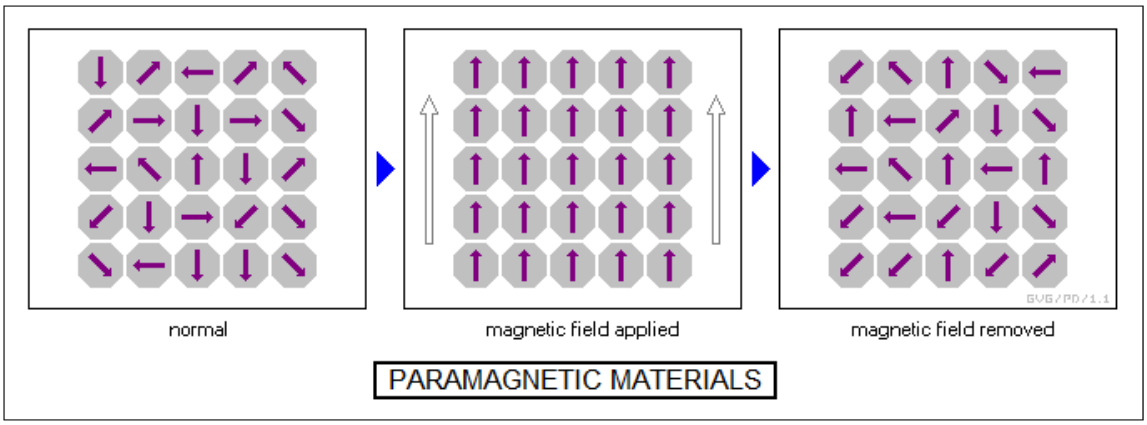

Fig. 2.4: Magnetic ordering of Paramagnetic Materials.

In the presence of small magnetic field the magnetization of paramagnetic material increases with increasing magnetic field linearly. The magnetization of paramagnetic material follows the Curie law i.e. for paramagnetic material

M = C (H / T), where C is the Curie constant. In other words the susceptibility of paramagnetic material varies as $\chi = C / T$

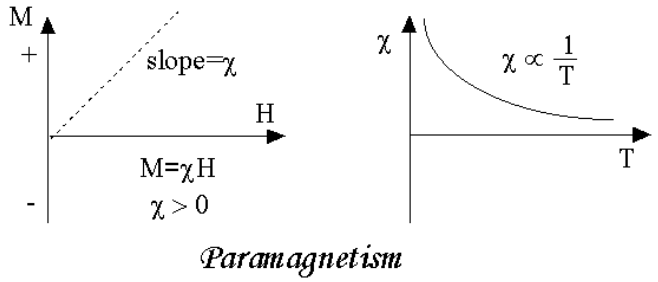

Fig. 2.5: Magnetization vs. applied field and temperature dependent susceptibility of Paramagnetic materials.

2.3.3 Ferromagnetism

Ferromagnetic materials are attracted by a magnet. These materials have very large values of magnetic permeability. Also they have very large degree of magnetization. Examples of ferromagnetic materials are Iron, Cobalt, Nickel etc.

In ferromagnetic materials the atomic magnetic moments are aligned parallel to each other. This is due to strong exchange interaction among atomic magnetic moments. This exchange interaction is very strong in nature but is short range. The dipolar interaction also acts among the atomic magnetic moments. This dipolar interaction is weak but it is long range in nature. The energy of the system can be minimized if it divides itself in a very large number of regions called magnetic domains. In a particular domain, the atomic magnetic moments are aligned along same direction. However the boundary of any magnetic domain cannot be sharp. Between two domains the atomic magnetic moments change their directions gradually over some distance. This region is known as Bloch wall. In this way the system can further minimize the energy. Usually all the domains are oriented randomly. This gives rise to zero magnetization. But the magnetization within each domain still remains non zero.

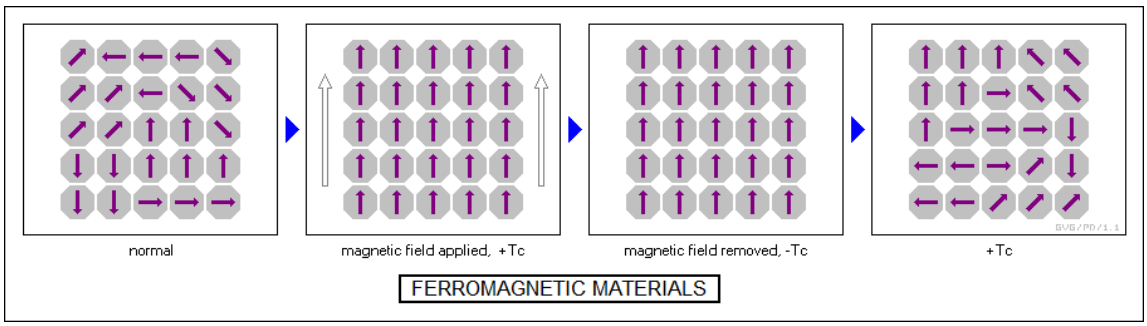

Fig. 2.6: Magnetic ordering of ferromagnetic materials.

A ferromagnetic material becomes paramagnetic at a critical temperature T_C, known as the Curie temperature. At this temperature the thermal energy is sufficiently large to overcome the strong exchange interaction energy among atomic magnetic moments. Because of this reason the ferromagnetic ordering inside the material is disturbed and the material becomes paramagnetic. Above this Curie temperature the susceptibility of the material is expressed by relation

$$\chi = C/(T - T_c)$$

where C is a material dependent constant.

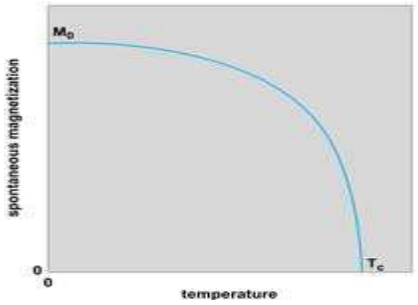

Fig. 2.7: Temperature dependent saturation magnetization

The magnetization of any ferromagnetic material remains unchanged in a constant applied magnetic field at constant temperature. The magnetization of the ferromagnetic material decreases with increasing temperature. The magnetization of the system becomes zero at Curie temperature T_C as shown in Figure 2.7.

2.3.4 Anti-ferromagnetism

In antiferromagnetic materials, the atomic spins are aligned antiparallel to each other as shown in Figure 2.8. The magnitudes of the spins are in same value. Because of this reason the antiferromagnetic material possess zero net magnetization. At a critical temperature, known as the Neel temperature T_N, this antiferromagnetic ordering breaks and the antiferromagnetic material becomes paramagnetic. Well above this temperature the susceptibility of the material is described by relation

$\chi = C/(T + T_N)$; where, C is a material dependent constant.

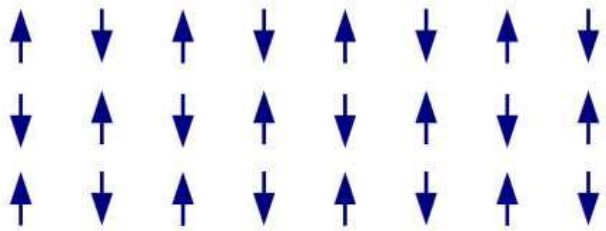

Fig. 2.8: Magnetic ordering of Anti-ferromagnetic Materials

The antiferromagnetic material can be considered to consist of two sub lattices. The magnetization of one sub-lattice is equal and opposite the others. Due to this the net dipole moment or magnetization of antiferromagnetic material is zero in the absence of external magnetic field. If the material is placed in external magnetic field a small magnetization in the direction of the field is produced. This magnetization increases with increasing temperature and become maximum at Neel temperature. The magnetization starts decreasing for any further increase in the temperature.

2.3.5 Ferrimagnetism

Ferrimagnetism is a particular case of anti-ferromagnetism in which the magnetic moments on the A and B lattices while still pointing in the opposite direction have different magnitudes. The magnetization on lattice site A is not completely balanced by the magnetization on lattice site B giving rise to resultant magnetization equal difference between them. It has a critical temperature below which the magnetic moments on both lattice have an orderly arrangement while above the critical temperature the magnetic moments randomly oriented as in paramagnetic substances. Ferromagnetic order was first suggested by Neel to explain the behavior of ferrites. The ferri-magnetics behave on a macroscopic scale very much like ferromagnetic.

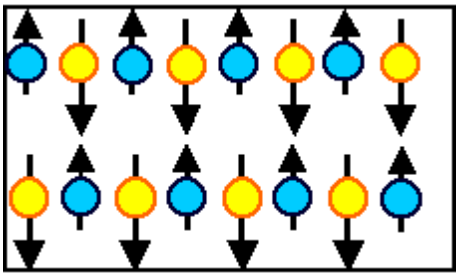

Fig. 2.9: Magnetic ordering of ferromagnetic Materials

Ferrite is a ceramic material formed by reacting metal oxides into a magnetic material. Soft magnetic material is one that can be both easily magnetized and demagnetized, so that it can store or transfer magnetic energy in alternating or other changing wave forms (sine, pulse, square, etc.).

2.4 Hysteresis Loop

An initially un-magnetized material is subjected to a cycle of magnetization. The values of intensity of magnetization M and the magnetizing field H are calculated at every stage and a closed loop is obtained on plotting a graph between M and H as shown in the figure 2.10.

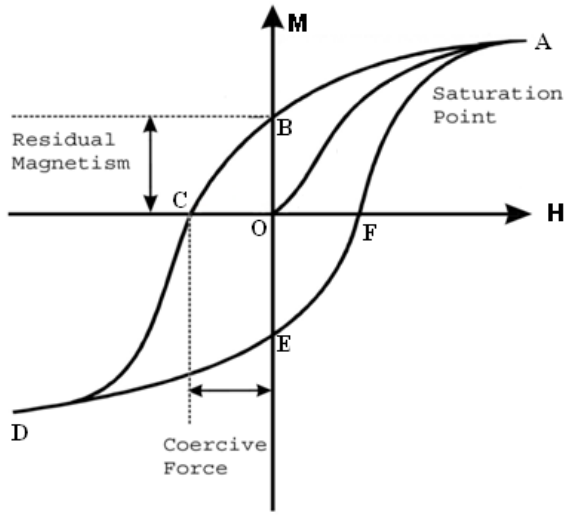

Fig. 2.10: Magnetic hysteresis loop showing coercive force OC, residual magnetism OB, saturation point A

The point 'O' represents the initial un-magnetized condition of the material. As the applied field is increased, the magnetization increases to the saturation point 'A' along 'OA'. As the applied field is reduced, the loop follows the path 'AB'. 'OB' represents the intensity of magnetization remaining in the material when the applied field is reduced to zero. This is called the residual magnetism or remanence. The property of retaining some magnetism on removing the magnetic field is called retentivity. OC

represents the magnetizing field to be applied in the opposite direction to remove residual magnetism. This is called coercive field and the property is called coercivity. When the field is further increased in the reverse direction the material reaches negative saturation point ‘D’. When the field is increased in positive direction, the curve follows path ‘DEF’.

2.5 Magnetic order and domain

The onset of magnetic order in solids has two basic requirements:

(a) Individual atoms should have magnetic moments

(b) Exchange interactions should exit that couple them together [4].

Magnetic moments originate in solids as a consequence of overlapping of the electronic wave function with those of neighboring atoms. This condition is best fulfilled by some transition metals and rare-earths. The exchange interactions depend sensitively upon the inter-atomic distance and the nature of the chemical bonds, particularly of nearest neighbor atoms. When the positive exchange dominates, which corresponds to parallel coupling of neighboring atomic moments (spin), the magnetic system becomes ferromagnetic below a certain temperature T_c called the Curie temperature. The common spin directions are determined by the minimum of magneto-crystalline anisotropy energy of the crystal. Therefore ferromagnetic substances are characterized by spontaneous magnetization. But a ferromagnetic material in the demagnetized state a ferro-magnetic of macroscopic size is divided into a number of small regions called domains, spontaneously magnetized to saturation value and the directions of these

spontaneous magnetization of the various domains are such that the net magnetization of the specimen is zero. The existence of domains is a consequence of energy minimization. The size and formation of these domains is in a complicated manner dependent on the specimen as well as its magnetic and thermal history. When negative exchange dominates, adjacent atomic moments (spins) align antiparallel to each other, and the substance is said to be anti –ferromagnetic bellow a characteristic temperature TN, called the Neel temperature. In the simplest case, the lattice of an anti-ferromagnet is divided into two sub-lattices with the magnetic moments of these in anti-parallel alignment. The result is zero net magnetization. A special case of anti-ferromagnetism is ferrimagnetism. In ferrimagnetism , there are also two sub-lattices with magnetic moments in opposite directions, but the magnetization of the sub-lattices are of unequal strength resulting in a non-zero magnetization and therefore has net spontaneous magnetization. At the macroscopic level of domain structures, ferromagnetic and ferromagnetic materials are therefore similar.

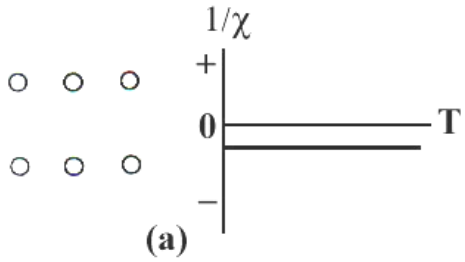

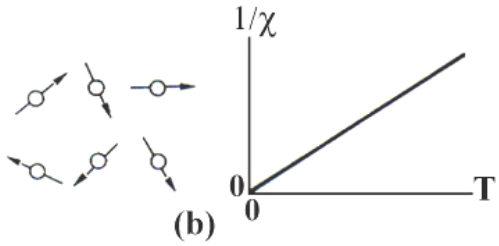

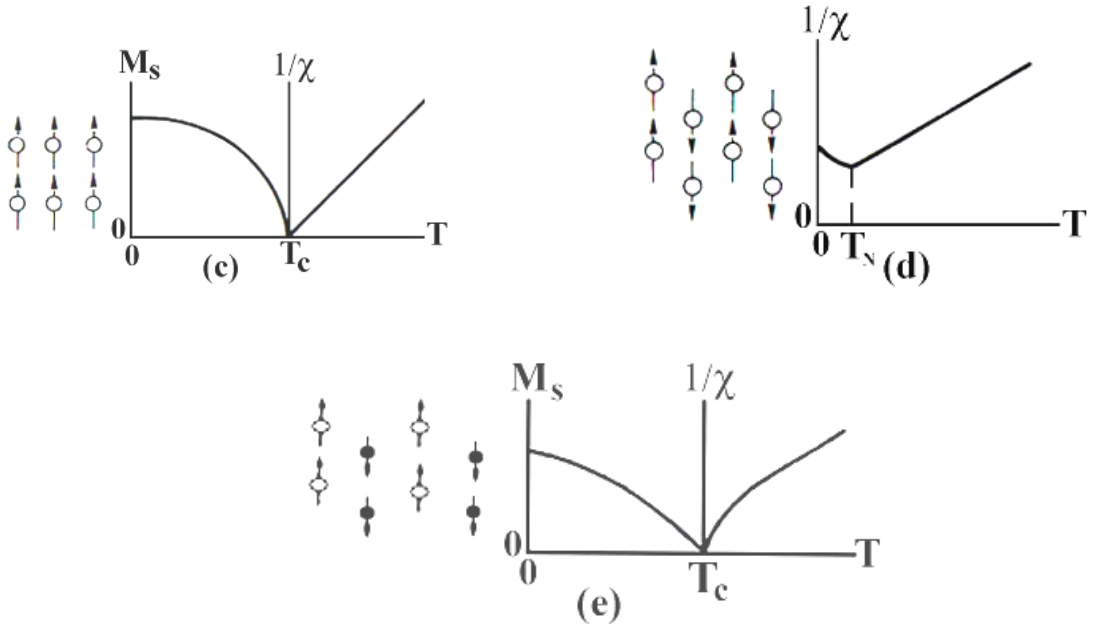

Fig. 2.11: Temperature dependence of the inverse susceptibility for: (a) a diamagnetic material; (b) a paramagnetic material, showing Curie's law behavior; (c) a ferromagnetic material, showing a spontaneous magnetization for $T<T_C$ and Curie-Weiss behavior for $T>T_C$; (d) an antiferromagnetic material; (e) a ferri-magnetic material, showing a net spontaneous magnetization for $T<T_C$ and non-linear behavior for $T>T_C$.

The Curie and Neel temperatures characterize a phase transition between the magnetically ordered and disordered (paramagnetic) states. From these simple cases of magnetic ordering various types of magnetic order exists, particularly in metallic substances. Because of long-range order and oscillatory nature of the exchange interaction, mediated by the conduction electrons, structures like helical, conical and modulated patterns might occur. A useful property for characterizing the magnetic materials is the magnetic susceptibility, χ, defined as the magnetization, M, divided

by the applied magnetic field, H i.e. $\chi = M/H$. The temperature dependence of susceptibility or, more accurately, inverse of susceptibility is a good characterization parameter for magnetic materials, Fig. (e) shows in the paramagnetic region, the variation of the inverse susceptibility with temperature of a ferrite material is decidedly non-linear. Thus the ferrite materials do not obey the Curie-Weiss law, $\chi = C/T - T_c$ [5, 6].

Domain:

A magnetic domain is a region within a magnetic material in which the magnetization is in a uniform direction. This means that the individual magnetic moments of the atoms are aligned with one another and they point in the same direction. When cooled below a temperature called the Curie temperature, the magnetization of a piece of ferromagnetic material spontaneously divides into many small regions called magnetic domains. The magnetization within each domain points in a uniform direction, but the magnetization of different domains may point in different directions. Magnetic domain structure is responsible for the magnetic behavior of ferromagnetic materials like iron, nickel, cobalt and their alloys, and ferri-magnetic materials like ferrite. This includes the formation of permanent magnets and the attraction of ferromagnetic materials to a magnetic field. The regions separating magnetic domains are called domain walls, where the magnetization rotates coherently from the direction in one domain to that in the next domain. The study of magnetic domains is called micro-magnetics.

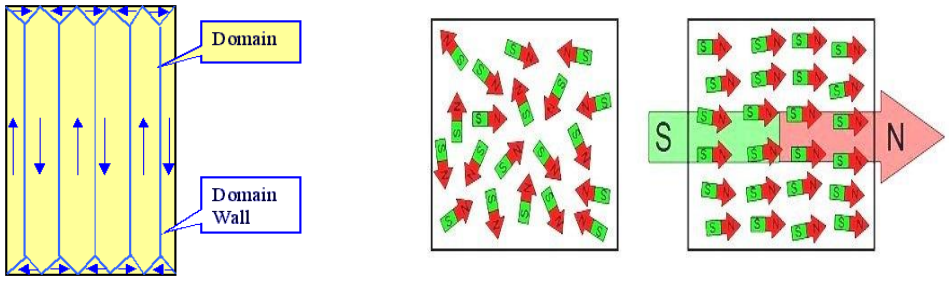

Fig. 2.12: The gradual change in magnetic dipole orientation across a domain wall or boundaries.

Magnetic domains form in materials which have magnetic ordering; that is, their dipoles spontaneously align due to the exchange interaction. These are the ferromagnetic, ferri-magnetic and antiferromagnetic materials. Paramagnetic and diamagnetic materials, in which the dipoles align in response to an external field but do not spontaneously align, do not have magnetic domains.

2.6 Ferrites

Ferrite, a ceramic-like material with magnetic properties that is useful in many types of electronic devices. Ferrites are hard, brittle, iron-containing, and generally gray or black and are polycrystalline i.e., made up of a large number of small crystals. They are composed of iron oxide and one or more other metals in chemical combination.

2.6.1 Types of ferrites

Now a day the term ferrite is used for magnetic oxides whose main constituent is iron oxide. There are different types of ferrites based on the magnetic properties, crystallographic structure, cation distribution.

In terms of the magnetic properties, ferrites are often classified as soft and hard which refers to their low or high coercivity respectively. Exhibiting dielectric properties means that even through electromagnetic waves can pass through ferrites, they do not readily conduct electricity. This also gives them an advantage over irons, nickel and other transition metals that have magnetic properties in many applications because these metals conduct electricity. Ferrites are classified into two categories based on their coercive field strength.

2.6.1.1 Soft ferrite

The ferrites are used in transformer or electromagnetic cores contain nickel, zinc, and/or manganese compounds. They have a low coercivity and are called soft ferrites. The low coercivity means the material's magnetization can easily reverse direction without dissipating much energy (hysteresis losses), while the material's high resistivity prevents eddy currents in the core, another source of energy loss. Because of their comparatively low losses at high frequencies, they are extensively used in the cores of RF transformers and inductors in applications such as switched mode power supplies.

2.6.1.2 Hard ferrites

In contrast, permanent ferrite magnets are made of hard ferrites, which have a high coercivity and high remanence after magnetization. These are composed of iron and barium or strontium oxides. The high coercivity means the materials are very resistant to becoming demagnetized, an essential characteristic for a permanent magnet. They also conduct magnetic flux well and have a high magnetic permeability. This enables these

so-called ceramic magnets to store stronger magnetic fields than iron itself. They are cheap, and are widely used in household products such as refrigerator magnets. The maximum magnetic field B is about 0.35tesla and the magnetic field strength H is about 30 to 160 kilo ampere turns per meter (400 to 2000 Oersteds). The density of ferrite magnets is about 5g/cm^3.

2.6.2 According to Crystal Structure

The ferrites consist dominant compound of Fe_2O_3, are divided into five groups namely Cubic, Spinal, Garnet, Ortho and hexagonal or magneto-plumbite ferrites. These ferrites are distinguished with respect to the molar ratio of Fe_2O_3 to other oxide components present in the ceramic.

2.6.2.1 Cubic

General formula of cubic ferrites is $MO.Fe_2O_3$, where M is divalent metal ion like Mn, Ni, Fe, Co, Zn, Mg, Cd, Cu, etc. Cobalt ferrite like $CoO.Fe_2O_3$ is magnetically hard, but all other cubic ferrites are magnetically soft. Usually, ferrites have spinel structures, often called ferro-spinel because their crystal structure is closely related to that of mineral spinel $MgO.Al_2O_3$. In case of ferrites the divalent ions replace Mg and trivalent ions replace Al. In all cases the ionic radii of the substitution ion should be between about 0.5 to 1Å.

2.6.2.2 Spinel

Ferrites with the formula AB_2O_4, constitute the first group of ferrites, where A and B represent various metal cations like iron. Spinel ferrites are magnetically soft and they

are alternative to metallic magnets such as Fe and layered Fe-Si alloys, but exhibit enhanced performance due to their outstanding magnetic properties [7, 8]. Spinel ferrites have the properties such as high electrical resistivity and low magnetic losses. Two popular ceramic magnets; Nickel-Zinc ferrites, Manganese-Zinc, Cobalt-Zinc etc. ferrites are the major members of the spinel ferrite family. They have been intriguing ceramic materials due to their high electrical resistivity, high magnetic permeability and possible modification of intrinsic properties over a wide spectrum [9].

2.6.2.3 Garnet

Another group of ferrites is the garnet type ferrites. Garnets, unique magnetic ceramics have optical transparency and used in magneto-optical applications [10]. Yttrium iron garnet (YIG) is a synthetic garnet with chemical composition $Y_3Fe_5O_{12}$. Yttrium can be replaced by one of the rare earth ions like La^{3+}, Dy^{3+}, Gd^{3+}, Er^{3+}, etc. with an atomic number greater than 61.

2.6.2.4 Ortho Ferrites

Ortho ferrites possess extremely high velocities of the domain wall motion and it is used in communication techniques, in optical internet, in sensors of magnetic fields and electrical currents, mechanical quantities etc.

2.6.2.5 Hexagonal

In 1952, a new class of ferrites having permanent magnetic properties was discovered. Workers at Philips laboratory at Eindhoven in the Netherlands made

the developments of hexagonal ferrites possible. Hexagonal ferrites (general formula $MFe_{12}O_{19}$ where M is usually Barium Ba, Strontium Sr, Calcium Ca or Lead Pb) have been distinguished due to their high uniaxial magneto-crystalline anisotropy which renders them perfect for permanent (hard) magnet applications [11]. The crystal structure of hexa-ferrite is complex but it can be described as hexagonal with a unique c axis, which is the easy axis of magnetization in the basic structure. Hexagonal ferrites are referred to as hard as the direction of magnetization cannot be changed easily to another axis. Barium ferrite ($BaFe_{12}O_{19}$) and Strontium ferrite ($SrFe_{12}O_{19}$) are the examples of hexagonal ferrites and they have received much interest in recent years because of microwave device applications. Barium hexa-ferrite is especially of interest for use in hybrid microwave devices, monolithic microwave integrated circuits or even as a future replacement for yttrium iron garnet [12] due to its high uniaxial anisotropy and large resistivity. The next generation of magnetic microwave devices (isolators, filters, phase shifters, and circulators and related components) will be planar, self-biased, and low loss, and operate better than today's devices [13].

2.6.3 Classification of Spinel Ferrites according to cation distribution

The chemical composition of a spinel ferrite can be written in general as MFe_2O_4 where M is a divalent metal ion such as Co^{2+}, Zn^{2+}, Fe^{2+}, Mg^{2+}, Ni^{2+}, Cd^{2+}, Cu^{2+} or a combination of these ions. Spinel is an important class of mixed metal oxides, which has the general chemical composition of $A^{2+}B^{3+}O_4^{2-}$. Normally A is a divalent metal such as Mg, Mn, Fe, Zn, Cu etc. and B is trivalent metal such as Ti, Fe, Al and Co. The structure

consists of a cubic closed-packed array of 32 oxide ions, which forms 64 tetrahedral holes and 32 octahedral in a unit cell. There are three main types of spinel [14]:

- Normal spinel structure: $\delta = 1$
- Inverse spinel structure: $\delta = 0$
- Mixed spinel structure: $0 < \delta < 1$.

2.6.3.1 Normal Spinel Ferrites

In normal spinel ferrites all Me^{2+} ions occupy tetrahedral sites i.e. 8 bivalent cations occupy 8 tetrahedral sites and 16 trivalent cations occupy 16 octahedral sites. Structural formula of such ferrites is $Me^{2+}\ [Fe_2^{3+}]\ O_4^{2-}$. Zinc ferrites $Zn^{2+}\ [Fe^{2+}Fe^{3+}]O_4^{2-}$ belong to this class. The normal spinel ferrites are illustrated in Fig. 3.1.

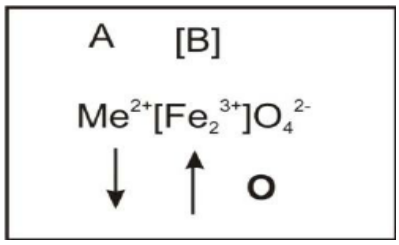

Fig. 3.1: Cation distribution of Normal Spinel ferrites.

2.6.3.2 Inverse Spinel Ferrites

All Me^{2+} are in octahedral sites and Fe^{3+} ions are equally distributed between tetrahedral and octahedral sites in inverse spinel ferrites. The structural formula of these ferrites is $Fe^{3+}\ [Me^{2+}\ Fe^{3+}]\ O_4^{2-}$. Fe_3O_4, $NiFe_2O_4$ and $CoFe_2O_4$ have inversed spinel structure. Inverse spinel ferrites are illustrated in Fig. 3.2.

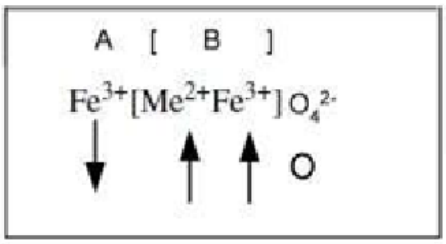

Fig. 3.2: Cation distribution of Inverse Spinel ferrites.

2.6.3.3 Mixed Spinel Ferrites

If the bivalent cations (Me^{2+}) are present on both tetrahedral and octahedral sites, the spinel is mixed spinel structure. Structural formula of such ferrites is $Me_{1-\delta}^{2+}\ Fe_{\delta}^{3+}\ [Me_{\delta}^{2+}\ Fe_{2-\delta}^{3+}]\ O_4$. Mixed spinel ferrites are illustrated in Fig. 2.15.

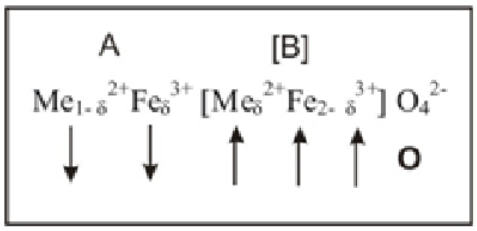

Fig. 3.3: Cation distribution of Mixed Spinel Ferrites.

2.7 Neel Theory of Ferrimagnetism

Consider the simplest case of two sub-lattices, which have anti parallel and unequal magnetic moments. The inequality may be due to:

- Different elements in different sites
- Same elements in different ionic states

- Different crystalline fields leading to different effective moments for ions having the same spin.

Neel's model is briefly outlined below which is based on a simplified model composed of identical magnetic ions divided unequally between the A and B sub-lattices.

Let there be n identical magnetic ions per unit volume with fraction λ located on the A sites and ν (= 1-λ) on the B sites. Let μ_A and μ_B the average moments of A ion and B ion in the direction of field at temperature T.

Though, the A- and B- sites ions are identical, μ_A and μ_B are not because they feel different fields in different sites.

Let $M_A = n\mu_A$ and $M_B = n\mu_B$

The Molecular fields acting on both sub-lattices are

$$Hm_A = \gamma_{AB}(\lambda\alpha M_A - \nu M_B)$$

$$Hm_B = \gamma_{AB}(\beta\nu M_B - \lambda M_A)$$

Where $\alpha = \gamma_{AA}/\gamma_{AB}$ and $\beta = \gamma_{BB}/\gamma_{AB}$

γ_{AA}, γ_{AB} and γ_{BB} are the Weiss constants

The above equations yield the expression for mass susceptibility as follows which is derived from the solving the equations above T_c

$$1/\chi = T/C + 1/\chi_0 + b/T - \theta'$$

Where, $^{1}/_{\chi_0} = \gamma_{AB}\rho(2\lambda\nu - \alpha\lambda^2 - \beta\nu^2)$

$b = \gamma_{AB}^2\rho^2 C\lambda\nu[\lambda(1+\alpha) - \nu(1+\beta)]^2$

$\theta' = \gamma_{AB}\rho C\lambda\nu(2+\alpha+\beta)$

where, ρ density and C is Curie constant for the material. From equating $\chi = 0$ in the above equation for negative value of Weiss constants the Neel temperature can be given as$T_N = \gamma_{AB}\rho\, C/2\left[\alpha\lambda + \beta\nu + \{(\alpha\lambda - \beta\nu)^2 + 4\lambda\nu\}^{1/2}\right]$

The equation for the mass susceptibility actually represents a hyperbola and physically meaningful part of it is shown in Figure. The curve cuts the temperature axis at θp which is called paramagnetic Curie point. It is in good agreement with the experimental observed susceptibility v/s temperature which differentiates ferri-magnetics form ferro-magnetics.

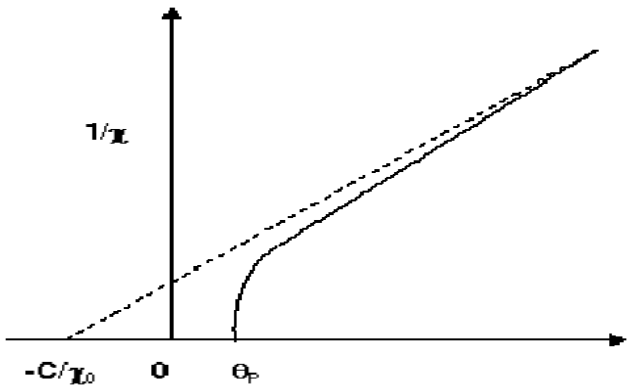

Fig. 2.16: Variation of inverse susceptibility with Temperature (K) below T_c.

In the ferri-magnetic region each sub-lattice is spontaneously magnetized by the molecular field acing on it. But the two sub-lattice magnetizations are opposite to each other. The observable magnetization is $|M| = |MB| - |MA|$

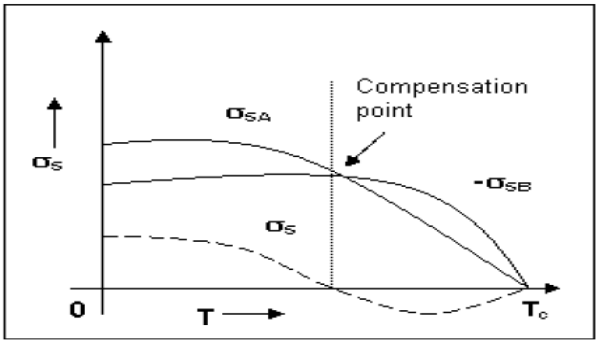

Fig. 2.17: Anomalous magnetization v/s temperature curve for ferri-magents.

Each sub-lattice magnetizations are governed by the same relation as ferro-magnetics. In terms of specific magnetization, they are given by

$$\frac{\sigma_A}{\sigma_0} = B\left(J, \frac{\mu_H H_{mA}}{Kt}\right)$$

$$\frac{\sigma_B}{\sigma_0} = B\left(J, \frac{\mu_H H_{mB}}{Kt}\right)$$

Where, k is Boltzmann constant and B is Brillouin function.

These sub-lattice magnetizations will have different temperature response because effective molecular field acting on them are different. This suggests the possibility of having anomalous net magnetization versus temperature curves. For most ferri-magnetics the curves show simple behavior but in few cases there may be a compensation point or a maximum in the curve at some temperature. The shape of the

curve depends on γ, λ, ν and α. There is an interesting possibility of the net magnetization reversing its sign. The situation is depicted in Figure where, at some temperature below T_c both the $|M_B| = |M_A|$ and of opposite sign. So M disappears at that point, which is called compensation point. Gorter [13] observed these types of behavior in Li-Cr system. Let's see how beautifully the Neel model explains the observed features of spinel ferrite. Take the case of Nickel ferrite, where the magnetic moments of Ni and Fe are reasonably different. It gives observed magnetic moment 2.3 μ_B. Now let us predict the cation distribution for it.

According to Neel model, if a normal structure is assumed the moment comes out is 8 μ_B as follows:

$$M = |M_B| - |M_A| = [2.5\mu_B(Fe)] - [1.2\mu_B(Ni)]$$

and an inverse will give 2 μ_B as follows

$$M = |M_B| - |M_A| = [1.5\mu_B(Fe)] - [1.2\mu_B(Ni)] - [1.5\mu_B(Fe)] = 2\mu_B$$

Later is near to observed value which allows us to term the Nickel ferrite as an inverse structure. A nominal observed difference is always present in every cases and may be ascribed to the following factors

- g factor may not be exactly 2
- the structure may not be completely inverse
- particular ion may have different moments when in different sites.

Shortcomings of the Neel model:

1. Saturation magnetization values in many ferrites are found to be much lower than those predicted by Neel model.
2. Some M v/s T curves have finite slopes at 0 K and cannot be explained by Neel model.
3. It is based on the assumption that strong negative AB interaction predominates over AA and BB interactions, which is not applicable to each and every case.

2.8 Mechanism of Permeability

Initial permeability describes the relative permeability of a material at low values of B. The maximum value for μ in a material is frequently a facing of between 2 and 5 or more above its initial value. Low flux has the advantage that every ferrite can be measured at that density without risk of saturation. This consistency means that comparison between different ferrite is easy.

For high frequency application, the desirable property of a ferrite is the high initial permeability with low loss. The present goal of the most of the recent ferrite researches is to fulfill this requirement. The initial permeability μ_i is defined as the derivative of induction B with respect to the initial field H in the demagnetization state.

$$\mu_i = \left|\frac{dB}{dH}\right|; H \to 0, B \to 0$$

At microwave frequency and also in low anisotropic materials, dH and dB may be in different directions. The permeability is thus a tensor character. In the case of amorphous materials containing a large number of randomly oriented magnetic atoms the permeability will be scalar. As we have

$$B = \mu_0(H + M)$$

and susceptibility

$$\chi = \frac{dM}{dH} = \frac{d}{d\chi H}\left(\frac{B}{\mu_0} - 1\right) = \frac{1}{\mu_0}(\mu - 1)$$

The magnetic energy density

$$E = \frac{1}{\mu_0}\int H.dB$$

For time harmonic fields H = H_0 Sin wt. The dissipation can be described by a phase difference between B+ and B.

Permeability is namely defines as the proportional constant between the magnetic field induction B and applied intensity H:

$$B = \mu H$$

If a magnetic material is subjected to an AC magnetic field as given below:

$$H = H_0 e^{i\omega t}$$

Then it is observed that the magnetic flux density B experiences a delay. The delay is caused due to presence of various losses and is thus expressed as

$$B = B_0 e^{i(\omega t - \delta)}$$

Where δ is the phase angle and marks the delay of B with respect to H. The permeability is then given by

$$\mu = \frac{B}{H} = \frac{B_0 e^{i(\omega t - \delta)}}{H_0 e^{i\omega t}} = \frac{B_0 e^{-i\delta}}{H_0} = \frac{B_0}{H_0}\cos\delta - i\frac{B_0}{H_0}\sin\delta$$

$$\mu = \mu' - \mu''$$

Where, $\mu' = \frac{B_0}{H_0} cos\,\delta$

$$\mu'' = i\frac{B_0}{H_0}\sin\delta$$

The real Part μ' of complex permeability μ represent the component of B induction which is in phase with H, so it corresponds to the normal permeability. If there is no losses, we should have μ = μ', The imaginary part μ'' corresponds to that part of B which is delayed by phase angle δ from H arranging up to 90° from H . The presence of such a component requires a supply of energy to maintain the alternating magnetization regardless of the origin of delay. The ratio of μ' to μ'' as is evident from equation gives:

$$\frac{\mu'}{\mu''} = \frac{\frac{B_0}{H_0} sin\,\delta}{\frac{B_0}{H_0}\cos\delta} = \tan\delta$$

This tan δ is called the loss Factor or loss tangent. The Q-Factor or quality factor is defined as the reciprocal of this loss factor, i.e.

$$Q = \frac{1}{\tan\delta}$$

And the relative quality factor

$$\frac{\mu'}{\tan\delta} = \mu' Q$$

The behavior of μ' and μ" versus frequency is called the permeability spectrum. The initial permeability of a ferromagnetic or ferromagnetic substance is the combined effects of the wall permeability and rotational permeability mechanisms.

References

[1] https://www.britannica.com/science/magnetism.

[2] https://www.livescience.com/38059-magnetism.html

[3] Magnetism and Magnetic Materials, J. M. D. COEY-2009 www.cambridge.org/9780521816144.

[4] A.K.M Abdul Hakim, Ph.D Thesis, BUET,1995.

[5] R.Valenzuela, Magnetic Ceramics, Cambridge University Press, Cambridge (1994).

[6] V.K Mittal, P.Chandramohan, Santanu Bera, M.P Srinivasan, S.Velmurugan, S.V.Narasimhan , JSSC 10.10161 (2005).

[7] E. C. Snelling, "Soft Ferrites: Properties and Applications", 1st Edition, Iliffe Books Ltd., London, 1969.

[8] M. Sugimoto, Journal of American Ceramic Society, 82-2 (1999) 269.

[9] L. L. Hench, J. K. West, "Principles of Electronic Ceramics", John Wiley & Sons, 1990.

[10] A. J. Moulson, J. M. Herbert, "Electro-ceramics: Materials, Properties, Applications", 1st Edition, Chapman & Hall, London, 1990.

[11] A. L. Stuijts, G. W. Rathenau, G. H. Weber, Philips Technical Review, 16 (1954) 141.

[12] H.C. Fang, C.K. Ong, Journal of Applied Physics, 86-4 (1999) 2191.

[13] H. W. Gorter, Philips Res. Repts. 9 (1954)295.

[14] Harris, V. G. Chen, Z. Chen, Y. Yoon, S. Sakai, T. Gieler, A. Yang, A. He, Y. Ziemer, K. S. Sun, N. X. Vittoria, Carmine, Journal of Applied Physics, 99-8 (2006) 08M911.

[15] M. G. Naseri and E. B. Saion, Crystalization in spinel ferrite nanoparticles, www.intechopen.com, pp. 352-353, 2012.

Chapter 3 : Compositions and Method

3.4 Introduction

3.5 Solid State Reaction Method

3.6 Sample preparation

3.3.8 Oxide of Raw Materials

3.3.9 Weighting by stoichiometric ratio

3.3.10 Mixing by milling

3.3.11 Pre-sintering

3.3.12 Milling

3.3.13 Different shapes by pressing

3.3.14 Final Sintering

References

Chapter 3: Compositions and Method

3.1 Introduction:

Today one of the challenges faced by materials scientists is the synthesis of materials with desired stoichiometric composition, structure and various properties of prepared materials for specific applications. The rational synthesis of materials requires the knowledge of different aspects which are important for the synthesis of desired materials such as crystal chemistry, phase equilibrium reaction kinetics etc. The choice of synthesis methods is an important issue to determine the physio-chemical properties of many materials. There are number of synthesis methods such as solid state reaction [1], chemical co-precipitation [2], sol-gel auto combustion [3], hydrothermal [4], micro-emulsion [5] etc. which can be employed for the synthesis of the ferrite materials. Thus, the selection of the synthesis method is a vital to control the composition, structure, morphology and many of the properties of a prepared material under study.

3.2 Solid state reaction method

Solid-state synthesis methods are the most widely used. This method involves mixing of raw materials and can take place with both wet and dry processes. An aqueous suspension, agitator mill, or vibration drum is used in wet mixing methods. This method is extremely effective but requires energy for dewatering and drying. Dry mixing is done either by grinding and mixing in a drum or ball mill.

This method depends on the solid state inter-diffusion between the raw materials. Solids do not usually react at room temperature over normal time scales. Thus it is necessary to heat them at higher temperatures for the diffusion length $(2D_t)^{1/2}$ to exceed the particle size, where *D* is the diffusion constant for the fast-diffusing species, and t is the firing time. The ground powders are then calcined in air or oxygen at a temperature above 1000℃. For some time, this process is continued until the mixture is converted into the correct crystalline phase. The calcined powders are again crushed into fine powders. The pellets or toroid shaped samples are prepared from these calcined powders using die-punch assembly or hydrostatic or iso-static pressure. Sintering is carried out in the solid state, at temperature ranging 1000-1500℃, for times of typically 1-40 h and in various atmospheres (e.g. Air, O_2 and N_2) [6-8].

The general solid state reaction leading to a ferrite MFe_2O_4 may be represented as

$$MO + Fe_2O_3 \rightarrow MeFe_2O_4;$$

where M is the divalent ions.

3.3 Sample preparation

The $Co_{0.5}Zn_{0.5}Fe_{2-x}Y_xO_4$ (x = 0.00, 0.02, 0.04, 0.06 and 0.08) were prepared by standard solid state reaction technique. Appropriate amount of commercially available high purity powders of Co_3O_4 (99.9%), ZnO (99.9%), Y_2O_3 (99.95%) and Fe_2O_3 (99.9%) were used as the raw materials. The exact amounts of compounds were calculated for each composition. Using those raw materials were weighed and mixed thoroughly by hand milling. During hand milling, few drops of acetone were added to increase the degree of

mixing. The mixture was calcined at 650ºC for 4 hours. The calcined powder again was crashed into fine powders. Then added 1wt% polyvinyl alcohol (PVA) as a binder and uni-axially pressed for the preparation of pellet or disc shaped and toroid shaped samples at a pressure of 10 kN/cm^3 and15 kN/cm^3, respectively. The compact sintered at temperatures 1100℃ in a muffle furnace. During sintering the samples were heated /cooled in 5℃/min heating and cooling rates. It was expected that sintering temperatures are produced samples of various surface morphology, electric and magnetic properties.

The main step of this process is shown in a flow chart below:

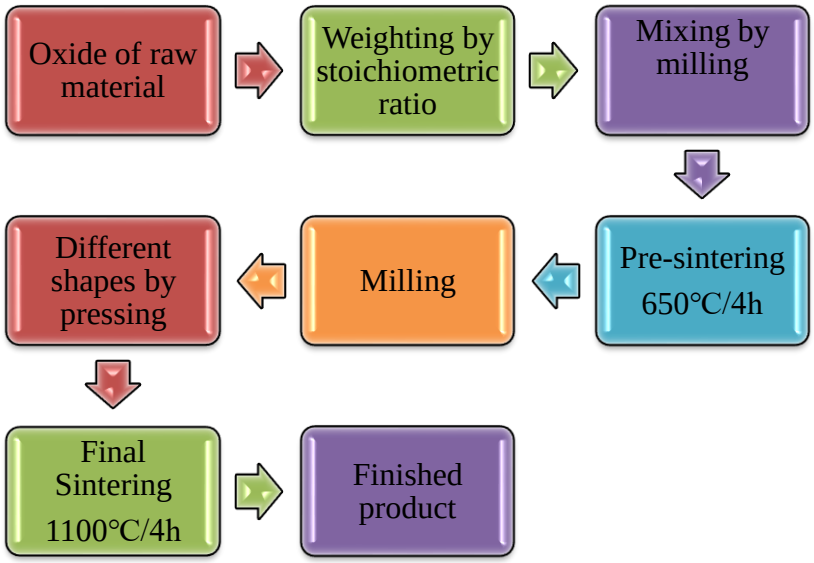

3.3.1 Oxide of raw materials

The samples of Y^{3+} substituted Co-Zn ferrites with a basic composition of $Co_{0.5}Zn_{0.5}Y_xFe_{2-x}O_4$ ($0.00 \leq x \leq 0.08$; in a step of 0.02) were synthesized by solid state reaction technique. The raw materials were Cobalt oxide (Co_3O_4); Zinc oxide (ZnO);

Iron oxide (Fe_2O_3); Yttrium oxide (Y_2O_3) with a purity of 99.98% obtained from E. Merck Germany.

3.3.2 Weighing by stoichiometric ratio

The weight percentages of the individual oxides were calculated using the solid state reaction.

Table 3.1: Weight percentage for 20gm of $Co_{0.5}Zn_{0.5}Y_xFe_{2-x}O_4$ with varying x.

x	**Co_3O_4**	**ZnO**	**Y_2O_3**	**Fe_2O_3**
0.00	3.337	3.3832	0	13.279
0.02	3.328	3.373	0.187	13.110
0.04	3.3191	3.3647	0.3735	12.942
0.06	3.3100	3.3555	0.5587	12.7756
0.08	3.3011	3.3465	0.7429	12.6093

3.3.3 Mixing by milling

The raw materials in required stoichiometric proportions were weighed first and then thoroughly mixed by hand milling using ceramic mortar and pestle to produce fine powers of mixed constituents for 6 hours.

3.3.4 Pre-sintering

The powder palletized by using only hand pressure in a hydraulic press and then transferred to a porcelain crucible for pre sintering in a constant temperature of 650°C for 4 hours. Pre-sintering of the materials was performed in a furnace named

Nabertherm at Material Science division, AECD. The cooling and heating rates were 5°C/min. The pre-sintering is very crucial because in this step of sample preparation of ferrite is form its component oxides. The solid-state reactions, leading to the formation of ferrites, actually achieved by counter diffusion. This means that the diffusion involves two or more species of ions, which more in opposite direction initially across the interface of two contacting particles of different component oxides. During the pre-sintering stage, the reaction of Fe_2O_3 with metal oxide of MO or $\acute{M}_2O_3$ (where M is the divalent and $\acute{M}$ is the trivalent metal atom) takes place in the solid state to form spinel ferrite according to the reactions:

$$MO + Fe_2O_3 \rightarrow MFe_2O_4 \text{ (spinel)}$$

$$2\acute{M}_2O_3 + 4Fe_2O_4 \rightarrow 4\acute{M}Fe_2O_4 + O_2$$

3.3.5 Milling

Besides reducing the particle size to ≈1micron, grinding also eliminates intra-particle pores and homogenizes the ferrite by mixing. To promote successful sintering in the next steps, the powder must be well characterized after grinding with respect to such factors as particles size and distribution, particle shape, homogeneity, absorbed gases, impurities and intra particle porosity. Iron contamination due to continuous wear of the mill wall and steel ball need to be closely watched and minimized.

3.3.6 Different shapes by pressing

Now to the ground homogeneous powder polyvinyl alcohol is added as a binder. Pressing the powder into compacts of desired shapes is done either by conventional

method in a die-punch assembly or by hydrostatic or isocratic compaction. We made use of the former one. Pressing a uniformly dense body by this method is difficult owing to the friction gradient of the powder at the walls of the die and between the particles themselves. This problems is somewhat overcome by the addition of external and internal lubricant to the powder such as stearic acid. Mainly, we made two types of samples- tablet and toroid. Specimen was prepared by a hydraulic press with a pressure of $10kN/cm^3$ and $15kN/cm^3$ for tablets and toroids, respectively.

3.3.7 Final Sintering

The tablets and toroids transferred to a porcelain crucible for final sintering in temperature of 1050℃ and 1100℃ for 4 hours. Powder sintering involves raising the temperature of the green compact, (pressed powder part), to a certain level and keeping it at that temperature for a certain amount of time. The sintering temperature is usually between 70% and 90% of the melting point of the powder metal. This will cause bonding mechanisms to occur between powder particles pressed together in the compact. Bonding within the green compact is weak and this pressed un-sintered part usually has just enough structural integrity to be handled. Bonding that occurs during sintering greatly strengthens the part.

Sintering involves heating the powdered metal compacts in vacuum or a reducing gaseous atmosphere to a temperature that is below the melting point of the primary constituent of the material. The metallic particles metallurgical bond and alloying take place via diffusion processes. Changes occur during sintering, including changes in size, configuration, and the nature of pores. Commonly used atmospheres for sintering are

hydrogen, carbon monoxide, and ammonia. Sintering operation ensures that powder particles are bonded strongly and that better alloying is achieved [9].

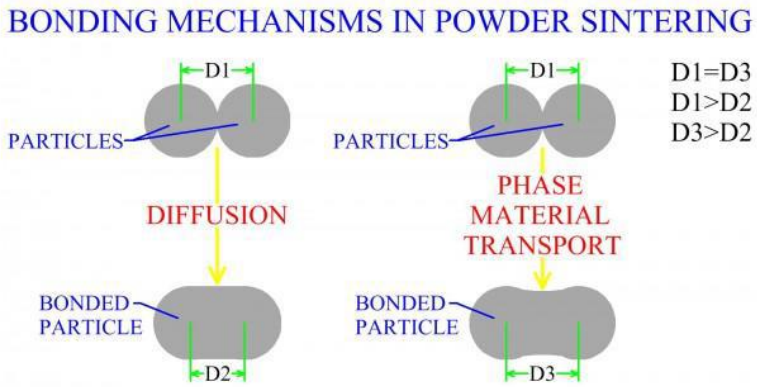

Fig. 3.1: Bonding Mechanism in powder sintering

This is a heat treatment by which a mass of compacted powder is transformed into a dense object. The thermodynamic driving force is the reduction in the specific surface area of the particles. The sintering mechanism usually involves atomic transport over particle surfaces, along grain boundaries and through the particle interiors. Sintering may result in densification, depending on the predominant diffusion pathway. It is used in the fabrication of metal and ceramic components, the agglomeration of ore fines for further metallurgical processing and occurs during the formation of sandstones and glaciers. Sintering must fulfill three requirements

- to bond the particles together so as to impart sufficient strength to the product
- to density the grain compacts by eliminating the pores and
- To complete the reactions left unfinished in the pre-sintering step.

The principle goal of sintering is the reduction of compact porosity. Sometimes the initial spaces between compacted grains of ceramics are called “voids”, to differentiate term from the isolated spaces pores, which occur in the final stages of sintering. The sintering process is usually accompanied by other changes within the materials, some desirable and some undesirable. The largest- changes occur in:

- Binding the particles together so as to impart sufficient strength to the products.
- Making homogeneous distribution of grain number, grain size and shape.

Sintering can be enhanced by the presence of a liquid phase. The liquid phase can form directly from the elements when the sintering temperature is between the melting point of the matrix and the additive, by the melting of eutectic phase mixtures, which form by diffusio. The liquid flows between the particles filling pores and causing densification by capillary action and through the provision of a fast diffusion pathway.

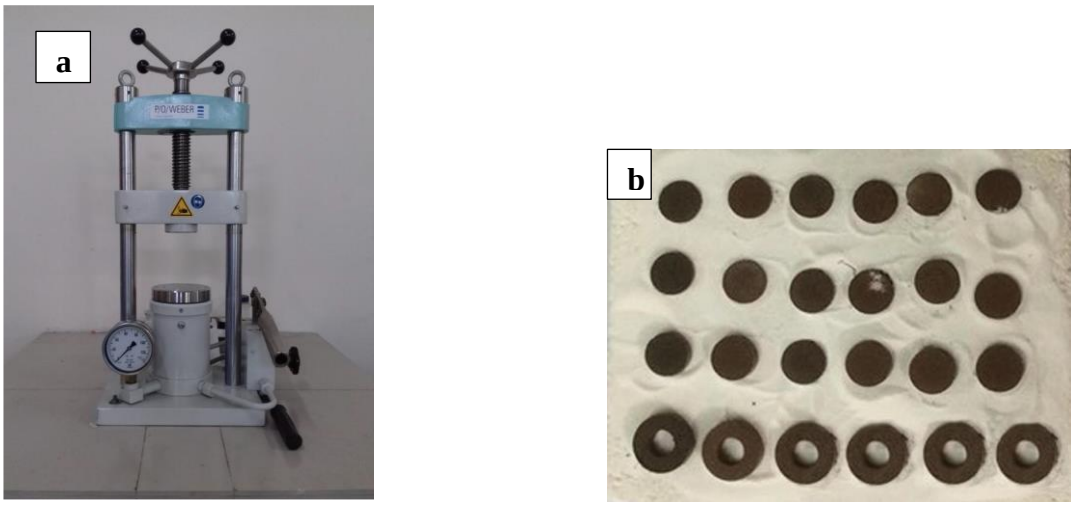

Fig. 3.2: a) Hydraulic press used to make different shaped samples, **b)** Ring and disk shape samples.

References

[1] A. Gruskeva, J. Slama, R. Dosoudil, M. Usakova, V. Jancarik, E. Usak, J. Magn. Magn. Mater. 320 (2008) 860-864

[2] A. A. Pandit, S. S. More, R. G. Dorik, K. M. Jadhav, Bull. Mat. Sci. 26(2003)17.

[3] M. George, A. M. John, S. S. Nair, P. A. Joy, M. R. Anantharaman, J. Magn. Magn. Mater. 302 (2006) 190-195.

[4] J.Wang, Mater. Sci. Eng. B 127 (2006) 81.

[5] N. Moumen, M. P. Pileni, Chem. Mater. 8(1996)1128–1134.

[6] B. D. Cullity, Introduction to Magnetic Materials, Addison-Wiseley Publishing Company, Inc, California(1972)

[7] R. J .Brook, Sintering: An Overview, concise Encyclopedia of Advanced Ceramic Materials, Pergamon Press, Oxford, PP.438(1991)

[8] P. Reijnen, Science of Ceramisc, Academic Press, London (1967)

[9] K. O. Low, S. R. Frank, J. Magn. Magn. Mater., 246 (2002) 30 - 35.

Chapter 4 Experimental Techniques

4.4 Structural and Physical properties measurement

4.1.4 X-ray diffraction technique

4.1.1.4 Lattice constant and Identify Phase

4.1.1.5 X-ray Density and Bulk Density

4.1.1.6 Porosity

4.1.5 Field Effect Scanning Electron Microscope (FESEM)

4.1.6 Energy Dispersive Spectrometer (EDS)

4.5 Magnetic properties measurement

4.2.4 Principle of Vibrating Sample Magnetometer (VSM)

4.2.5 Permeability Measurement

4.2.6 Curie Temperature Measurement

4.6 Electrical Properties Measurement

4.3.5 Electrical Conductivity & Resistivity

4.3.6 Dielectric Relaxation

4.3.7 Electric Modulus

4.3.8 Impedance Spectroscopy

References

Chapter 4: Experimental Techniques

4.1 Structural and Physical properties measurement

The study of structural and physical properties of a ferrite involve with the crystal structure, grain size, lattice parameter, density, purity, phase identification etc. To determine these properties of the ferrites the XRD, FESEM, EDS measurement explained have been discussed.

4.1.1 X-ray diffraction technique

X-rays are electromagnetic radiation discovered by Rontgen in 1895. In electromagnetic spectrum these rays occupy the region between gamma rays and ultraviolet rays. X-ray photons are highly energetic having energy in range of 100 eV to 100 keV. X-ray diffraction is a very useful and non-destructive technique that provides detailed information about the crystal structure of a crystalline material.

The peaks in an X-ray diffraction pattern are directly related to the atomic distance. Let us consider an incident X-ray beam interacting with the atoms arranged in a periodic manner as shown in two dimensions in figure. The atoms, represented as spheres in the illustration, can be viewed as forming different sets of planes in the crystal. For a given set of lattice planes with an inter-plane distance of d, the condition for a diffraction (peak) to occur can be simple written as

$$2d \sin n\theta = n\lambda$$

which is known as Bragg‟s law. In the equation, λ is the wavelength of the X-ray, θ is the scattering angle, and n is an integer representing the order of the diffraction peak.

The Bragg‟s Law is one of the most important laws used for interpreting X – ray diffraction data. From the law, we find that the diffraction is only possible when $\lambda < 2d$ [1].

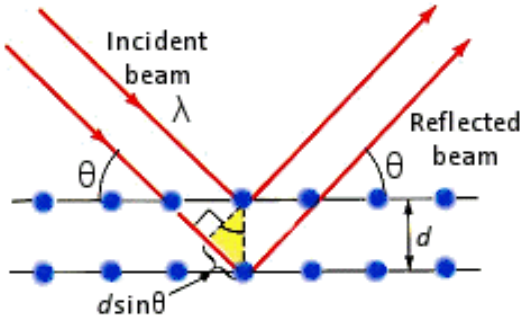

Fig. 4.1: Bragg's diffraction pattern

In the present work, A PHILIPS PW 3040 X‟pert PRO X-ray diffracto-meter was used for the lattice parameter to study the crystalline phases of the prepared samples in the Materials Science division, Atomic Energy Centre, Dhaka (AECD). Figure shows the block diagram of X‟pert PRO XRD system. The powder diffraction technique was used with a primary beam powder of 40 kV and 30 mA for Cu-K_α radiation. A nickel filter was used to reduce Cu-Kβ radiation and finally Cu-Kα radiation was only used as the primary beam. The experimental has been performed at room temperature. A 2θ scan was taken from 15° to 70° to get possible fundamental peaks of the samples with the sampling pitch of 0.02° and time for each step data collection was 1.0 sec. Both the programmable divergence and receiving slits were used to control the irradiated beam area and output intensity from the powder sample, respectively. An anti-scatter slit was used just after the tube and in front of the detector to get parallel beam only. All data of the samples were stored in the computer memory and later on analyzed them using

computer “software, X‟ PERT HJGHS CORE”. For XRD experiment each sample was set on a glass slide and fixed the sample by putting adhesive typed the two ends of the sample.

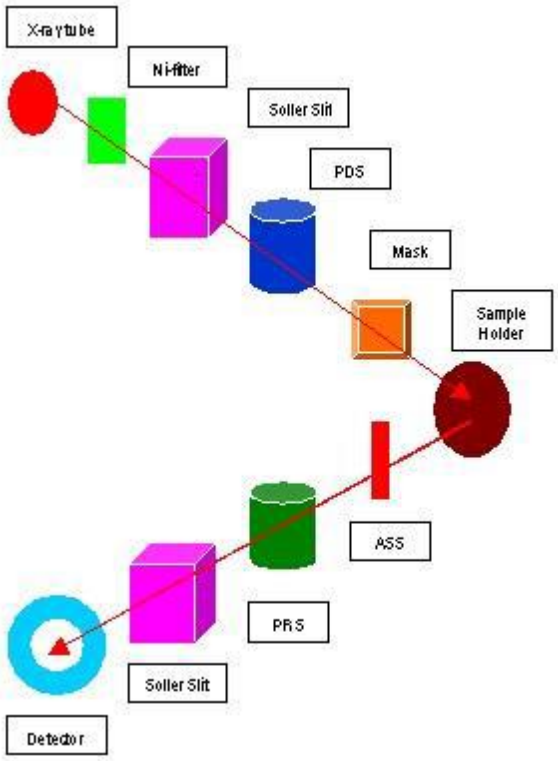

Fig. 4.2: Block diagram of the PHILIPS PW 3040 X‟ Pert PRO XRD system

For each composition, the cylindrical samples of weight more than 2 gm are converted into powder. For XRD experiment each sample was set on a glass slide and fixed the sample by putting adhesive tape at the two ends of the sample X-ray diffraction patterns were carried out to confirm the crystal structure. Instrumental broadening of the system was determined from θ-2θ scan of standard Si. At (311) reflection’s position of the peak, the value of instrumental broadening was found to be 0.07°. This value of instrumental

broadening was subtracted from the pattern. After that, using the X-ray data, the lattice constant (a) and hence the X-ray densities were calculated.

Figure shows the inside view of the X‟ pert PRO XRD system. A complex of instruments of X- ray diffraction analysis has been established for both materials research and specimen characterization.

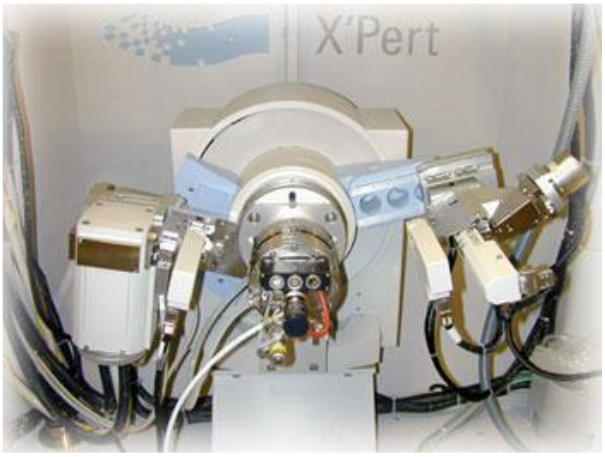

Fig. 4.3: Internal arrangement of a PHILIPS X‟ Pert PRO X-ray diffractometer

4.1.1.1 Lattice constant and Identify Phase

The XRD data consisting of θ_{hkl} and d_{hkl} values corresponding to the different crystallographic planes are used to determine the structural information of the samples like lattice parameter and constituent phase. Lattice parameters of Co-ferrites samples were determined. Normally, lattice parameter of an alloy composition is determined by the Debye-Scherrer method after extrapolation of the curve. We determine the lattice spacing (inter-planer distance), d using these reflections from the equation which is known as Bragg's Law.

$$2d_{hkl} \sin\theta = \lambda$$

$$\text{i.e. } d_{hkl} = \frac{\lambda}{2\sin\theta}$$

where λ is the wavelength of the X-ray, θ is the diffraction angle and n is an integer representing the order of the diffraction.

The lattice parameter for each peak of each sample was calculated by using the formula:

$$a = d_{hkl}\sqrt{h^2 + k^2 + l^2}$$

where h, k, l are the indices of the crystal planes. We get d_{hkl} values from the computer using software "X" Pert HJGHS CORE". So we got seven 'a' values for seven reflection planes such as a a_1, a_2, a_3 ….. etc. Determine the exact lattice parameter for each sample, through the Nelson-Riley extrapolation method. The values of the lattice parameter obtained from each reflected plane are plotted against Nelson-Riley function. The Nelson-Riley function F (θ), can be written as

$$f(\theta) = \frac{1}{2}\left[\frac{\cos^2\theta}{\sin^2\theta} + \frac{\cos^2\theta}{\theta}\right]$$

where θ is the Bragg's angle. Now drawing the graph of a vs. F(θ) and using linear fitting of those points will give us the lattice parameter a_0. This value of a_0 at F(θ) = 0 or θ = 90° .These a_0 are calculated with an error estimated to be ± 0.0001Å.

4.1.1.2 X-ray Density and Bulk Density

X-ray density, d_x was also calculated usual from the lattice constant. The relation between d_x and a is as follows,

$$d_x = \frac{8M}{N_a a_0^3}$$

Where, M is the molecular weight of the corresponding composition, N_a is the Avogadro's number (6.023×10^{23} $mole^{-1}$), *a* is the lattice parameter. The bulk density was calculated considering a cylindrical pellet of mass (m) and volume (V) of the pellets using the relation

$$d_B = \frac{m}{V} = \frac{m}{\pi r^2 h}$$

Where, m is the mass of the pellet sample, r is the radius and h is the thickness of the pellet.

4.1.1.3 Porosity

Porosity is a parameter which is inevitable during the process of sintering of oxide materials. It is noteworthy that the physical and electromagnetic properties are strongly dependent on the porosity of the studied samples. Therefore an accurate idea of percentage of pores in a prepared sample is prerequisite for better understanding of the various properties of the studied samples to correlate the microstructure property relationship of the samples under study. The porosity of a material depends on the shape, size of grains and on the degree of their storing and packing. The difference between the bulk density d_B and X-ray density d_x gave us the measure of porosity. Percentage of porosity has been calculated using the following relation [2]

$$P = \left(1 - \frac{d_B}{d_x}\right) \times 100\%$$

4.1.2 Field Emission Scanning Electron Microscope (FESEM)

The microstructure of the samples has been studied by the Field Emission Scanning Electron Microscope (FESEM) from Bangladesh University of Engineering and Technology (BUET), Dhaka.

FESEM works with electrons (particles with a negative charge) instead of light. These electrons are liberated by a field emission source. The object is scanned by electrons according to a zig-zag pattern. It is used to visualize very small topographic details on the surface or entire or fractioned objects. Researchers in biology, chemistry and physics apply this technique to observe structures that may be as small as 1 nanometer (= billion of a millimeter). The FESEM may be employed for example to study organelles and DNA material in cells, synthetical polymers, and coatings on microchips.

Electrons are liberated from a field emission source and accelerated in a high electrical field gradient. Within the high vacuum column these so-called primary electrons are focused and deflected by electronic lenses to produce a narrow scan beam that bombards the object. As a result secondary electrons are emitted from each spot on the object. The angle and velocity of these secondary electrons relates to the surface structure of the object. A detector catches the secondary electrons and produces an electronic signal. This signal is amplified and transformed to a video scan-image that can be seen on a monitor or to a digital image that can be saved and processed further.

4.1.3 Energy Dispersive Spectrometer (EDS)

Energy Dispersive X-Ray Spectroscopy (EDS or EDX) is a chemical microanalysis technique used in conjunction with scanning electron microscopy (SEM). The EDS technique detects X-rays emitted from the sample during bombardment by an electron beam to characterize the elemental composition of the analyzed volume. Features or phases as small as 1 μm or less can be analyzed.

When the sample is bombarded by the SEM's electron beam, electrons are ejected from the atoms comprising the sample's surface. The resulting electron vacancies are filled by electrons from a higher state, and an X-ray is emitted to balance the energy difference between the two electrons' states. The X-ray energy is characteristic of the element from which it was emitted.

The EDS X-ray detector measures the relative abundance of emitted x-rays versus their energy. The detector is typically lithium-drifted silicon, solid-state device. When an incident X-ray strikes the detector, it creates a charge pulse that is proportional to the energy of the X-ray. The charge pulse is converted to a voltage pulse (which remains proportional to the x-ray energy) by a charge-sensitive preamplifier. The signal is then sent to a multichannel analyzer where the pulses are sorted by voltage. The energy as determined from the voltage measurement, for each incident x-ray is sent to a computer for display and further data evaluation. The spectrum of X-ray energy versus counts is evaluated to determine the elemental composition of the sampled volume [8].

4.2 Magnetic properties measurement

Magnetization in ferrite samples originate due to the difference in the magnetic moments for the two sub-lattices. The larger the difference, the greater is the resultant magnetization, because of the anti-parallel arrangements of the moments in two sub-lattices. Different ions occupy different 2 sites. So, as a whole, the two sub-lattices have their individual resultant magnetic moments. The differences in magnetic moment between the two sub-lattices give rise to net magnetic moment which in turn yields magnetization. In the present study magnetization has been performed using a VSM.

4.2.1 Principle of Vibrating Sample Magnetometer (VSM)

Vibrating sample magnetometer (VSM) systems are used to measure the magnetic properties of materials. The vibrating component causes a change in the magnetic field of the sample, which generates an electrical field in a coil based on Faraday's Law of Induction. It is a versatile and sensitive method of measuring magnetic properties developed by S. Foner [9] and is based on the flux change in a coil when the sample is vibrated near it.

If the sample is placed within a uniform magnetic field H, a magnetization M will be induced in the sample. In a VSM, the sample is placed within suitably placed sensing coils, also held at the desired angle. And the vibrating sample component is made to undergo sinusoidal motion, i.e., mechanically vibrated.

The electromagnet activates before the testing starts so if the sample is magnetic, it will become more so the stronger the field that is produced. A magnetic field H appears

around the sample and, once the vibration begins then the magnetization of the sample can be analyzed as changes occur in relation to the timing of movement. Because magnetic flux changes induce a voltage in the sensing coils that is proportional to the magnetization of the sample. Changes in the signal are converted to values by the software to graph magnetization M versus the magnetic field H strength, often referred to as a hysteresis loop.

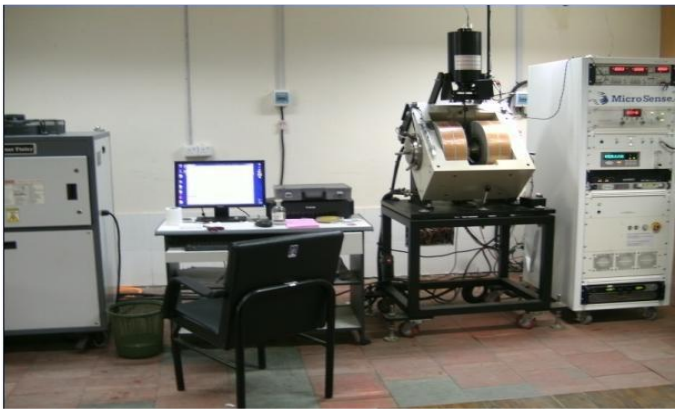

Fig. 4.4: Vibrating Sample Magnetometer

4.2.2 Permeability Measurement

From the frequency dependence of complex permeability, evolution of permeability and magnetic loss component at different stages of ferrite sample as affected by thermal treatment at different temperature was determined using toroid shape sample prepared with insulating Cu wire. The WK 6500B Impedance analyzer directly measures the value of inductance as shown in figure, L and loss factor.

$$D = tan\delta$$

From inductance the value of real part of complex permeability, μ' can be obtained by using the relation, $\mu' = \frac{L}{L_0}$

Where, L is the inductance of the toroid and L_o is the inductance of the coil of same geometric shape in vacuum, L_o is determined by using the relation,

$$L_0 = \frac{\mu_0 N^2 S}{\pi \bar{d}}$$

Here μ_0 is the permeability of the vacuum, N is the number of turns (N = 8), S is the cross-sectional area of the toroid shaped sample, S = dh, where,

$$d = \frac{d_1 \sim d_2}{2}$$

đ is the average diameter of the toroid sample given as

$$\bar{d} = \frac{d_1 + d_2}{2}$$

where, d_1 and d_2 are the inner and outer diameter of the toroid samples.

Fig. 4.5: Impedance Analyzer Model-Wayne kerr (6500B)

4.2.3 Curie Temperature Measurement

Curie temperature measurement is one of the most important measurements for magnetic materials. Curie temperature provides substantial information on magnetic status of a substance in respect of the strength of exchange interaction. So, the determination of Curie temperature is of great importance.

Curie temperature was measured from the temperature dependent initial permeability. For this measurement, the sample was kept inside a little oven with a thermocouple placed at the middle of the sample. The thermocouple measures the temperature inside the oven and also of the sample. The sample was kept just in the middle part of the cylindrical oven in order to minimize the temperature gradient. The temperature of the oven was then raised slowly. If the heating rate is very fast then temperature of the sample may not follow the temperature inside the oven, and there can be misleading information on the temperature of sample. The thermocouple showing the temperature in that case will be erroneous. Due to the closed winding of wires, the sample may not receive the heat at once. Therefore, a slow heating rate was used to eliminate this problem. Also, a slow heating ensures accuracy in the determination of Curie temperature. The oven was kept thermally insulated from the surroundings. The temperature dependent permeability was measured at a constant frequency (100 kHz) of a sinusoidal wave.

4.3 Electrical Properties Measurement

There is a sense in which every property of a solid can be considered an electrical property. This is because the particles that make up solids are fundamentally electrical in nature. The response of solids to externally applied electric fields is referring to as electrical properties.

4.3.1 Electrical Conductivity and Resistivity

The AC and DC resistivity and conductivity of the samples has been measured using conventional two probe method, using pellet samples of diameter 4.7-5.1 mm and of thickness 1.7-1.9 mm by applying silver electrodes on the surfaces. Samples were prepared by sintering the samples at 1050℃ and 1100 ℃ for 4 hours. The samples were polished using silicon carbide papers with grit size 600 and 1200. Then silver paste was added to both the sides of the polished pellet samples together with two thin copper wires of 100 micron diameter for conduction. Again the samples are dried at room temperature to eliminate any absorbed moisture.

When any substance is subject to an applied electric field E, a current of electronic charge flows through the substance. The magnitude of the resultant current density, j, is characterized by the electrical resistivity ρ or the electrical conductivity $\sigma = {}^{1}/_{\rho}$ of the substance. The electrical resistivity and conductivity are determined by:$j = \sigma E$ and $E = \rho j$

If the current density is measured in Am^{-2} and electric field (E) in Vm^{-1}, then the units of σ are $\Omega^{-1}m^{-1}$ or Sm^{-1}. The SI symbol of S stands for Siemens not to be confused with‘s’

for second. The units of resistivity are Ωm. for an example of cross sectional area A and length L, the resistivity is related to the electrical resistance R by:

$$\rho = {}^{RA}/_{L}\ \Omega\text{m}.$$

4.3.2 Dielectric Relaxation

The dielectric properties of materials, namely permittivity, are typically measured as a function of frequency and are called dielectric. The permittivity values show the interaction of an external field with the electric dipole moment of the sample [10]. Dielectric measurement is an important tool to understand the material behavior especially at high frequencies because it can provide the electrical or magnetic characteristics of the materials, which is a critical parameter required to implement the material in many applications. The measurement of complex dielectric properties of materials at radio frequency (RF) and microwave frequency is very relevant especially in the research fields, such as material science, communication, microwave circuit design and biological research [11]. A number of methods have been developed to measure the complex permittivity of materials in time domain or frequency domain using transmission (2 ports) or reflection (1 port) methods. Each technique is limited to specific frequencies, materials and applications and has its own limitations.

The frequency dependence of dielectric constant was obtained using an Impedance Analyzer (Hewlett Packard, model no. 4192A) in the frequency range of 1 kHz to 100 MHz. The pellet shaped samples were well polished to remove any roughness and the two surfaces of each pellet were coated with silver paste as contact material for electrical and dielectric measurements.

The real part of dielectric constant was calculated from the formula

$$\varepsilon' = CL/\varepsilon_0 A$$

where, C is the capacitance, L is the thickness or height, and A is the cross-sectional area of the flat surface of the pellet, ε_0 is the permittivity for free space which is constant.

The imaginary part of dielectric constant was calculated from using the formula;

$$\varepsilon'' = \varepsilon' tan\delta$$

Measurement of dielectric properties involves measurements of the complex relative permittivity, which consists of a real part and an imaginary part. As mentioned earlier, the real part of the complex permittivity, also known as the dielectric constant is a measure of the amount of energy from an external electrical field stored in the material. The imaginary part is zero for lossless materials and is also known as loss factor. It is a measure of the amount of energy loss from the material due to an external electric field. Loss tangent:

$$tan\delta = \frac{\varepsilon''}{\varepsilon'}$$

The term tanδ is called loss tangent (dissipation factor or loss factor) and it represents the ratio of the imaginary part to the real part of the complex permittivity.

4.3.3 Electric Modulus

The complex electric modulus spectrum represents the measure of the distribution of ion energies or configurations in the structure and it also describe the electrical

relaxation and microscopic properties of ferrites. The modulus formalism has been adopted as suppresses the polarization effects at the electrode interface. Hence, the complex electric modulus M spectra reflect the dynamics properties of the sample alone. Hence, the real and imaginary parts of electric modulus are calculated by using following equations:

$$M^* = {}^1\!/_{\varepsilon^*}$$

$$M' = \frac{\varepsilon'}{(\varepsilon'^2 + \varepsilon''^2)}$$

$$M'' = \frac{\varepsilon''}{(\varepsilon'^2 + \varepsilon''^2)}$$

Where M^*, M' and M" represents the complex electric modulus, real and imaginary part of electric modulus, respectively.

4.3.4 Impedance Spectroscopy

The overall electrical properties of a polycrystalline ceramic material have contribution from grains, grain boundaries and specimen electrode interfaces. Each of these contributions can be represented by a suitable combination of resistance and capacitance in parallel. The sample can thus be represented by an equivalent circuit containing three parallel R-C elements connected in series [12]. In impedance analysis, the imaginary part of the total complex impedance, z^* is plotted as a function of real part, z' over a range of frequencies (10^3 -10^7 Hz in the present work). If the time constant for three RC elements is different (ratio >10), each parallel RC element gives rise to a semicircle with

its center on the z' axis if there is only single value of relaxation time [13]. The resistance value for each element is obtained from the intercept of the arc on z' axis corresponding to that element. Capacitance values are calculated by using the relation, $C_0 = \varepsilon_0 A/t$,

$\omega = 2\pi f$,

f being the frequency corresponding to the maximum of each circular arc. If any of them above processes have a distribution of relaxation times, then one obtain a depressed circular arc in the impedance plot having its center below the z' axis.

Complex plane modulus plots give complementary information to the information given by complex plane impedance plots. The real part of impedance data are calculated by using the relations [14]

$$Z' = \frac{M''}{\omega C_0}$$

And the imaginary part,

$$Z'' = \frac{M'}{\omega C_0}$$

References

[1] T. Abbas, M. U. Islam, M.C. Ashraf, Mod. Phy. Letts., B 9(22), 1419, 1995.

[2] Smit and Wijn W. J. P.; ―Ferrites, Philips Technical Libery C Wiley, New York, 1959.

[3] H. M. Rietveld, J. Appl. Cryst. 2 (1969) 65.

[4] H. M. Rietveld, Acta, Cryst 22 (1967) 151.

[5] J. Rodriquez-Cravajal, Physica B, 192 (1993) 55.

[6] L. B. McCusker, R. B. Von Dreele, D. E. Cox, D. Louer and P. Scardi, J. Appl Cryst. 32 (1999) 36.

[7] R. A. Young, "The Rietveld Method", Oxford University Press Inc (1993).

[8] Handbook of Materials Failure Analysis with Case Studies from the Oil and Gas Industry, 2016.

[9] S. Forner; "Versatile and Sensitive Vibrating Sample Magnetometer", Rev.Sci. Instr. 30, P.548, 1959.

[10] Griffiths 1999, Baker-Jarvis, et al. 2010, Yaw 2012.

[11] Burdette, et al.1980, F.H.Wee, et al.2009.

[12] J. R. Macdonald, Impedance Spectroscopy: Emphasizing Solid Materials and Systems, Wiley Inter science Publication, New York (1987).

[13] L. Pandey, O. Parkash, K. K. Rajesh and D.Kumar, Bull. Mater. Sci.18 (1995) 5.

[14] S. Upadhyay, D. Kumar, O. Parkash, Bull. Mater. Sci.19 (1996) 513.

Chapter 5 : Results and Discussion

5.6 Structural Properties

5.1.4 X-Ray Diffraction Analysis

5.1.5 Lattice Constant

5.1.6 Density and porosity

5.7 Morphological study of $Co_{0.5}Zn_{0.5}Y_xFe_{2-x}O_4$ (CZYFO) ($0.00 \leq x \leq 0.08$)

5.8 Energy dispersive Spectroscopy

5.9 Magnetic Properties of $Co_{0.5}Zn_{0.5}Y_xFe_{2-x}O_4$; (x=0.00, 0.02, 0.04, 0.06, 0.08) ferrites

5.4.4 Magnetization

5.4.5 Permeability

5.4.6 Quality Factor

5.10 Electrical Properties of $Co_{0.5}Zn_{0.5}Y_xFe_{2-x}O_4$ ferrites

5.5.5 AC and DC Resistivity

5.5.6 Dielectric Relaxation Properties

5.5.7 Electric Modulus Analysis

5.5.8 Impedance Spectra and Cole-Cole Plot

References

Chapter 5: Results and Discussion

5.1 Structural Properties

5.1.1 X-Ray Diffraction Analysis

The X-ray diffraction (XRD) patterns of Y-substituted Co-Zn ferrites with the chemical composition of $Co_{0.5}Zn_{0.5}Y_xFe_{2-x}O_4$ (CZYFO) ($0.00 \leq x \leq 0.08$) sintered at 1100 °C have been depicted in Fig 5.1. The creation of cubic spinel structure has been confirmed from the well-defined diffraction peaks in the planes. The samples show sole single phase cubic spinel structure up to $x = 0.04$ and a slight amount of secondary phase ($YFeO_3$) in the plane (121) has also been identified at $x>0.06$. The similar extra phase recognized (121) reflection at $2\theta = 33.1°$ for $YFeO_3$ according to the ICDD PDF #39-1489 [1]. The similar peak has been reported that this secondary phase confirms the solubility limit of rare earth ions (Y^{3+}) and Fe^{3+} ions in the ferrites [2, 3].

5.1.2 Lattice Constant

The theoretical lattice constant of $Co_{0.5}Zn_{0.5}Y_xFe_{2-x}O_4$ ($0.00 \leq x \leq 0.08$) can be calculated from the equation, $a_{th} = \frac{8}{3\sqrt{3}}[(r_A + R_0) + \sqrt{3}(r_B + R_0)]$, where r_A = ionic radius of tetrahedral A site, r_B = ionic radius of octahedral B site and R_0 = ionic radius of oxygen ion (1.32 Å) [4, 5]. The chemical formula for the cation distribution of Y substituted Co-Zn ferrite is as follows $[Fe_{0.5}^{2+}Zn_{0.5}^{2+}]\,[Fe_{1-x}^{3+}Co_{0.5}^{2+}Y_x^{3+}]O_4^{2-}$, where $[Fe_{0.5}^{2+}Zn_{0.5}^{2+}]$ and $[Fe_{1-x}^{3+}Co_{0.5}^{2+}Y_x^{3+}]O_4^{2-}$ contribute in A and B site, respectively.

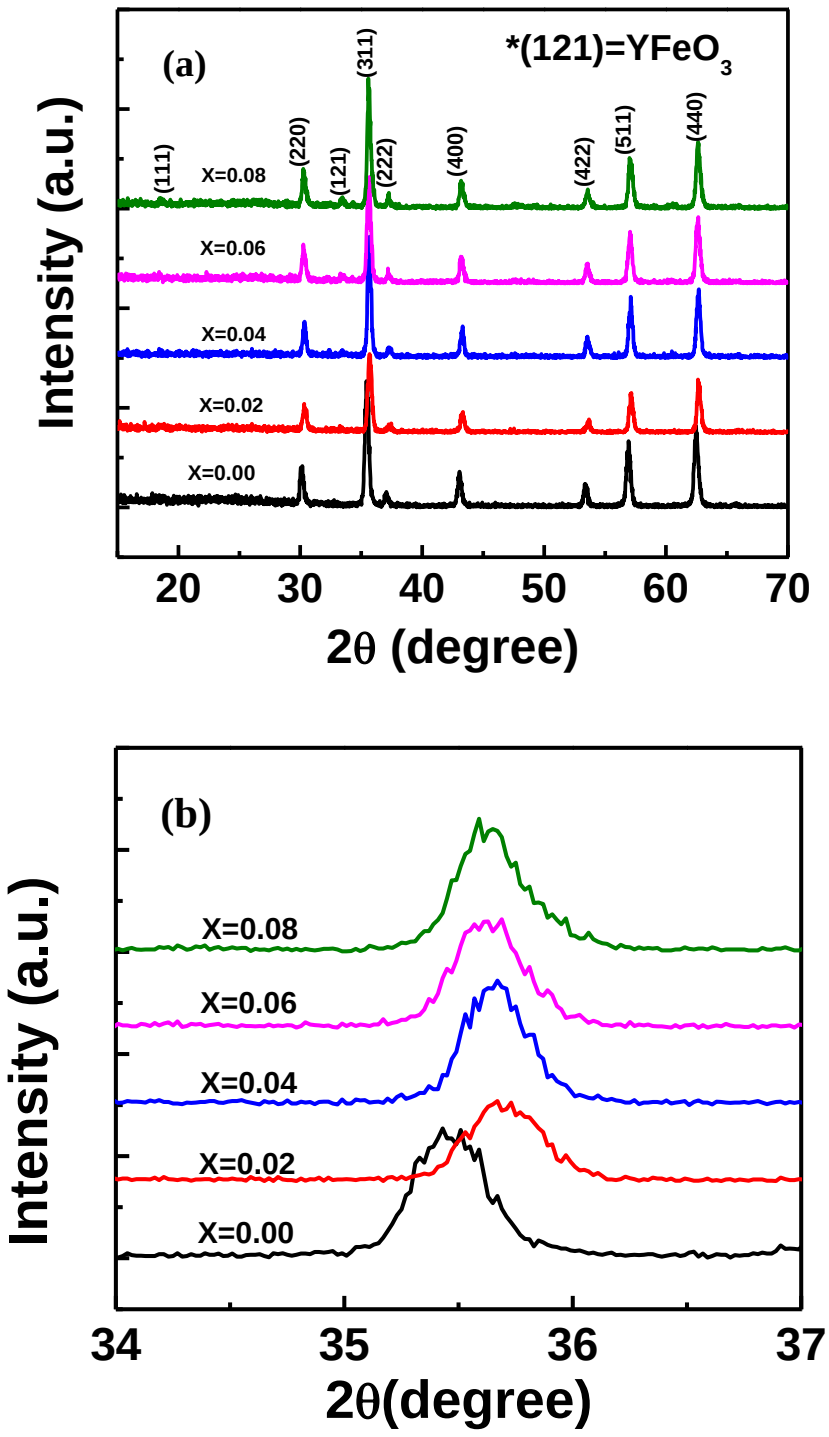

Fig. 5.1: (a) The XRD pattern of $Co_{0.5}Zn_{0.5}Y_xFe_{2-x}O_4$ (CZYFO) ($0.00 \leq x \leq 0.08$) sintered at 1100 °C and **(b)** highest peak intensity at 2θ.

The calculated ionic radius of r_A and r_B are shown in Fig. 5.2. The radius of individual ions are of r_{Zn} =0.74Å, r_{Co}=0.745Å, r_{Fe} =0.645Å, and r_Y=0.95Å. The ionic radius of Y^{3+} ion is larger than that of Fe^{3+}, results the lattice parameter of the ferrites increases that is consistent with reported values [6].

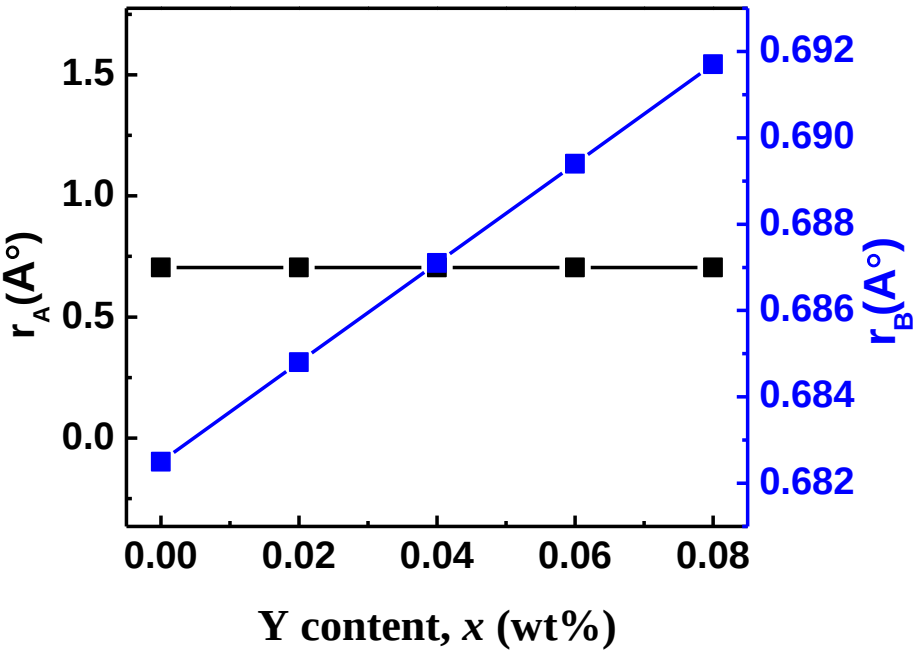

Fig. 5.2: Ionic radius of A-site and B-site for different Y content in the $Co_{0.5}Zn_{0.5}Y_xFe_{2-x}O_4$ (CZYFO) ($0.00 \leq x \leq 0.08$) sintered at 1100 °C.

The experimental lattice constant (*a)* has been calculated using the formula, $a = d\sqrt{h^2 + k^2 + l^2}$, where *h*, *k* and *l* are the Miller indices of the crystal planes that is used for all peaks of the samples. The Nelson-Riley (N-R) extrapolation scheme has been used to evaluate lattice constants, the N-R function, *F*(θ), is given as $F(\theta) = \frac{1}{2}\left[\frac{cos^2\theta}{sin\theta} + \frac{cos^2\theta}{\theta}\right]$ [7]. The exact value of *a* is obtained at y-axis cut point from the least

square fit straight line in the a vs. $F(\theta)$ plot. The lattice parameter is also strongly depends on the A-site and B-site cationic distribution of a spinel structure. So that, the ions redistribution of tetrahedral A site and octahedral B-site contribute in the decrease of lattice parameter for x=0.02 [8]. The introduction of larger Yttrium ion in the octahedral site can be decrease the lattice parameter for possible ion emptiness during

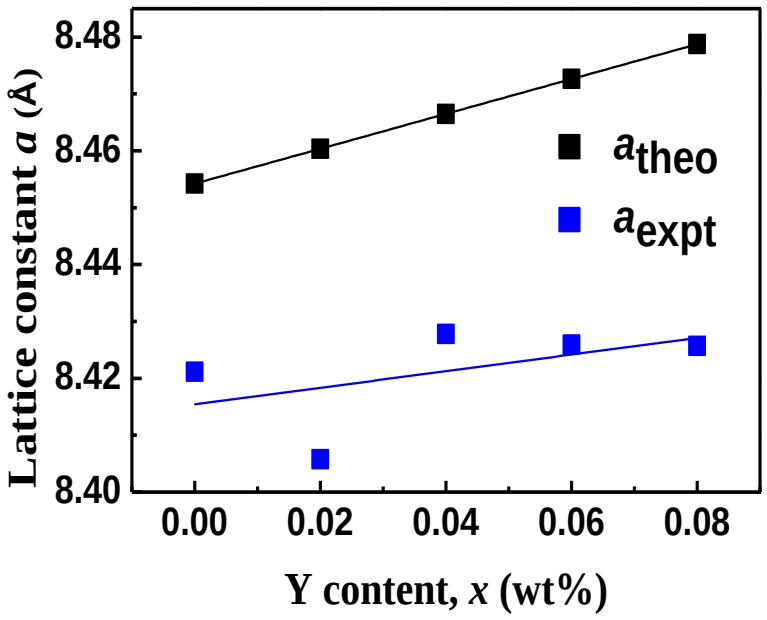

Fig. 5.3: The variation of theoretical lattice constant (a_{theo}) and experimental (a_{expt}) with Y content at T_s=1100 °C and solid line represents linear fitting.

crystalline process [9]. The theoretical (a_{theo}) and experimental (a_{expt}) lattice parameters as a function of Y content have been represented in Fig. 5.3. The results are in good agreement with Vegard's law [10].

The average values of a_{theo} and a_{expt} have been measured (square) and fit the data (solid line) is shown in Fig.5.3(a.) and found to be 8.4542 and 8.4154 Å, respectively. The obtained values are very close with 0.5% variation that approves validity of our calculation.

Table 5.11: The Chemical formula, cation distribution, ionic radius of A and B-sites and theoretical a_{th}(Å) and experimental a_{exp}(Å) lattice parameter:

x	Chemical formula	A site	B site	r_A(Å)	r_B(Å)	a_{th}(Å)	a_{exp}(Å)
0.0	$Co_{0.5}Zn_{0.5}Fe_2O_4$	$Fe_{0.5}Zn_{0.5}$	$Fe_{1.5}Co_{0.5}$	0.705	0.6825	8.454235	8.42113
0.02	$Co_{0.5}Zn_{0.5}Fe_{1.98}Y_{0.02}O_4$	$Fe_{0.5}Zn_{0.5}$	$[Fe_{1.48}Co_{0.5}Y_{0.02}]O_4^{2-}$	0.705	0.6848	8.460366	8.40578
0.04	$Co_{0.5}Zn_{0.5}Fe_{1.96}Y_{0.04}O_4$	$Fe_{0.5}Zn_{0.5}$	$[Fe_{1.46}Co_{0.5}Y_{0.04}]O_4^{2-}$	0.705	0.6871	8.466496	8.42779
0.06	$Co_{0.5}Zn_{0.5}Fe_{1.94}Y_{0.06}O_4$	$Fe_{0.5}Zn_{0.5}$	$[Fe_{1.44}Co_{0.5}Y_{0.06}]O_4^{2-}$	0.705	0.6894	8.472627	8.4259
0.08	$Co_{0.5}Zn_{0.5}Fe_{1.92}Y_{0.08}O_4$	$Fe_{0.5}Zn_{0.5}$	$[Fe_{1.42}Co_{0.5}Y_{0.06}]O_4^{2-}$	0.705	0.6917	8.478758	8.42569

5.1.3 Density and porosity

The bulk density was measured by usual mass and dimensional consideration whereas X-ray density was calculated from the molecular weight and the volume of the unit cell for each sample.

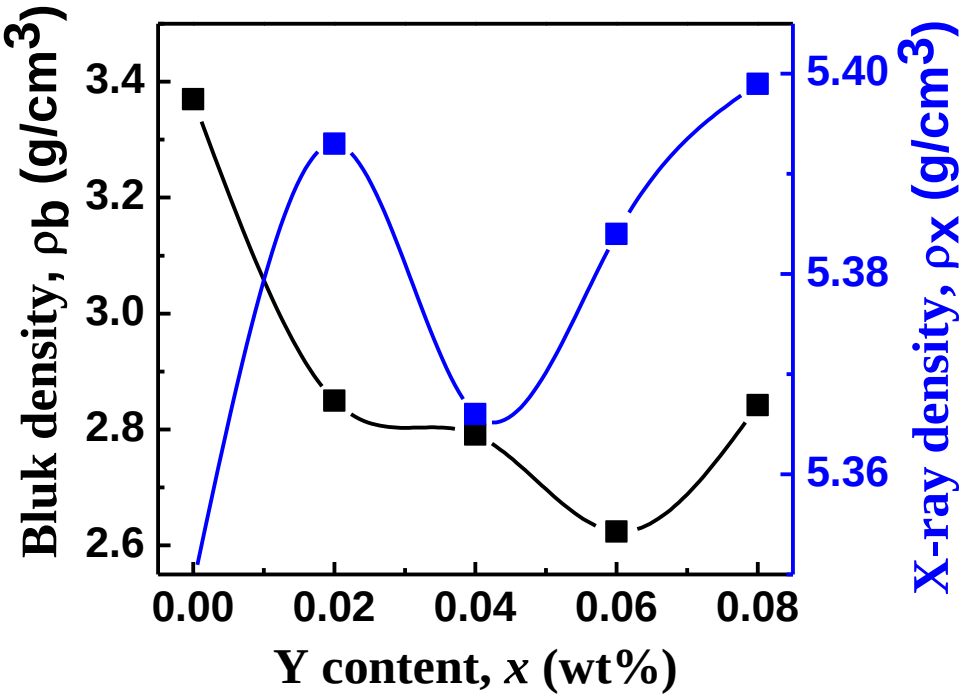

Fig. 5.4: The bulk and X-ray density for Yttrium variation in the the $Co_{0.5}Zn_{0.5}Y_xFe_{2-x}O_4$ (CZYFO) ($0.00 \leq x \leq 0.08$) sintered at 1100 °C.

The calculated values of the bulk density and theoretical (or X-ray) density of the present ferrite system are shown in figure 5.4. It is observed that bulk density is lower than the X-ray density. This may be due to the existence of pores which were formed and developed during the sample preparation or sintering process.

5.2 Morphological study of $Co_{0.5}Zn_{0.5}Y_xFe_{2-x}O_4$ (CZYFO) ($0.00 \leq x \leq 0.08$)

A room temperature surface morphology or microstructure study of $Co_{0.5}Zn_{0.5}Y_xFe_{2-x}O_4$; ($x$=0.00, 0.02, 0.04, 0.06, 0.08) ferrites sintered at 1100 °C are investigated by the FESEM for ruptured surfaces as shown in Fig.5.5. The FESEM images reveal the samples are packed, crack-free with homogeneous grain distribution having clear grain boundaries throughout the samples. The ferrites attain a uniform grain size distribution owing to homogeneous distribution of the driving force of grain boundary in each grain [11]. The variation of grain size has significant impression on the electric and magnetic properties of a ferrite.

The grain size has been measured using the imageJ software [12] and linear intercept method by including adequately enormous number of grains from surface micrographs of the samples. The Y content dependent grain size of the samples is illustrated in Fig.5.5. The grain sizes initially decrease with increasing Y^{3+} ions content at x = 0.2 and then it almost linearly increases at x>0.2. The manner of grain growth in the samples strongly depends on the force between driving force for the grain boundary movement and the impeding force exerted by pores [11].

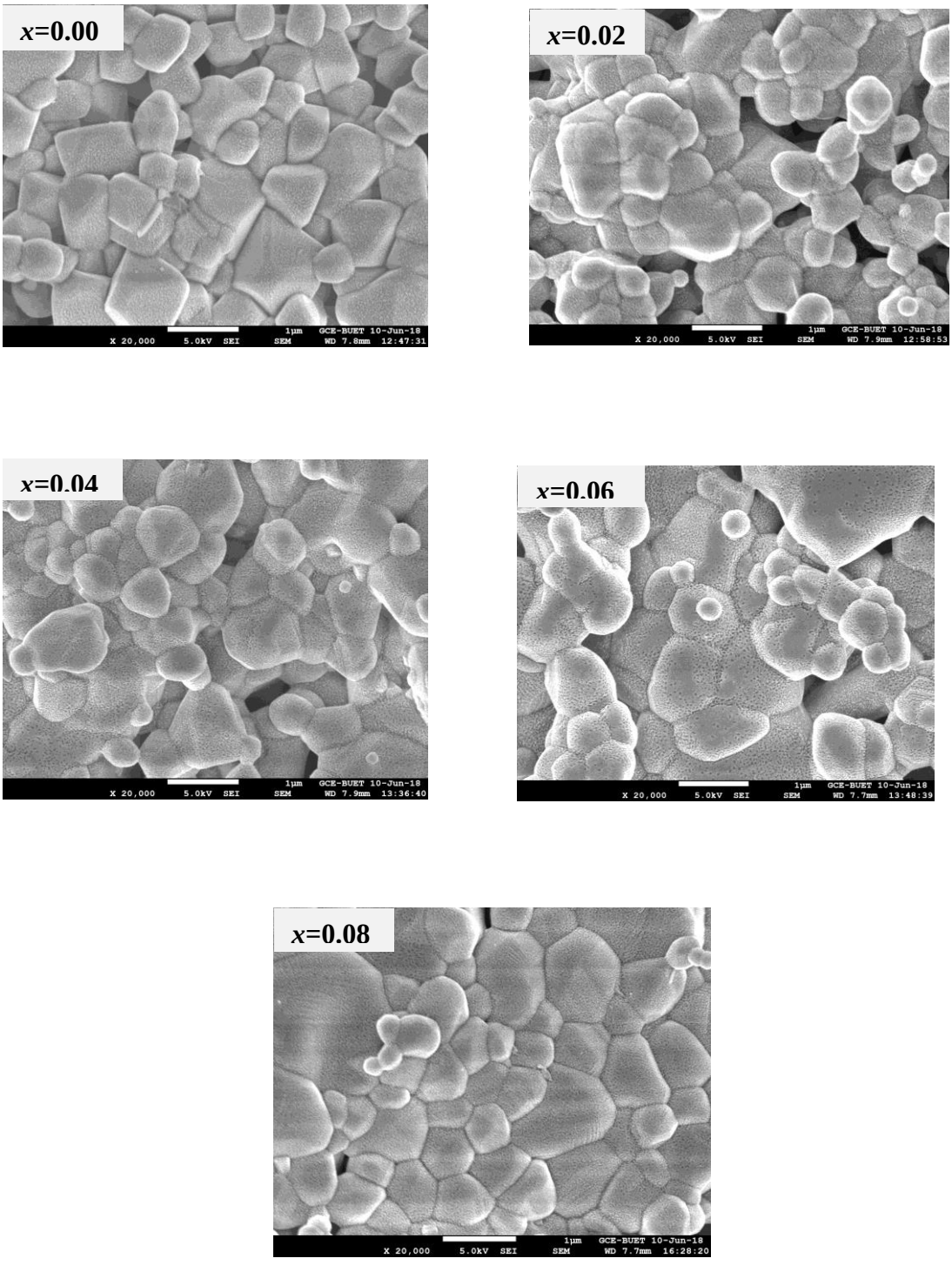

Fig. 5.5: FESEM micrographs of $Co_{0.5}Zn_{0.5}Y_xFe_{2-x}O_4$; ($x$=0.00, 0.02, 0.04, 0.06, 0.08) sintered at 1100 °C.

The larger bonding energy of Y^{3+}-O^{2-} than that of Fe^{3+}-O^{2-} that requires more energy in mass transfer process of impeded $FeYO_3$ in the grain boundaries consequently the grain size decreases initially (Fig. 5.6) [13]. Later on, some divalent Fe^{2+} ions are replaced by the Y^{3+} ions in the grain boundaries results the grain size rises with increasing Y^{3+} substitution to balance the electric charge for vicinity of metallic charge vacancies [14].

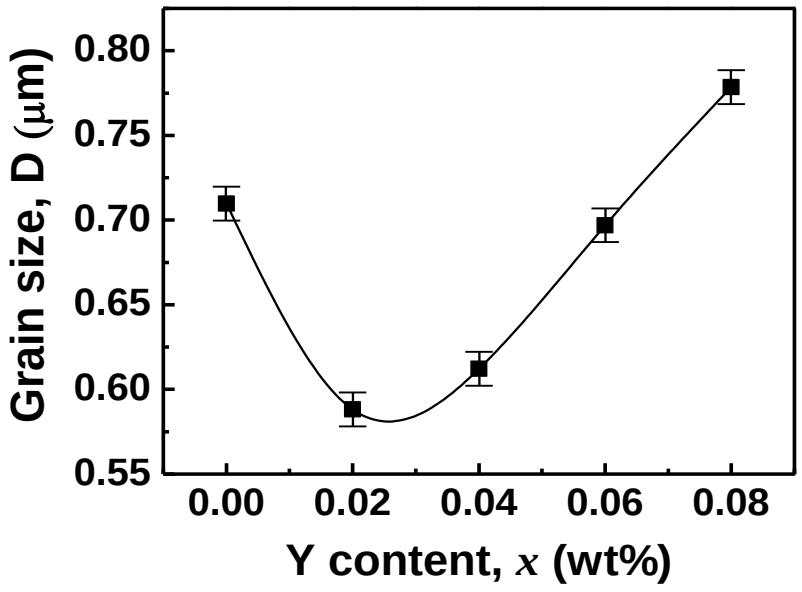

Fig. 5.6: The variation of grain size with Y^{3+} substitution of $Co_{0.5}Zn_{0.5}Y_xFe_{2-x}O_4$; (x=0.00, 0.02, 0.04, 0.06, 0.08) ferrite sintered at 1100 °C.

5.3 Energy Dispersive Spectroscopy:

The electron dispersive spectroscopy (EDS) patterns of the $Co_{0.5}Zn_{0.5}Y_xFe_{2-x}O_4$ ferrites for x=0.00 and x=0.02 are presented in the Fig. 5.7. The peaks obtain for the elements Co, Zn, Fe, Y, O that indicate the purity of the samples.

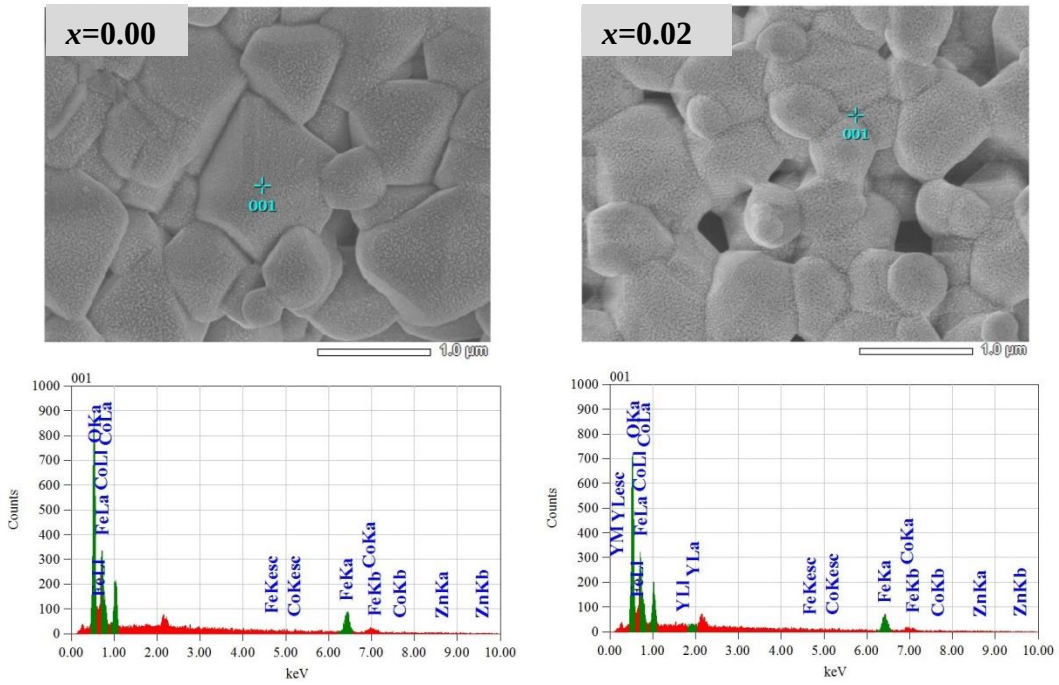

Fig.5.7: The EDS pattern of $Co_{0.5}Zn_{0.5}Y_xFe_{2-x}O_4$ ferrites for x=0.00 and 0.02 with T_s=1100°C at room temperature

5.4 Magnetic Properties of $Co_{0.5}Zn_{0.5}Y_xFe_{2-x}O_4$; (x=0.00, 0.02, 0.04, 0.06, 0.08) ferrites

5.4.1 Magnetization

The room temperature static applied magnetic field, H (up to 10 kOe) magnetization hysteresis loops and its first quadrant of the $Co_{0.5}Zn_{0.5}Y_xFe_{2-x}O_4$; ($x$=0.00, 0.02, 0.04, 0.06, 0.08) compositions sintered at 1100 °C are shown in Fig. 5.8. The values of saturation magnetization (M_s), remanent magnetization (M_r) and coercive field (H_c) of the samples have been calculated and presented in Table 5.2. The value of magnetization upsurges with increasing applied magnetic field up to a certain field then it becomes saturated.

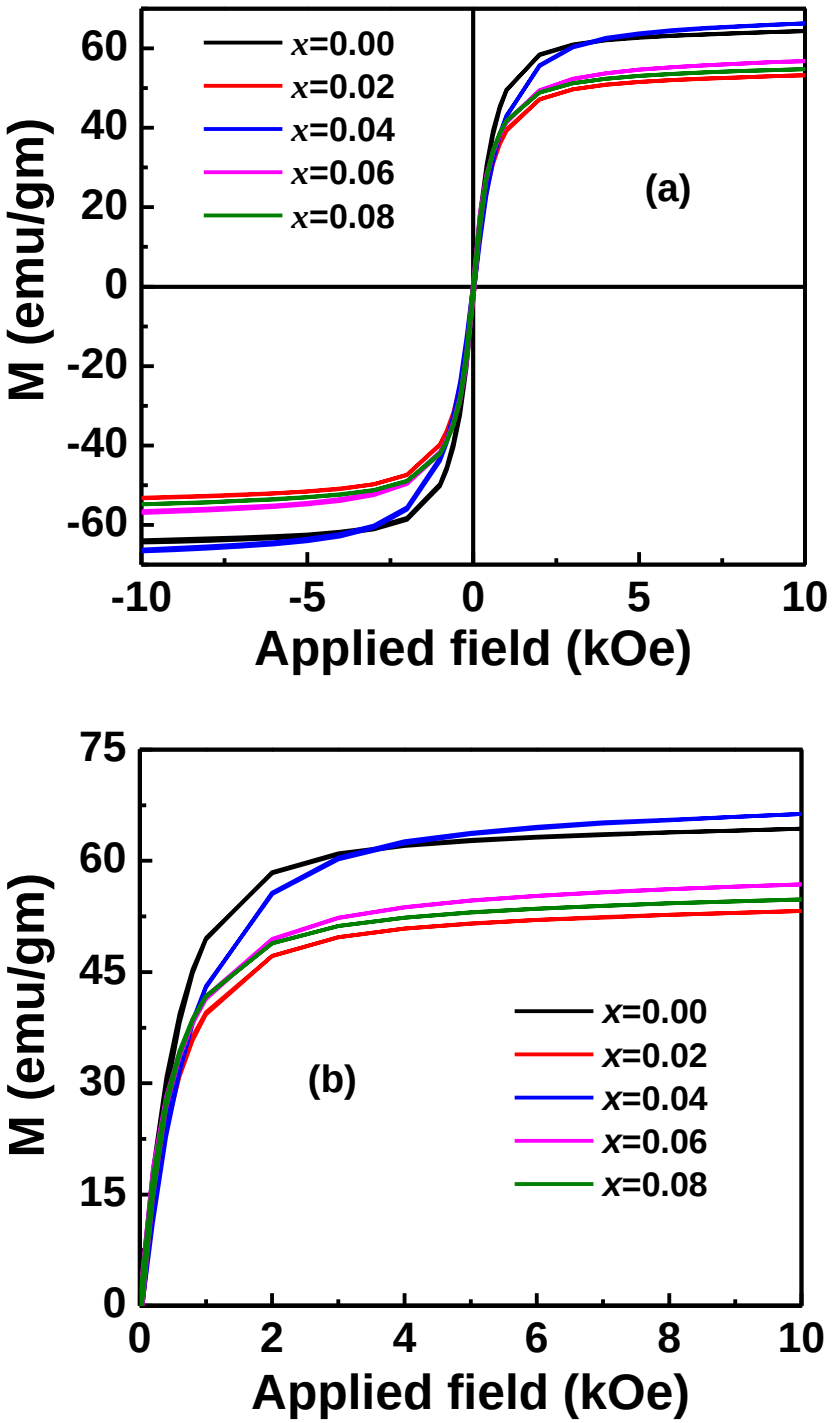

Fig. 5.8: (a) The M-H loops for $Co_{0.5}Zn_{0.5}Y_xFe_{2-x}O_4$ (x=0.00 to 0.08) compositions at T_s=1100 °C. (b) 1st quadrant of M-H loop of the samples.

The value of M_s declines with increasing Y^{3+} contents unlike at *x*=0.04. This typical behavior can be explained that the M_s is calculated by the following equation: $M_s = |M_B - M_A|$; where M_A and M_B are the magnetic moment of A and B sites. The ions Zn^{2+} and Fe^{2+} preferred in A-site where as Co^{2+}, Fe^{3+} and Y^{3+} in B-site. The net magnetic moment in the B-site decreases due to substituted diamagnetic ions Y^{3+} (μ_B=0) in place of Fe^{3+} (μ_B=5) consequently M_s reduces with increasing Y content [15]. Moreover, domain wall motion become tougher due to substitution of foreign ions Y^{3+} that possess larger ionic radius results the M_s decreases in the CZYFO ferrites [13]. The value of H_c decreases with increasing Y^{3+} content in the CZYFO except bit rises at *x*=0.02 (Table 5.2). It can be understood that the M-H loop requires more energy in magnetization and demagnetization process for substitution of Y^{3+} ions, however the domain wall energy

Table 5.2: Calculated saturation magnetization (M_s), remanent magnetization (M_r), and coercive field (H_c) of $Co_{0.5}Zn_{0.5}Y_xFe_{2-x}O_4$ (x=0.00 to 0.08) ferrites at T_s=1100°C.

Y content	**M_s (emu/gm)**	**M_r (emu/gm)**	**H_c (O_e)**
0.00	64.44	2.55	28.00
0.02	53.33	2.23	28.23
0.04	66.60	1.722	25.11
0.06	57.00	2.43	27.22
0.08	55.00	1.87	21.30

reduces due to the decreasing isotropic field with increasing Y^{3+} ions from 28.230 O_e to 21.297 O_e, might be the reason further reducing H_c at higher Y^{3+} content [16, 17]. The crystal lattice anisotropy decreasing for increasing Y^{3+} content in the CZYFO compositions contribute to decline the H_r field [18].

5.4.2 Permeability

The frequency and temperature dependent initial permeability are shown in Fig. 5.9(a) and 5.9(b), respectively. The permeability decreases gradually with Y substitution in the prepared samples and follows the similar trend. The domain rotation and domain wall displacement are influenced by the grain size variation consequently initial permeability of the samples changes [19]. Initially, the Y^{3+} ions are pinned in the grain boundaries that prevents the domain wall displacement results the initial permeability decreases for x=0.02 and 0.04. The grain sizes rises with increasing Y^{3+} ions that make the domain wall movement easier than before, accordingly the permeability increases at x>0.02 in the CZYFO ferrites.

Temperature dependent initial permeability μ' at 100 kHz with the temperature range of 30° to 250 °C is shown in Fig.5.9 (b). The value of μ' sharply decreases for a certain temperature, its known as Curie temperature (T_c) and measured T_c for different x content also be presented in Fig.5.10.

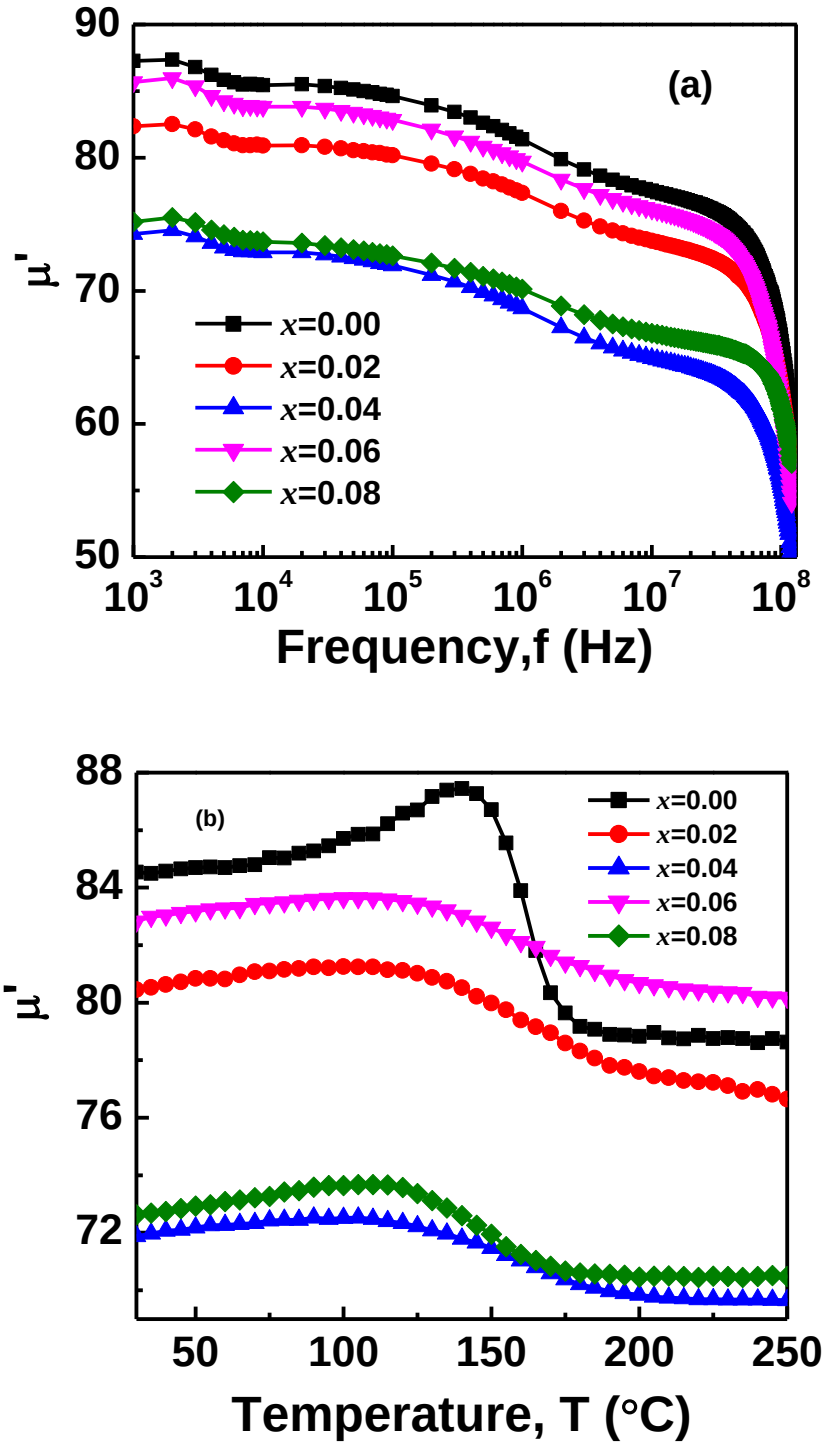

Fig.5.9: Frequency (a) and temperature (b) dependence of permeability for different composition of $Co_{0.5}Zn_{0.5}Fe_{2-x}Y_xO_4$ ferrites.

The T_c decreases with the increase in Y^{3+} ions up to x=0.06 then it rises at x=0.08. Presence of the diamagnetic Y^{3+} ions in the octahedral (B) site of CZYFO ferrites introduces magnetic dilution in the A-B interactions subsequent weakening magnetic strength that results the T_c declines with the x contents [20]. The higher Y^{3+} content enhances the size of the grains and pinned the movement of domain wall in the samples might be the reason increasing T_c at x=0.08.

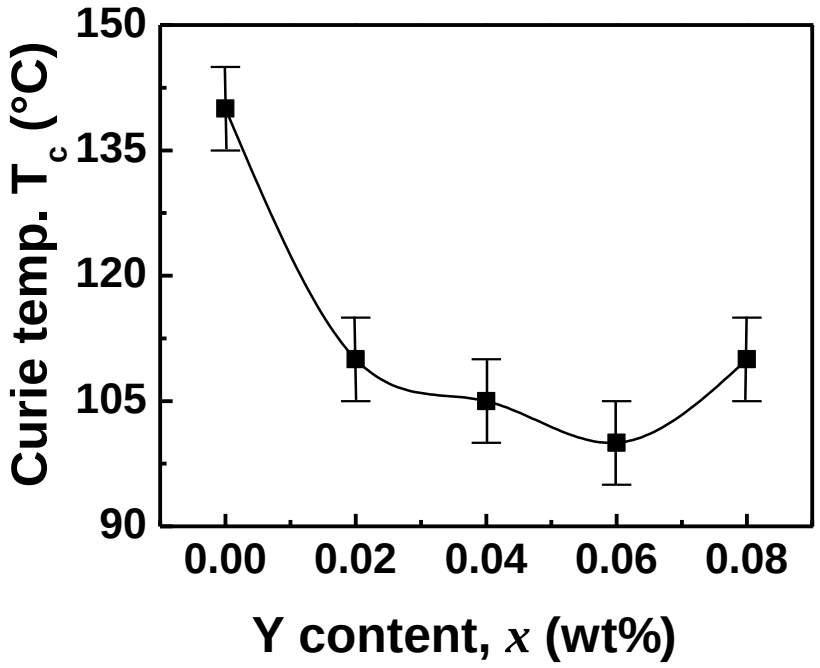

Fig. 5.10: The variation of Curie temperature (T_c) of $Co_{0.5}Zn_{0.5}Fe_{2-x}Y_xO_4$ ferrites.

5.4.3 Quality Factor:

Quality factor is an important parameter to measure the performance of a sample in practical application. Figure shows the variation of relative quality factors with frequency.

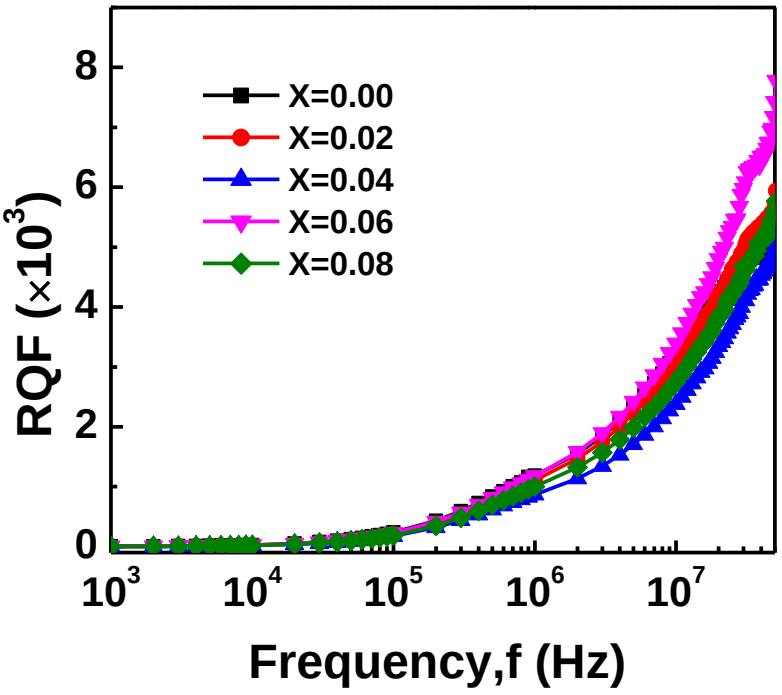

Fig.5.11: Frequency versus RQF plot for $Co_{0.5}Zn_{0.5}Y_xFe_{2-x}O_4$ ferrites.

From the figure 5.11, it have been seen that, the quality of $Co_{0.5}Zn_{0.5}Y_xFe_{2-x}O_4$ ferrites increase with frequency and in high frequencies 6% yttrium substituted ferrites shows better quality.

5.5 Electrical Properties of $Co_{0.5}Zn_{0.5}Y_xFe_{2-x}O_4$ ferrites

5.5.1 AC and DC Resistivity

The DC resistivity and AC conductivity of $Co_{0.5}Zn_{0.5}Y_xFe_{2-x}O_4$ ferrites CZYFO samples as a function of temperature and frequency have been measured by two probe measurement system as illustrated in Fig. 5.12 (a) and (b), respectively. The resistivity increases with increasing Y^{3+} ions substitution yields a peak at certain temperature and showing highest value (3.6×10^6 Ω/m) for x=0.02. Afterward it decreases with rising sample temperature and all samples show the similar trend for Y^{3+} ions substitution. The Y^{3+} ions replaces the Fe^{3+} ions in the octahedral sites of the samples that diminishes the hopping rate between Fe^{3+} and Fe^{2+} ions continuously with Y^{3+} ions substitution results the resistivity diminutions [21].

The frequency dependence of ac conductivity (σ_{ac}) of the samples has been shown in Fig. 5.12(b). The frequency dependent σ_{ac} conductivity can be represented by Jonscher's power law: [22]

$$\sigma_{ac,total}(\omega) = \sigma(0) + \sigma_{ac}(\omega) = \sigma_{dc} + A\omega^n$$

where, σ_{dc} indicates the frequency-independent conductivity or dc conductivity, 'A' is pre-exponential factor and dependent on temperature, 'n' is an exponent, dependent on both frequency and temperature in the range 0 to 1 and ω represents the angular

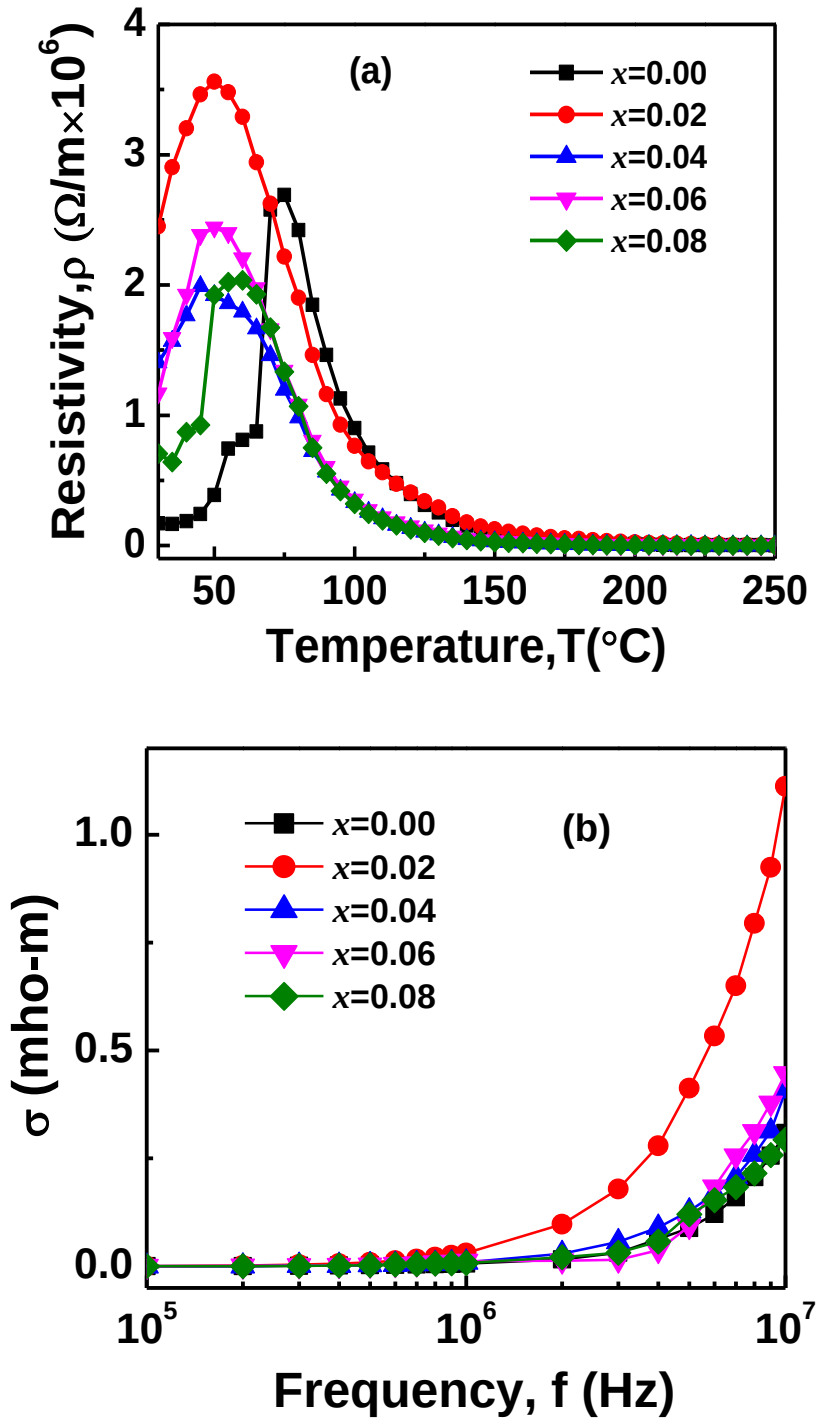

Fig. 5.12: (a) The variation of DC resistivity and (b) AC (σ_{ac}) conductivity as a function of temperature and frequency of $Co_{0.5}Zn_{0.5}Y_xFe_{2-x}O_4$ ferrites.

frequency. Frequency dependent σ_{ac} conductivity behavior of the samples can be explained by employing Maxwell–Wanger double layer model [23-25] that the ferrites contains of two layers: the layer consists of grains which are well conducting, separated by poorly conducting thin layer, forming grain boundary. The samples show different conductivity at low and high frequency regions in response of frequency of these two layers. The grain boundaries which are more active and the exchange of electrons between $Fe^{2+}$and Fe^{3+}ions is fewer attributed at the lower frequency region, while the grains activity increases with increasing the frequency by boosting the electrons hopping between $Fe^{2+}$and Fe^{3+} ions consequently an increase in hopping rate hence ac electrical conductivity rises.

5.5.2 Dielectric Relaxation Properties

The dielectric constant [$\varepsilon' = Cd/\varepsilon_0 A$, where C is the capacitance, d is the thickness, ε_0 is the permittivity in free space and A is the surface area of pellet] and loss tangent ($\tan\delta = \varepsilon''/\varepsilon'$) of the CZYFO ferrites have been calculated and shown in Fig.5.13 (a) and, (b) respectively.

The curves exhibit a sharp decrease at low frequency up to 100 kHz then bit slow drop and finally become almost zero and frequency independent at high frequency region that is common feature for spinel ferrites [26]. The behavior consistent with previously reported in various ferrites system such as Mg–Zn [27], Sm, Cr and Co substituted Mg-Zn ferrites [16, 28, 29] and Ni–Zn [30, 31].

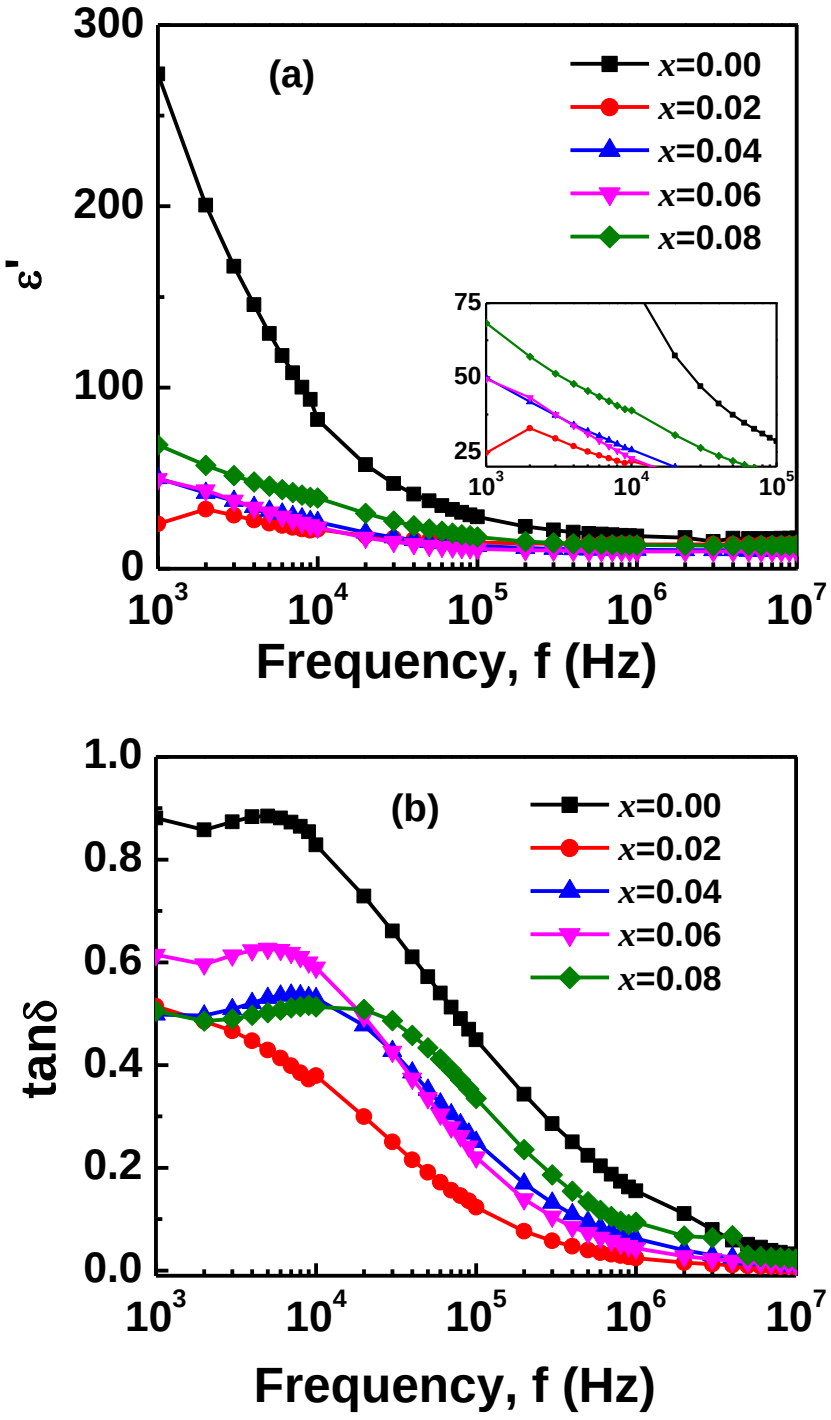

Fig. 5.13: The frequency dependence of dielectric constant (a) and dielectric loss (b) of $Co_{0.5}Zn_{0.5}Y_xFe_{2-x}O_4$; ($x$=0.00, 0.02, 0.04, 0.06, 0.08) ferrites sintered at 1100 °C measured at room temperature.

The Koops' theory can be employed to explain the frequency dependent behavior of the CZYFO that the dielectric materials contain two layers of the Maxwell–Wagner model [32, 33]. At low frequency region, the electric field up to certain frequency follows by the electron exchange between Fe^{2+} and Fe^{3+} consequently the local displacement of charges between sites in the applied field direction, which determine the polarization of the system. However, at high frequency the electron exchange between Fe^{2+} and Fe^{3+} cannot follow the applied electric field and hence reduction of the ε′ and becomes a constant value [34].

The dielectric loss of CZYFO compositions as a function of frequency is shown in Fig. 5.13 (b). The curves show a typical maximum value with a peak at certain frequency for substituted compositions. The curves reveal a maximum frequency [$\omega = 2\pi f_{max}$ and τ is the relaxation time, related to the jumping probability per unit time p by an equation $\tau=1/2p$] where the applied electric field is equal to jumps frequency between Fe^{2+} and Fe^{3+}ions at adjacent B-sites approximately [35].

5.5.3 Electric Modulus Analysis

The study of electric modulus and impedance is very important to understand the complete electrical properties of spinel ferrites. Modulus provides the information regarding the relaxation behavior and resonance frequencies, at the same time a complete contribution of microstructure resistance get from the complex impedance plot.

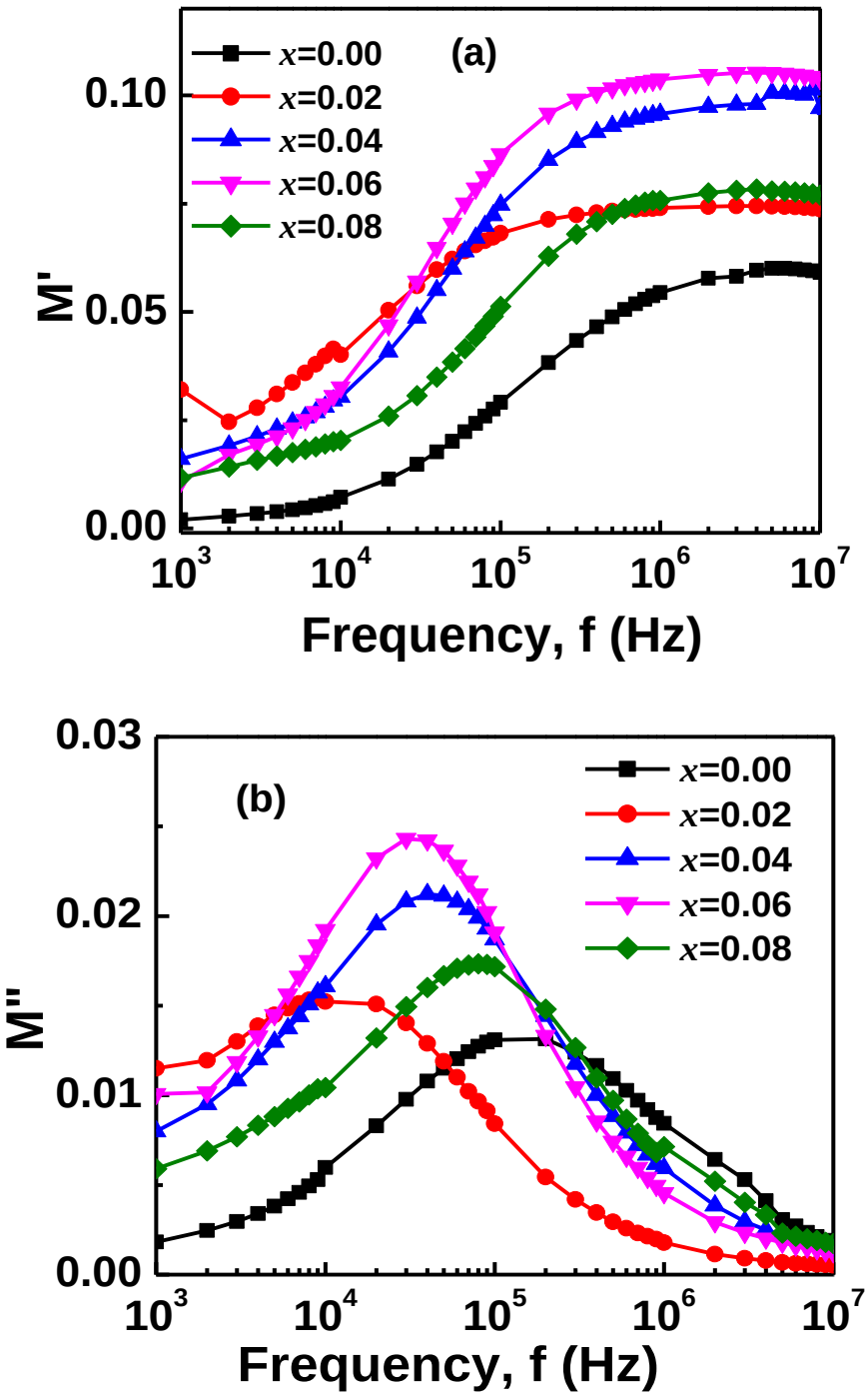

Fig. 5.14: Frequency dependent (a) real and (b) imaginary part of modulus for different Y concentration in $Co_{0.5}Zn_{0.5}Y_xFe_{2-x}O_4$; ($x$=0.00, 0.02, 0.04, 0.06, 0.08) ferrite.

Figure 5.14(a) and 5.14(b) show the real and imaginary part of modulus which determined by the following equation:

$$M' = \frac{\varepsilon'}{\varepsilon'^2+\varepsilon''^2} \quad \text{and} \quad M'' = \frac{\varepsilon''}{\varepsilon'^2+\varepsilon''^2}$$

From figure 5.14 (a), it is characterized that, in the low frequency region, the value of M', is very low and with the rise of frequency, it is continuously increasing. In high frequencies, it shows the tendency of saturation at a maximum asymptotic value. It indicates the conduction phenomena due to short range mobility of charge carriers [36].

Figure 5.14 (b) shows the variation of M" as a function of frequency, which provide the information about electrical transport mechanism, conductivity relaxation and ion dynamics. This type of modulus pattern indicates the long range of charge carriers due to hopping mechanism. The peak region indicates the transition of charge carrier from long range to short range with frequency. The shifting of the peak frequencies in the backward direction indicates the increasing relaxation time with Y^{3+} ion substitution [37].

5.5.4 Impedance Spectra and Cole-Cole Plot

The variation of Z' as a function of frequency for different Y concentration are shown in figure 5.15 (a). It can be seen that, Z' decrease with increasing frequencies and after a certain frequency it's almost constant and in low frequency region the value of Z' increase with Y substitution. The result indicates the space charge polarization effect on the materials.

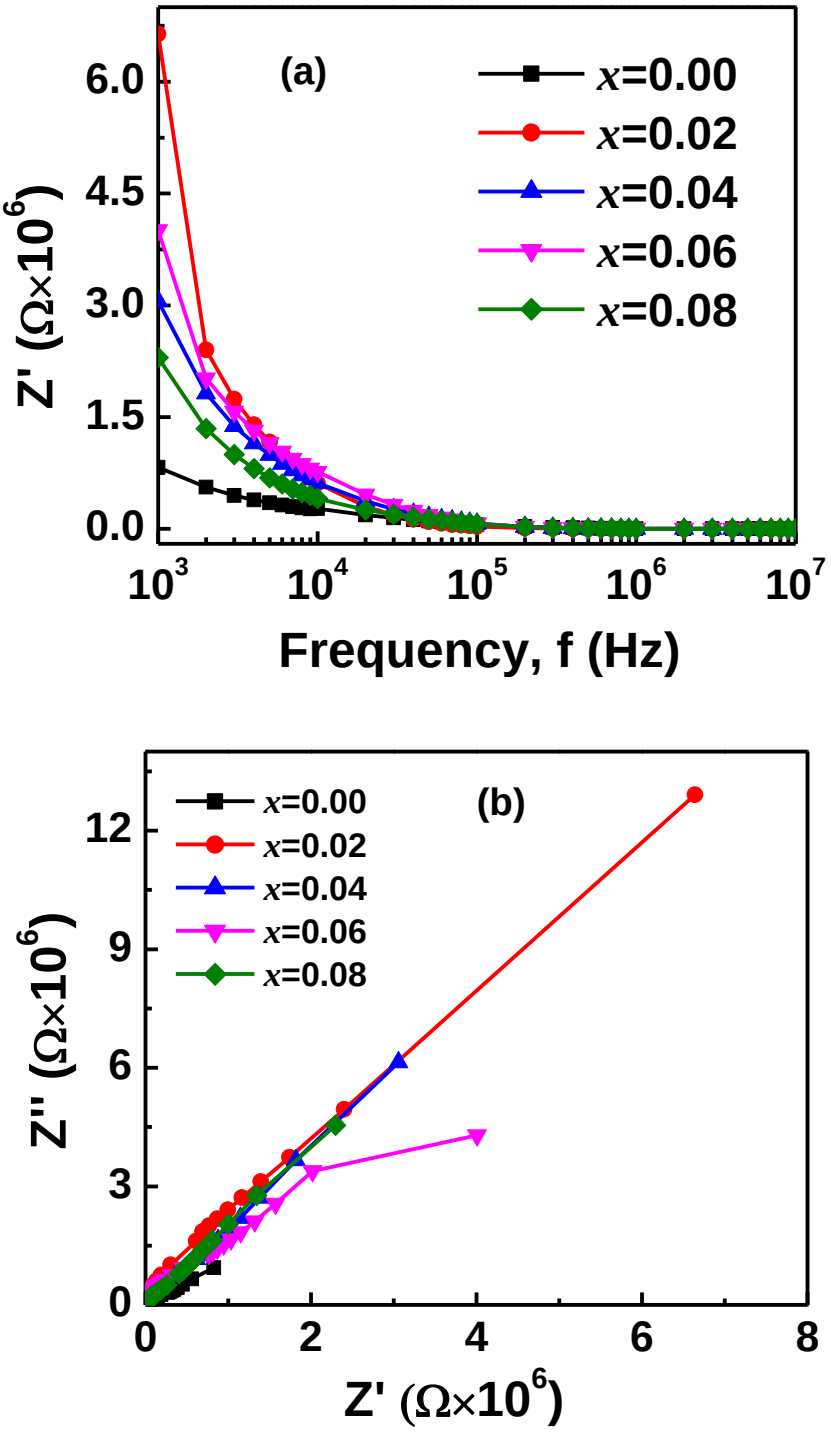

Fig. 5.15 (a): The variation of impedance real part as a function of frequency, **(b):** Cole Cole plot of $Co_{0.5}Zn_{0.5}Y_xFe_{2-x}O_4$; ($x$=0.00, 0.02, 0.04, 0.06, 0.08) ferrites.

Usually, there are two consecutive semi circles in a cole cole plot, one shows the grain boundaries resistance in low applied field and another shows the grain contribution in high field side. From Figure 5.15 (b), it have been seen that, the complex impedance plot perform only one semi-circle for all studied samples in low frequency region. It indicates the predominance of grain boundary resistance. This types of result also get by other researchers [38].

References

[1] S.T. Alone, S.E. Shirsath, R.H. Kadam, K.M. Jadhav, J. Alloys Compd. 509 (2011) 5055-5060.

[2] N.H. Vasoya, V.K. Lakhani, P.U. Sharma, K.B. Modi, R. Kumar, H.H. Joshi, J. Phys. Condens. Matter 18 (2006) 8063.

[3] M. Vanaja, G. Gnanajobitha, K. Paulkumar, S. Rajeshkumar, C. Malarkodi, G. Annadurai, J. Nanostruct. Chem. 3 (2013) 17.

[4] S.A. Mazen, M.H. Abdallah, R.I. Nakhla, H.M. Zaki, F. Metaw, Mater. Chem. Phys. 34 35 (1993) 40.

[5] J. Smit, H.P.J. Wijn, Ferrites, Wiley, NewYork, 1959.

[6] N. Rezlescu, E. Rezlescu , C. L. Sava, F. Tudorache, P.D. Popa, Phys. Stat. Sol. (a) 201 (2004) 17.

[7] J.B. Nelson, D.P. Riley, Proc. Phys. Soc. London 57 (1945) 160.

[8] O.M. Hemeda, M.M. Barakat, J. Magn. Magn. Mater. 223 (2001) 127-132.

[9] S. E. Jacobo, P. G. Bercoff, Ceramics International 42, (2016) 7664-7668.

[10] Y.Y.Meng, Z.W.Liu, H.C.Dai, H.Y.Yu, D.C.Zeng, S.Shukla, R.V.Ramanujan, PowderTechnol. 229(2012)270–275.

[11] A. Gabal, Y. M. A. Angari, J. Magn. Magn. Mater. 322 (2006) 3159-3165.

[12] ImageJ software link.

[13] Z. J. Peng, X. L. Fu, H.L. Ge, Z.Q. Fu, C.B. Wang, L.H. Qi, H.Z. Miao, J. Magn. Magn. Mater. 323 (2011) 2513-2518.

[14] X. L. Fu, H. L. Ge, Q. K. Xing, Z. J. Peng, Mater. Sci. Eng. B 176 (2011) 926-931.

[15] A. M. Pachpinde, M. M. Langade, K.S. Lohar, S. M. Patange, S.E. Shirsath, Chem. Phys. 429 (2014) 20-26.

[16] N. Lwin, R. Othman, S. Sreekantan, M. N. A. Fauzi, J. Magn. Magn. Mater. 385 (2015) 433-440.

[17] I. H. Gul, A. Z. Abbasi, F. Amin, M. Anis-ur-Rehman, A. Maqsood, Journal of Magnetism and Magnetic Materials 311 (2007) 494-499.

[18] S.E. Shirsath, B.G. Toksha, K. M. Jadhav, 2009 Materials Chemistry and Physics, 117 (2009) 163-168.

[19] X. F. Fan, H. P. Ren, Y. H. Zhang, S. H. Guo, X. L. Wang, Rare Met. 27 (2008) 287-291.

[20] I. H. Dunn, S. E. Jacobo, P.G. Bercoff, Journal of Alloys and Compounds 691 (2016) 130-137.

[21] M. Ishaque, M. A. Khan, I. Ali I, M. Athair, H. M. Khan, M. A. Iqbal, M. U. Islam, M. F. Warsi, Mater. Sci. Semi.Proces. 41 (2016) 508.

[22] A. K. Jonscher, Nature (London) 267 (1977) 673.

[23] C.G. Koops, Phys. Rev. 83 (1951) 121.

[24] J. C. Maxwell, Electricity and Magnetism, Oxford University Press, New York, 1973.

[25] K. Katsmi, S. Mamoru, I. Tatrsuo, I. Katsuya I, Bull. Chem. Soc. 48 (1975) 1764.

[26] K. W. Wagner, Am. Phys. 40 (1973) 317.

[27] M. A. El Hiti, J. Magn. Magn. Mater. 192 (1999) 305.

[28] S. F. Mansour, M. A. Abdo, S. I. El-Dek, J. Magn. Magn. Mater. 422 (2017) 105.

[29] M. Hashim, S.S. Meena, R. K. Kotnala, S. E. Shirsath, P. Bhatt, S. Kumar, E. Şentürk, R. Kumar, A. Alimuddin, N. Gupta, J. Magn. Magn. Mater. 360 (2014) 21.

[30] M. A. Ali, M. M. Uddin, M. N. I. Khan, F. U. Z. Chowdhury, S. M. Hoque, J. Magn. Magn. Mater. 424 (2017) 148.

[31] M. A. Ali, M. N. I. Khan, F. U. Z. Chowdhury, S. Akhter, M. M. Uddin, J. Sci. Res. 7 (2015) 65.

[32] C. G. Koops, Phys. Rev. 83 (1951) 121.

[33] J. C. Maxwell, Electricity and Magnetism, Oxford University Press, New York, 1973.

[34] K. Verma, A. Kumar, D. Varshney, Curr. Appl. Phys. 13 (2013) 467.

[35] V. R. K. Murthy, J. Sobhanadri, Phys. Status Solidi A, 36 (1976) 133.

[36] M.A. Ali, M.M. Uddin, M.N.I. Khan, F.-U.-Z. Chowdhury, S.M. Haque, Journal of Magnetism and Magnetic Materials 424 (2017) 148–154.

[37] K. Prabakar, S. K. Narayandass and D. Mangalaraj, Mater. Sci. Eng. B 98 (2003) 225-231.

[38] E. Pervaiz and I H Gul, Journal of Physics: Conference Series 439 (2013) 012015.

Chapter 6 : Conclusions and Suggestions for Further Research

6.3 Conclusions

6.4 Suggestions for Further Research

Chapter 6: Conclusions

6.1 Conclusions

The mixed spinel ferrite of $Co_{0.5}Zn_{0.5}Y_xFe_{2-x}O_4$, x=0.00 to 0.08 in step of 0.02 has been prepared by conventional solid state reaction technique and sintered at 1100 °C. The structural, electrical and magnetic properties have been studied.

- The XRD patterns confirm the single phase cubic spinel structure up to $x<0.06$ with a very tiny amount of $YFeO_3$ for $x\geq 0.06$. The lattice parameter decreases initially and then it increases with Y^{3+} contents. The average grain size decreases at $x= 0.02$ and then it increases with Y substitution. The theoretical lattice constant is consistent with experimental one only for the compositions with single phase region. The FESEM data confirm the uniform grain size distribution. The purity of all samples confirms from the EDS spectra.
- The DC resistivity increase after Y^{3+} substitution and the highest value get for 2% substituted yttrium and the AC conductivity found to be increased in high frequencies. The electric modulus and impedance indicate long range mobility of charge carriers and peaks separation reveal the existence of localized charge carriers with retreat from the Debye-like behavior.
- The Curie temperature decreases with lower contents of Y^{3+} and increases at higher contents endorses presence of magnetic dilution in the A-B interactions consequent weakening magnetic strength that results the T_c declines with the x contents.

- The value of saturation magnetization decreases with increasing Y^{3+} contents that indicates the domain wall motion become tougher due to substitution of foreign ions Y^{3+} that possess larger ionic radius.

Thus, for high resistivity and low losses, Y^{3+} substituted Co-Zn ferrites found to be useful in high frequency and power supply devices.

6.2 Suggestions for Further Research

- Neutron diffraction analysis may be performed for these compositions to determine the distribution of substituted Y^{3+} ions between A- and B-sites. Mossbauer spectroscopy can also be studied.
- For the domain wall motion and degree of ordering present in the samples, MFM study can carried out.

List of Publication

1 Structural, morphological, electrical and magnetic properties of Yttrium-substituted Co-Zn ferrites synthesized by double sintering technique; **M. Das**, M.N.I. Khan, M.A. Matin and M.M. Uddin, accepted to Journal of Superconductivity and Noble Magnetism (Springer, IF-1.142).

List of Conference Attended

1 Investigation of Structural, Electrical and Magnetic Properties of Y-substituted Co-Zn Ferrites Synthesized by Double Sintering Technique; **M. Das** , M. N. I. Khan , S. M. Hoque , and M. M. Uddin; International Conference on Physics, 8-10 March, 2018, organized by Bangladesh Physical Society (BSP).

2 Effect of Y^{3+} substitution on the enhancement of electrical resistivity of Co-Zn ferrites prepared by standard ceramic technique; **M. Das**, M. N. I. Khan, S. M. Hoque, and M. M. Uddin; Conference on Weather Forecasting & Advances in Physics, 11-12 May, 2018, organized by Dept. of Physics, Khulna University of Engineering & Technology (KUET).

3 Influence of Y^{3+} substitution on magnetic and electric properties of Co-Zn ferrites synthesized by conventional solid state reaction technique; **M. Das**, M. N. I. Khan, S. I. Liba, H. N. Das, M. A. Matin, M. A. Hakim, and M. M. Uddin; International Conference on Electronics and ICT, 25-26 November, 2018, organized by Bangladesh Electronic Society (BES) & Bangladesh Atomic Energy Commission (BAEC).

Journal of Superconductivity and Novel Magnetism (2019) 32:3569–3577
https://doi.org/10.1007/s10948-019-5104-6

ORIGINAL PAPER

Structural, Morphological, Electrical and Magnetic Properties of Yttrium-Substituted Co-Zn Ferrites Synthesized by Double Sintering Technique

M. Das[1] · M. N. I. Khan[2] · M. A. Matin[3] · M. M. Uddin[1]

Received: 20 February 2019 / Accepted: 3 April 2019 / Published online: 16 May 2019

Abstract
A series of rare earth Y^{3+} ion substituted Co-Zn ferrites $Co_{0.5}Zn_{0.5}Y_xFe_{2-x}O_4$ ($x = 0.00$ to 0.08 in step of 0.02) have been synthesized by conventional double sintering technique from the oxide powders of Co, Zn, Fe, and Y. The XRD, FESEM, EDS, DC resistivity, dielectric measurements, VSM, and Curie temperature (T_c) analysis have been used to investigate structural, morphological, electrical, and magnetic properties. Single phase of cubic spinel structure has been confirmed up to $x < 0.06$, and a small amount of secondary phase $YFeO_3$ has also been detected for $x > 0.06$. The lattice parameter initially decreases than increases with yttrium concentrations. The FESEM image shows that the grains and grain boundaries are distinct and uniformly distributed and the purity has also been endorsed from the EDS spectra. The average grain size decreases at $x = 0.02$ and then increases with Y substitution. The long range mobility of charge carriers and presence of localized charge carriers with retreat from the Debye-like behavior in the compositions have been explored using electric modulus and impedance. The magnetic strength diminishes owing to existence of magnetic dilution in the A-B interactions subsequent to the T_c declines with the x contents. The value of saturation magnetization decreases with increasing Y^{3+} contents that indicates that the domain wall motion become tougher due to substitution of foreign ions Y^{3+} that possess larger ionic radius. Therefore, the Y^{3+} substituted $Co_{0.5}Zn_{0.5}Y_xFe_{2-x}O_4$ ($x = 0.00$ to 0.08 in step of 0.02) ferrites with high resistivity and low losses has implications to be used in high frequency and power supply devices applications.

Keywords Co-Zn ferrites · Rare-earth ions substitution · DC resistivity · Dielectric properties · Magnetic properties

PACS 75.50.Bb · 75.50.Gg · 75.60.Ej · 75.50.Ss

1 Introduction

Ferrite materials have drawn much attention to the scientific community as well as in industrial applications due to their unique properties in both nano and bulk form even many years afterward since their innovation. Huge effort has been paid by the scientists, researchers, technologist, and engineers to uncover new commercial applications of the ferrites with tremendous properties [1, 2].

Among the spinel ferrites the combination of Co-Zn has attracted huge interest because of its high electrical resistivity, mechanical hardness, chemical stability, and reasonable cost [3]. The remarkable properties of Co-Zn make them as an apposite choice for applications in microwave devices, memory devices, and transformer cores [4]. The Co-Zn ferrite has a mixed spinel structure with general formula of $(Zn^{2+}Fe^{2+})$ $[Co^{2+}Fe^{3+}]$ O_4^{2-}, where Zn^{2+} and Fe^{2+} occupy A site and Co^{2+} and Fe^{3+} occupy B site [1]. The properties of ferrites are influenced by numerous issues such as method and conditions of preparation as well as the amount and type of additives. The implantation of rare earth ions can remarkably tuned the structural, electrical, and magnetic behavior of

✉ M. M. Uddin
mohi_cuet@yahoo.com

[1] Department of Physics, Chittagong University of Engineering and Technology (CUET), Chattogram 4349, Bangladesh

[2] Materials Science Division, Atomic Energy Center, Dhaka 1000, Bangladesh

[3] Department of Glass and Ceramic Engineering, Bangladesh University of Engineering and Technology (BUET), Dhaka 1000, Bangladesh

ferrites due to their larger ionic radius [5–11]. Substitution of different ions in the ferrites modifies cation dissemination at A site and B site for either divalent cation (M^{2+} of MFe_2O_4) or Fe^{3+} ions. The structural, electrical, and soft magnetic properties of Co-Zn ferrites have been changed by substituted Ni [12], Si [13], and Mo [11].

The electron hopping between Fe^{2+} (which is formed during sintering process [14, 15]) and Fe^{3+}ions at octahedral (B) site [16] is mainly contributed in the electrical conductivity of spinel ferrites. However, the rare-earth ions occupy the octahedral (B) site that reduces the electron hopping by limiting the motion of Fe^{2+}, consequently the resistivity upturns [8]. Some rare-earth ions have already been substituted in the Co-Zn ferrites such as Gd^{3+} [10]and Ho^{3+} [9]. We intended to enhance the electrical resistivity of the Co-Zn ferrites with $Co_{0.5}Zn_{0.5}Y_xFe_{2-x}O_4$ ($x = 0.00$ to 0.08 in step of 0.02) composition by substituted Y^{3+} for Fe^{3+} and a significant characteristic (rises resistivity) is expected to be changed with retaining magnetic properties unaffected even enhanced for applications in the high-frequency devices. In addition, the Yttrium (Y) has already been substituted in the ferrites Ni-Zn, Mg, Mg-Zn, and Co [17–25]. To the best of our knowledge, there is no report on the effect of Y substitution in the Co-Zn ferrite yet. Therefore, we report here the Y^{3+} ions substation for Fe^{3+} in the Co-Zn ferrites with the compositions of $Co_{0.5}Zn_{0.5}Y_xFe_{2-x}O_4$ (where $x = 0.00$ to 0.08 with a step of 0.02) that would be provided fundamental knowledge to be implemented in practical applications.

1.1 Experimental Details

The samples of Y^{3+} substituted Co-Zn ferrites with a basic composition of $Co_{0.5}Zn_{0.5}Y_xFe_{2-x}O_4$ ($0.00 \le x \le 0.08$; in a step of 0.02) have been fabricated by double sintering technique. The raw materials are cobalt oxide (Co_3O_4), zinc oxide (ZnO), iron oxide (Fe_2O_3), and yttrium oxides (Y_2O_3) with a purity of 99.98% obtain from E-Merck, Germany. The oxide powders are weighed using their stoichiometric ratio for particular composition. The powders are homogeneous mixed and then loosely pressed to make biscuit-like shape that are calcined at 650 °C for 4 h in a muffle furnace. The calcined powders are then crushed and grinded again for 1 h after removing from the furnace. A 5% polyvinyl alcohol solution are added to the powders with as a binder and different shapes are made by pressing with a hydraulic press using 15 kN and 10 kN pressure for ring and pellet samples, respectively. Finally, these samples are sintered in air at 1100 °C for 4 h into a muffle furnace with an increasing rate of 5 °C/min and cooled down to the room temperature naturally. The characterization of samples has been performed using X-ray diffraction (XRD) (Philips X'pert PRO X-ray diffractometer (PW3040) with Cu-K_α radiation ($\lambda = 1.5405$ Å)), and conductivity, dielectric constant (Wayne Kerr precision impedance analyzer (6500B)),

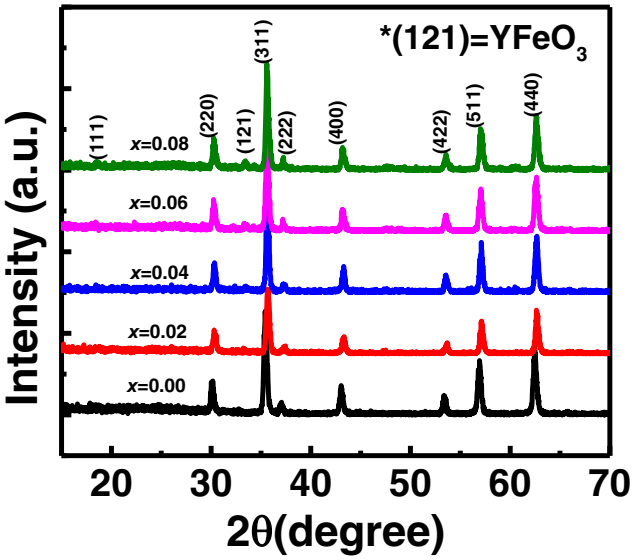

Fig. 1 The XRD patterns of Y^{3+} substituted $Co_{0.5}Zn_{0.5}Y_xFe_{2-x}O_4$ ferrite samples ($x = 0.00$, 0.02, 0.04, 0.06, 0.08)

dielectric loss tangent, electric modulus, impedance, permeability, and quality factor have been measured with a drive voltage 0.5 V at room temperature. The magnetic properties of the samples have also been carried out using a vibrating sample magnetometer (VSM) (EV-9, Microsense LLC, USA). The dc resistivity and T_c in the range of 30 to 250 °C has been determined by the two probe measurement system.

2 Results and Discussion

2.1 Structural Properties

The X-ray diffraction (XRD) patterns of Y-substituted Co-Zn ferrites with the chemical composition, $Co_{0.5}Zn_{0.5}Y_xFe_{2-x}O_4$

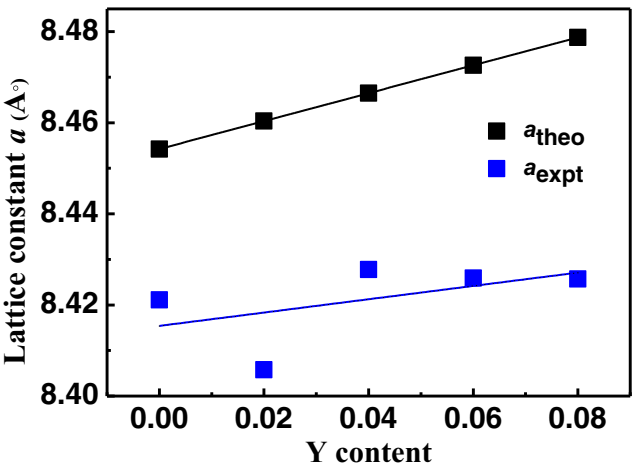

Fig. 2 The variation of theoretical lattice constant (a_{theo}) and experimental (a_{expt}) with Y content at $T_s = 1100$ °C and solid line represents linear fitting

Table 1 The chemical formula, cation distribution, ionic radius of A and B-sites, and theoretical a_{th}(Å) and experimental a_{exp}(Å) lattice parameter

Content, x	Chemical formula	A site	B site	r_A(Å)	r_B(Å)	a_{th}(Å)	a_{exp}(Å)
0.0	$Co_{0.5}Zn_{0.5}Fe_2O_4$	$Fe_{0.5}Zn_{0.5}$	$Fe_{1.5}Co_{0.5}$	0.705	0.6825	8.454235	8.42113
0.02	$Co_{0.5}Zn_{0.5}Fe_{1.98}Y_{0.02}O_4$	$Fe_{0.5}Zn_{0.5}$	$[Fe_{1.48}Co_{0.5}Y_{0.02}]O_4^{2-}$	0.705	0.6848	8.460366	8.40578
0.04	$Co_{0.5}Zn_{0.5}Fe_{1.96}Y_{0.04}O_4$	$Fe_{0.5}Zn_{0.5}$	$[Fe_{1.46}Co_{0.5}Y_{0.04}]O_4^{2-}$	0.705	0.6871	8.466496	8.42779
0.06	$Co_{0.5}Zn_{0.5}Fe_{1.94}Y_{0.06}O_4$	$Fe_{0.5}Zn_{0.5}$	$[Fe_{1.44}Co_{0.5}Y_{0.06}]O_4^{2-}$	0.705	0.6894	8.472627	8.4259
0.08	$Co_{0.5}Zn_{0.5}Fe_{1.92}Y_{0.08}O_4$	$Fe_{0.5}Zn_{0.5}$	$[Fe_{1.42}Co_{0.5}Y_{0.06}]O_4^{2-}$	0.705	0.6917	8.478758	8.42569

(CZYFO) ($0.00 \leq x \leq 0.08$) sintered at 1100 °C are depicted in Fig. 1. The creation of cubic spinel structure has been confirmed from the well-defined diffraction peaks in the planes. The samples show sole phase cubic spinel structure up to $x = 0.04$ and at $x > 0.06$, a slight amount of secondary phase ($YFeO_3$) in the plane (121) has also been identified. The similar extra phase recognized (121) reflection at $2\theta = 33.1°$ for $YFeO_3$ according to ICDD PDF #39-1489 [20]. The similar peak has been reported that this secondary phase confirms the solubility limit of rare earth ions (Y^{3+}) and Fe^{3+} ions in the ferrites [26, 27].

The lattice constant (a) has been calculated using the formula, $a = d\sqrt{h^2 + k^2 + l^2}$, where h, k, and l are the Miller indices of the crystal planes that is used for all peaks of the samples. The Nelson-Riley (N-R) extrapolation scheme has been used to evaluate lattice constants, the N-R function, $F(\theta)$, is given as $F(\theta) = \frac{1}{2}\left[\frac{\cos^2\theta}{\sin\theta} + \frac{\cos^2\theta}{\theta}\right]$ [28]. The exact value

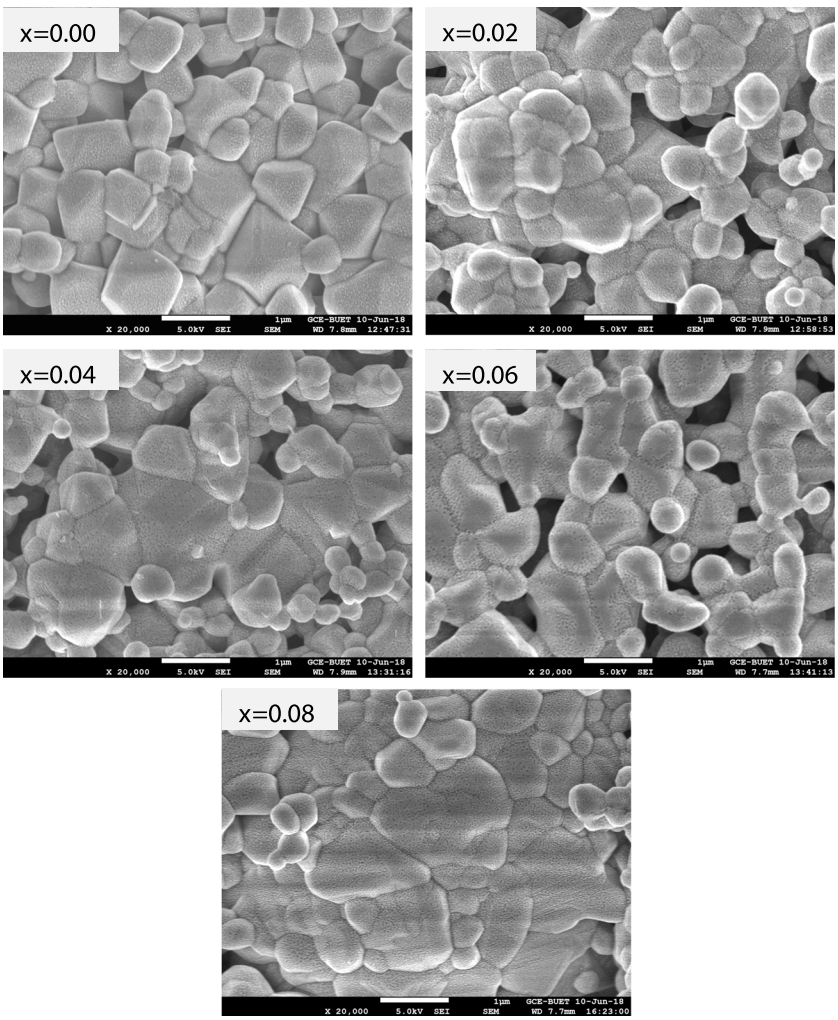

Fig. 3 FESEM micrographs of $Co_{0.5}Zn_{0.5}Y_xFe_{2-x}O_4$; ($x = 0.00$, 0.02, 0.04, 0.06, 0.08) with T_s = 1100 °C at room temperature

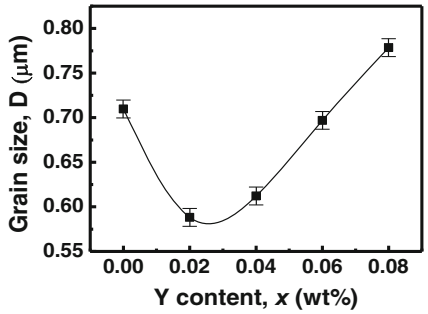

Fig. 4 The variation of grain size with Y^{3+} substitution of $Co_{0.5}Zn_{0.5}Y_xFe_{2-x}O_4$; ($x = 0.00$, 0.02, 0.04, 0.06, 0.08) ferrite with $T_s = 1100$ °C at room temperature

of a is obtained at y-axis cut point from the least square fit straight line in the a vs. $F(\theta)$ plot. The theoretical (a_{theo}) and experimental (a_{expt}) lattice parameters as a function of Y content are represented in Fig. 2. The results are in good agreement with Vegard's law [29].

The theoretical lattice constant of $Co_{0.5}Zn_{0.5}Y_xFe_{2-x}O_4$ ($0.00 \le x \le 0.08$) can be calculated from the equation, $a_{th} = \frac{8}{3\sqrt{3}}[(r_A + R_0) + \sqrt{3}(r_B + R_0)]$, where r_A is the ionic radius of tetrahedral A site, r_B is the ionic radius of octahedral B site, and R_0 is the ionic radius of oxygen ion (1.32 Å) [30, 31]. The chemical formula for the cation distribution of Y substituted Co-Zn ferrite is as follows $[Fe_{0.5}^{2+}Zn_{0.5}^{2+}]$ $[Fe_{1-x}^{3+}Co_{0.5}^{2+}Y_x^{3+}]O_4^{2-}$, where $[Fe_{0.5}^{2+}Zn_{0.5}^{2+}]$ and $[Fe_{1-x}^{3+}Co_{0.5}^{2+}Y_x^{3+}]O_4^{2-}$ contribute in A and B site, respectively. The radius of individual ions are of $r_{Zn} = 0.74$ Å, $r_{Co} = 0.745$ Å, $r_{Fe} = 0.645$ Å, and $r_Y = 0.95$ Å. The ionic radius of Y^{3+} ion is larger than that of Fe^{3+}, results the lattice parameter of the ferrites increases that is consistent with reported values [32] (Table 1).

The average values of a_{theo} and a_{expt} have been measured (square) and fit the data (solid line) is shown in Fig. 2 and found to be 8.4542 and 8.4154 Å, respectively. The obtained values are very close with 0.5% variation that approves validity of our calculation.

The surface morphology or microstructure study of ferrite samples are investigated by the FESEM for ruptured surfaces at room temperature as shown in Fig. 3. The FESEM images reveal that the samples are packed, crack-free with homogeneous grain distribution having clear grain boundaries throughout the samples. The ferrites attain a uniform grain size distribution owing to homogeneous distribution of the driving force of grain boundary in each grain [33]. The variation of grain size has significant impression on the electric and magnetic properties of a ferrite.

The grain size has been measured using the imageJ software [34] and linear intercept method by including adequately enormous number of grains from surface micrographs of the samples. The Y content-dependent grain size of the samples is illustrated in Fig. 4. The grain sizes initially decrease with increasing Y^{3+} ions content at $x = 0.02$ and then it almost linearly increases at $x > 0.02$. The manner of grain growth in the samples strongly depends on the force between driving force for the grain boundary movement and the impeding force exerted by pores [33].

The larger bonding energy of Y^{3+}-O^{2-} than that of Fe^{3+}-O^{2-} that requires more energy in mass transfer process of impeded $YFeO_3$ in the grain boundaries consequently the grain size decreases initially (Fig. 4) [35]. Later on, some divalent Fe^{2+} ions are replaced by the Y^{3+} ions in the grain boundaries results the grain size rises with increasing Y^{3+} substitution to balance the electric charge for vicinity of metallic charge

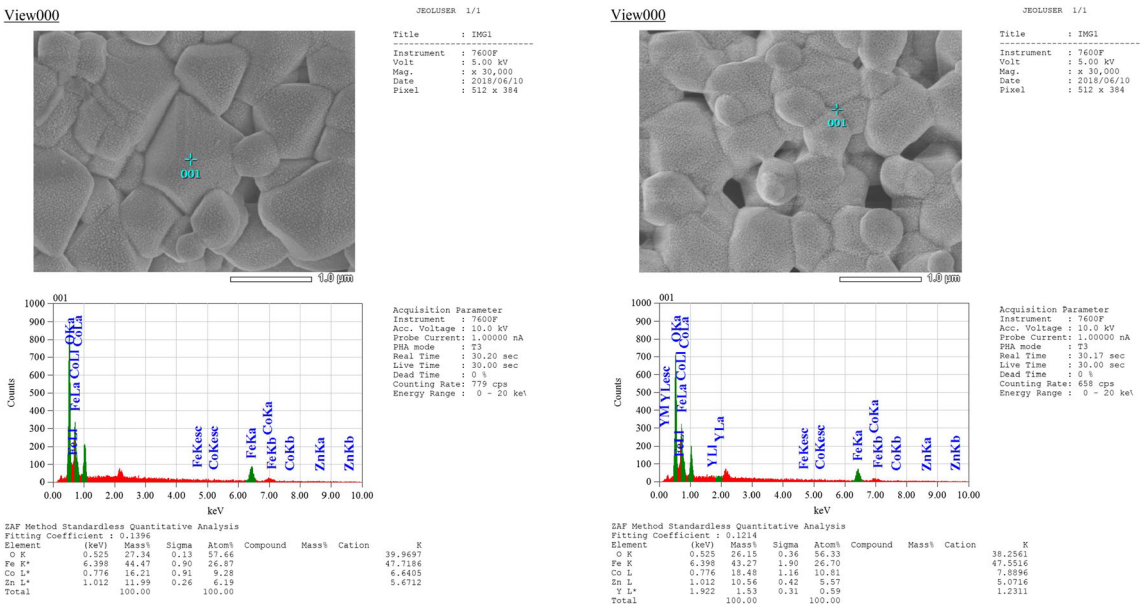

Fig. 5 The EDS pattern of $Co_{0.5}Zn_{0.5}Y_xFe_{2-x}O_4$ ferrites for $x = 0.00$ and 0.02 with $T_s = 1100$ °C at room temperature

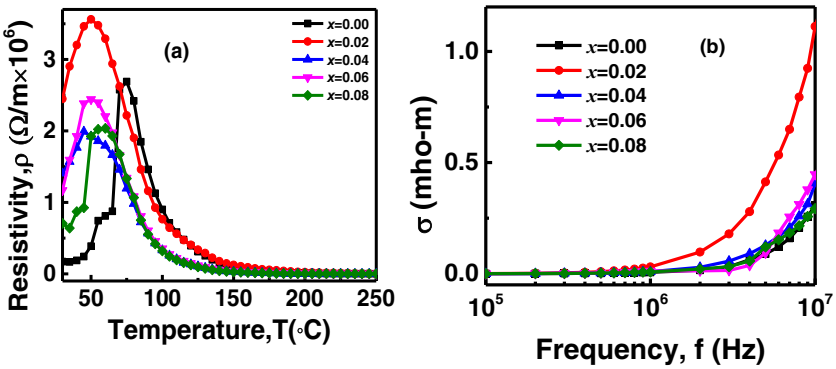

Fig. 6 **a** The variation of DC resistivity and **b** AC (σ_{ac}) conductivity as a function of temperature and frequency, respectively

vacancies [36]. The electron dispersive spectroscopy (EDS) patterns of the CZYFO ferrites for $x = 0.00$ and $x = 0.02$ are presented in Fig. 5. The peaks obtain for the elements Co, Zn, Fe, Y, and O indicate the purity of the samples.

2.2 Electrical Properties

2.2.1 Frequency Dependence of DC Resistivity and AC Conductivity

The DC resistivity and AC conductivity of CZYFO samples as a function of temperature and frequency have been measured by two probe measurement system as illustrated in Fig. 6a, b, respectively. The resistivity increases with increasing Y^{3+} ions substitution yields a peak at certain temperature and showing highest value (3.6×10^6 Ω/m) for $x = 0.02$. Afterward, it decreases with rising sample temperature and all samples show the similar trend for Y^{3+} ions substitution. The Y^{3+} ions replaces the Fe^{3+} ions in the octahedral sites of the samples that diminishes the hopping rate between Fe^{3+} and Fe^{2+} ions continuously with Y^{3+} ions substitution results the resistivity diminutions [20].

The frequency dependence of ac conductivity (σ_{ac}) of the samples is shown in Fig. 6b. The frequency dependent σ_{ac} conductivity can be represented by Jonscher's power law: [37]

$$\sigma_{ac,total}(\omega) = \sigma(0) + \sigma_{ac}(\omega) = \sigma_{dc} + A\omega^n$$

where, σ_{dc} indicates the frequency-independent conductivity or dc conductivity, "A" is pre-exponential factor and dependent on temperature, "n" is an exponent, dependent on both frequency and temperature in the range 0 to 1, and ω represents the angular frequency. Frequency-dependent σ_{ac} conductivity behavior of the samples can be explained by employing Maxwell–Wanger double layer model [38–40] that the ferrites contains of two layers: the layer consists of grains which are well conducting, separated by poorly conducting thin layer, forming grain boundary. The samples show different conductivity at low- and high-frequency regions in response of frequency of these two layers. The grain boundaries are more active and the exchange of electrons between $Fe^{2+}$and Fe^{3+}ions is fewer attributed at the lower frequency region, while the grain activity increases with increasing the frequency by boosting the electrons hopping between $Fe^{2+}$and Fe^{3+} ions consequently an increase in hopping rate hence ac electrical conductivity rises.

2.3 Frequency Dependence of Dielectric Constant and Dielectric Loss

The dielectric constant [$\varepsilon' = Cd/\varepsilon_0 A$, where C is the capacitance, d is the thickness, ε_0 is the permittivity in free space, and A is the surface area of pellet] and loss tangent ($\tan\delta = \varepsilon''/\varepsilon'$) of the CZYFO ferrites are calculated and shown in Fig. 7a, b, respectively.

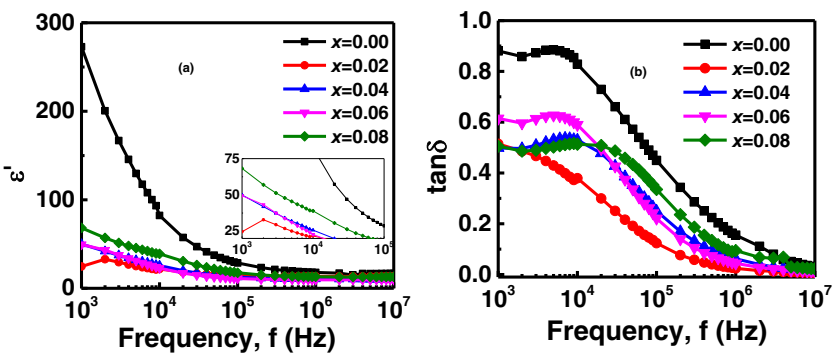

Fig. 7 The frequency dependence of dielectric constant (**a**) and dielectric loss (**b**) of $Co_{0.5}Zn_{0.5}Y_xFe_{2-x}O_4$; ($x = 0.00$, 0.02, 0.04, 0.06, 0.08) ferrites at room temperature

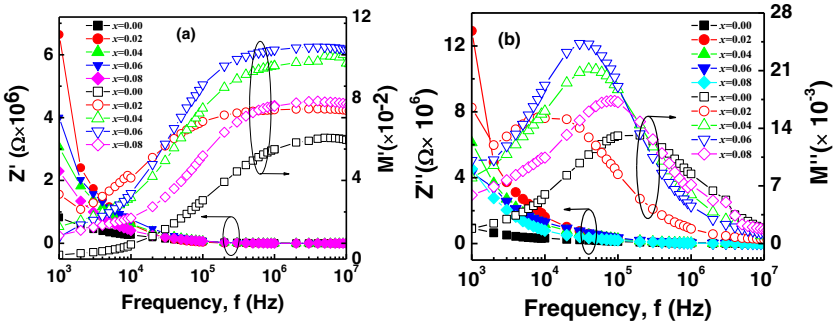

Fig. 8 Frequency-dependent **a** real part of impedance (Z') and electric modulus (M') **b** imaginary part of impedance (Z'') and electric modulus (M'') of $Co_{0.5}Zn_{0.5}Y_xFe_{2-x}O_4$; ($x = 0.00$, 0.02, 0.04, 0.06, 0.08) ferrites at $T_s = 1100$ °C measured at room temperature

The curves exhibit a sharp decrease at low frequency up to 100 kHz then bit slow drop and finally become almost zero and frequency independent at high-frequency region that is common feature for spinel ferrites (Fig. 7a) [41]. The behavior consistent previously reported in various ferrites system such as Mg–Zn [42], Sm, Cr, and Co substituted Mg-Zn ferrites [16, 43, 44] and Ni–Zn [45, 46]. The Koops' theory can be employed to explain the frequency-dependent behavior of the CZYFO that the dielectric materials contain two layers of the Maxwell–Wagner model [38, 39]. At low-frequency region, the electric field up to certain frequency follows the electron exchange between Fe^{2+} and Fe^{3+}; consequently, the local displacement of charges between sites in the applied field direction determines the polarization of the system. However, at high frequency, the electron exchange between Fe^{2+} and Fe^{3+} cannot follow the applied electric field and hence reduction of the ε' and becomes a constant value [47].

The dielectric loss of CZYFO compositions as a function of frequency is shown in Fig. 7b. The curves show a typical maximum value with a peak at certain frequency for substituted compositions. The curves reveal a maximum frequency [$\omega = 2\pi f_{max}$ and τ is the relaxation time, related to the jumping probability per unit time p by an equation $\tau = 1/2p$] where the applied electric field is equal to jumps frequency between Fe^{2+} and Fe^{3+}ions at adjacent B sites approximately [48].

2.3.1 Study of Impedance and Electric Modulus

The electrical response of the materials neither homogenous nor inhomogeneous and the electrical relaxation in electronically and ionically accompanying materials as a microscopic property of the materials has been studied meritoriously by the complex electric modulus [49]. Frequency dependence of real part of electric modulus (M') and impedance (Z') for the samples sintered at $T_s = 1100$ °C is illustrated in Fig. 8a. The value of M' shows a maximum at high-frequency region and reaching to zero at low frequency demonstrating the electrode polarization contribution is negligible in the prepared ferrites [50]. It is observed that the value of Z' declines monotonically with increasing frequency (Fig. 8a). The dispersion pattern of the Z' is observed with various Y contents in low-frequency region followed by a plateau at high-frequency region. The curves coalesce with approaching zero value that represents the Z' is independent of frequency. At higher frequency region, the space charges have slighter time to relax results the recombination is faster that diminishes the space charge polarization prominent to a combine of the curves of all the samples at different x contents (Fig. 8a).

The frequency-dependent imaginary part of electric modulus M'' [the complex electric modulus $M^* = M' + jM''$, $M' = \varepsilon'/(\varepsilon'^2 + \varepsilon''^2)$ and $M'' = \varepsilon''/(\varepsilon'^2 + \varepsilon''^2)$] and impedance ($Z''$) of CZYFO is presented in Fig. 8b. The relaxation process is either due to short or long-range movement of charge carriers, the smallest capacitance, and the largest resistance can be understood using the values of M'' of the samples [51]. The curves represent that the peaks does not occur at the same frequency results the process is long range according to Sinclair and West theory [51]. The peaks separation reveals the presence of localized charge carriers and curves are departure from Debye-like behavior.

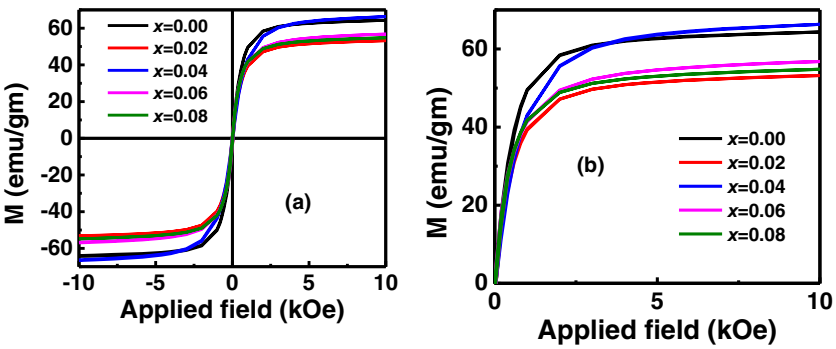

Fig. 9 **a** the M-H loops for $Co_{0.5}Zn_{0.5}Y_xFe_{2-x}O_4$ ($x = 0.00$ to 0.08) compositions at $T_s =$ 1100 °C. **b** 1st quadrant of M-H loop of CZYFO compositions

Table 2 Calculated saturation magnetization (M_s), remanent magnetization (M_r), and coercive field (H_c) of $Co_{0.5}Zn_{0.5}Y_xFe_{2-x}O_4$ (x = 0.00 to 0.08) ferrites at T_s = 1100 °C

Y content	M_s (emu/g)	M_r (emu/g)	H_c (O_e)
0.00	64.44	2.55	28.00
0.02	53.33	2.23	28.23
0.04	66.60	1.722	25.11
0.06	57.00	2.43	27.22
0.08	55.00	1.87	21.30

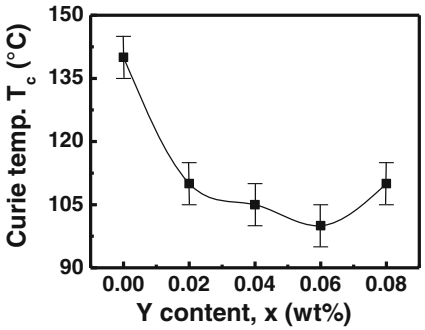

Fig. 11 The variation of T_c of $Co_{0.5}Zn_{0.5}Fe_{2-x}Y_xO_4$ ferrites

2.4 Magnetic Properties

The room temperature static applied magnetic field, H (up to 10 kOe) magnetization hysteresis loops and its first quadrant of the $Co_{0.5}Zn_{0.5}Y_xFe_{2-x}O_4$; ($x$ = 0.00, 0.02, 0.04, 0.06, 0.08) compositions sintered at 1100 °C are shown in Fig. 9. The values of saturation magnetization (M_s), remanent magnetization (M_r), and coercive field (H_c) of the samples are calculated and presented in Table 2. The value of magnetization upsurges with increasing applied magnetic field up to a certain field then it becomes saturated.

The value of M_s declines with increasing Y^{3+} contents unlike at x = 0.04. This typical behavior can be explained that the M_s is calculated by the following equation: $M_s = |M_B - M_A|$; where M_A and M_B are the magnetic moment of A and B sites. The ions Zn^{2+} and Fe^{2+} preferred in A site where as Co^{2+}, Fe^{3+}, and Y^{3+} in B site. The net magnetic moment in the B site decreases due to substituted diamagnetic ions Y^{3+} (μ_B = 0) in place of Fe^{3+} (μ_B = 5) consequently M_s reduces with increasing Y content [52]. Moreover, domain wall motion becomes tougher due to substitution of foreign ions Y^{3+} that possesses larger ionic radius which results the M_s to decrease in the CZYFO ferrites [35]. The value of H_c decreases with increasing Y^{3+} content in the CZYFO except bit rises at x = 0.02 (Table 2). It can be understood that the M-H loop requires more energy in magnetization and demagnetization process for substitution of Y^{3+} ions; however, the domain wall energy reduces due to the decreasing isotropic field with increasing Y^{3+} ions from 28.230 O_e to 21.297 O_e, might be the reason further reducing H_c at higher Y^{3+} content [53, 54]. The crystal lattice anisotropy decreasing for increasing Y^{3+} content in the CZYFO compositions contribute to decline the M_r field [55].

The frequency- and temperature-dependent initial permeability is shown in Fig. 10a and b, respectively. The permeability decreases gradually with Y substitution in the prepared samples and follows the similar trend. The domain rotation and domain wall displacement are influenced by the grain size variation consequently initial permeability of the samples changes [56]. Initially, the Y^{3+} ions are pinned in the grain boundaries that prevents the domain wall displacement resulting the initial permeability decreases for x = 0.02 and 0.04. The grain sizes rises with increasing Y^{3+} ions that make the domain wall movement easier than before, accordingly the permeability increases at x > 0.04 in the CZYFO ferrites.

Temperature-dependent initial permeability μ' at 100 kHz with the temperature range of 30° to 250 °C is shown in Fig. 10b. The value of μ' sharply decreases for a certain temperature, which is known as Curie temperature (T_c), and measured T_c for different x content also are be presented in Fig. 11.

The T_c decreases with the increase in Y^{3+} ions up to x = 0.06 then it rises at x = 0.08. Presence of the diamagnetic Y^{3+} ions in the octahedral (B) site of CZYFO ferrites introduces magnetic dilution in the A-B interactions of subsequent weakening magnetic strength that results the T_c to decline with the x contents [57]. The higher Y^{3+} content enhances the size of the grains and pinned the movement of domain wall in the samples that might be the reason for the increasing T_c at x = 0.08.

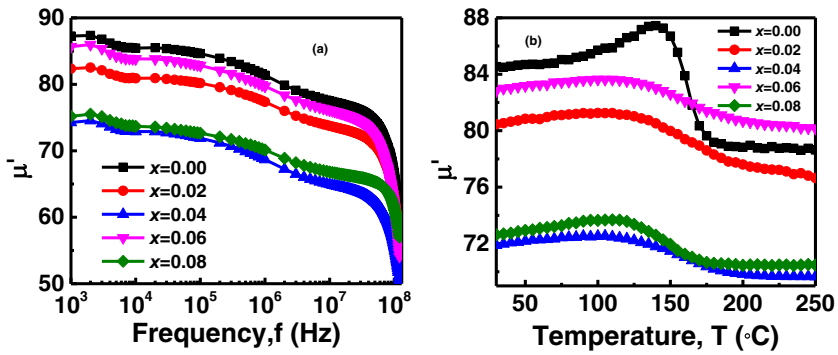

Fig. 10 Frequency (**a**) and temperature (**b**) dependence of permeability for different composition of $Co_{0.5}Zn_{0.5}Fe_{2-x}Y_xO_4$ ferrites

3 Conclusions

The mixed spinel ferrite of $Co_{0.5}Zn_{0.5}Y_xFe_{2-x}O_4$, $x = 0.00$ to 0.08 in step of 0.02 has been prepared by conventional solid state reaction technique and sintered at 1100 °C. The structural, electrical, and magnetic properties have been studied. The XRD patterns confirm the single phase cubic spinel structure up to $x < 0.06$ with a very tiny amount of $YFeO_3$ for $x \geq 0.06$. The lattice parameter decreases initially and then it increases with Y^{3+} contents. The average grain size decreases at $x = 0.02$ and then it increases with Y substitution. The theoretical lattice constant is consistent with experimental one only for the compositions with single-phase region. The purity of the samples endorses from the EDS spectra. The DC resistivity increases after Y^{3+} substitution and the highest value get for 2% substituted yttrium and the AC conductivity found to be increased in high frequencies. The electric modulus and impedance indicate long range mobility of charge carriers and peak separation reveal the existence of localized charge carriers with retreat from the Debye-like behavior. The Curie temperature decreases with lower contents of Y^{3+} and increases at higher contents endorses presence of magnetic dilution in the A-B interaction consequent weakening magnetic strength that results the T_c to decline with the x contents. The value of saturation magnetization decreases with increasing Y^{3+} contents that indicates that the domain wall motion become tougher due to substitution of foreign Y^{3+} ions that possess larger ionic radius. Thus, for high resistivity and low losses, Y^{3+} substituted Co-Zn ferrites found to be useful in high frequency and power supply devices.

Acknowledgments The authors are grateful to the authority of Chittagong University of Engineering and Technology (CUET) for financial support. Authors are also thankful to Materials Science Division (MSD), Atomic Energy Centre, Dhaka (AECD) and Department of Glass and Ceramics Engineering (GCE), Bangladesh University of Engineering and Technology for their laboratory support for this work.

References

1. Alone, S.T., Shirsath, S.E., Kadam, R.H., Jadhav, K.M.: J. Alloys Compd. **509**, 5055–5060 (2011)
2. Vasoya, N.H., Lakhani, V.K., Sharma, P.U., Modi, K.B., Kumar, R., Joshi, H.H.: J. Phys. Condens. Matter. **18**, 8063 (2006)
3. Vanaja, M., Gnanajobitha, G., Paulkumar, K., Rajeshkumar, S., Malarkodi, C., Annadurai, G.: J. Nanostruct. Chem. **3**, 17 (2013)
4. Jacob, B.P., Thankachan, S., Xavier, S., Mohammed, E.M.: J.Alloy. Compd. **578**, 314–319 (2013)
5. Iqbal, M.A., Islam, M., Ali, I., Sadiq, I.: J. Alloy. Compd. **586**, 404–410 (2014)
6. Cai, X., Xu, B., Wang, J., Li, B., Wu, A., Wang, B., Gao, H., Yu, L., Li, Z.: J. Mater. Sci. Mater. Electron. **27**, 1328–1336 (2016)
7. Cai, X., Wang, J., Li, B., Wu, A., Xu, B., Wang, B., Gao, H., Yu, L., Li, Z.: J. Alloy. Compd. **657**, 608–615 (2016)
8. Rezlescu, N., Rezlescu, E., Pasnicu, C., Craus, M.L.: J. Phys. Condens. Matter. **6**, 5707–5716 (1994)
9. Pawar, R.A., Patange, S.M., Tamboli, Q.Y., Ramanathan, V., Shirsath, S.E.: Ceram. Int. **42**, 16096–16102 (2016)
10. Pawar, R.A., Desai, S.S., Patange, S.M., Jadhav, S.S., Jadhav, K.M.: Physica B. **S0921-4526**, 30019–30014 (2017)
11. Pradhan, A.K., Mandal, P.R., Bera, K., Saha, S., Nath, T.K.: Physica B: Physics of Condensed Matter. **S0921-4526**, 30571–30579 (2017)
12. Vara Prasad, B.B.V.S., Ramesh, K.V., Srinivas, A.: Structural and Soft Magnetic Properties of Nickel-Substituted Co-Zn Nanoferrites. JOSC, Accepted: 11 January 2018
13. Shinde, S.S.: Electrical properties of Co-Zn ferrite Doped with Silicon. Int. J. Cur. Res. Rev. **9**(9) (2017)
14. Bellad, S.S., Watave, S.C., Chougule, B.K.: J. Mater. Res. Bull. **34**, 1099 (1999)
15. Patil, R.S., Kakatkar, S.V., Sankapal, A.M., Sawant, S.R.: Ind. J. Pure Appl. Phys. **32**, 193 (1994)
16. Melagiriyappa, E., Jayanna, H.S., Chougule, B.K.: Mater. Chem. Phys. **112**, 68 (2008)
17. Ahmed, M.A., Okasha, N., Salah, L.: J. Magn. Magn. Mater. **264**, 241 (2003)
18. Jacobo, S.E., Duhalde, S., Bertorello, H.R.: J. Magn. Magn. Mater. **272-276**, 2253 (2004)
19. Alves, T.E.P., Pessoni, H.V.S., Franco, A.: Jr. Phys. Chem. Chem. Phys. **19**, 16395 (2017)
20. Ishaque, M., Khan, M.A., Ali, I., Athair, M., Khan, H.M., Iqbal, M.A., Islam, M.U., Warsi, M.F.: Mater. Sci. Semi. Proces. **41**, 508–512 (2016)
21. Jacobo, S.E., Bercoff, P.G.: Ceram. Int. **42**, 7664 (2016)
22. Ishaque, M., Khan, M.A., Ali, I., Khan, H.M., Iqbal, M.A., Islam, M.U., Warsi, M.F.: Ceram. Int. **41**, 4028 (2015)
23. Chakrabarty, S., Dutta, A., Pal, M.: J. Magn. Magn. Mater. **461**, 69 (2018)
24. AliM, A., Khan, M.N.I., Chowdhury, F.U.Z., Hossain, M.M., Hossain, A.K.M.A., Nahar, A., Hoque, S.M., Matin, M.A., Uddin, M.M.: Yttrium substituted Mg-Zn ferrites: correlation of physical properties with Yttrium content, to published. Submitted
25. Kumari, S., Kumar, V., Kumar, P., Kar, M., Kumar, L.: Adv. Powd. Tech. **26**, 213 (2015)
26. Rezlescu, N., Rezlescu, E., Popa, P.D., Rezlescu, L.: J. Alloys Compounds. **275–277**, 657–659 (1998)
27. Salah, L.M.: Phys. Status Solidi A. **203**(2), 271–281 (2006)
28. Nelson, J.B., Riley, D.: Proc. Phys. Soc. Lond. **57**, 160 (1945)
29. Hemeda, O.M., Barakat, M.M.: J. Magn. Magn. Mater. **223**, 127–132 (2001)
30. Mazen, S.A., Abdallah, M.H., Nakhla, R.I., Zaki, H.M., Metaw, F.: Mater. Chem. Phys. **34**, 35–40 (1993)
31. Smit, J., Wijn, H.P.J.: Ferrites. Wiley, NewYork (1959)
32. Rezlescu, N., Rezlescu, E., Sava, C.L., Tudorache, F., Popa, P.D.: Phys. Stat. Sol. (A). **201**, 17 (2004)
33. Gabal, A., Angari, Y.M.A.: J. Magn. Magn. Mater. **322**, 3159–3165 (2006)
34. ImageJ Software Link
35. Peng, Z., Fu, X., Ge, H., Fu, Z., Wang, C., Qi, L., Miao, H.: Effect of Pr^{3+} doping on magnetic and dielectric properties of Ni–Zn ferrites by "one-step synthesis". J. Mag. Magn. Mater. **323**, 2513–2518 (2011)
36. Fu, X.L., Ge, H.L., Xing, Q.K., Peng, Z.J.: Mater. Sci. Eng. B. **176**, 926–931 (2011)
37. Jonscher, A.K.: Nature (London). **267**, 673 (1977)
38. Koops, C.G.: Phys. Rev. **83**, 121 (1951)
39. Maxwell, J.C.: Electricity and magnetism, New York. Oxford University Press (1973)
40. Wagner, K.W.: Am. Phys. **40**, 317 (1973)
41. Katsmi, K., Mamoru, S., Tatrsuo, I., Katsuya, I.: Bull. Chem. Soc. **48**, 1764 (1975)
42. El-Hiti, M.A.: J. Magn. Magn. Mater. **192**, 305 (1999)

43. Mansour, S.F., Abdo, M.A., El-Dek, S.I.: J. Magn. Magn. Mater. **422**, 105 (2017)
44. Hashim, M., Meena, S.S., Kotnala, R.K., Shirsath, S.E., Bhatt, P., Kumar, S., Şentürk, E., Kumar, R., Alimuddin, A., Gupta, N.: J. Magn. Magn. Mater. **360**, 21 (2014)
45. Ali, M.A., Uddin, M.M., Khan, M.N.I., Chowdhury, F.U.Z., Hoque, S.M.: J. Magn. Magn. Mater. **424**, 148 (2017)
46. Ali, M.A., Khan, M.N.I., Chowdhury, F.U.Z., Akhter, S., Uddin, M.M.: J. Sci. Res. **7**, 65 (2015)
47. Verma, K., Kumar, A., Varshney, D.: Curr. Appl. Phys. **13**, 467 (2013)
48. Murthy, V.R.K., Sobhanadri, J.: Phys. Status Solidi A. **36**, K133 (1976)
49. Macdonald, J.R.: Impedance Spectroscopy: Emphasizing Solid State Material and Systems. Wiley, NewYork (1987)
50. Padmasree, K.P., Kanchan, D.D., Kulkami, A.R.: Solid State Ionics. **177**, 475 (2006)
51. Sinclair, D.C., West, A.R.: J. Appl. Phys. **66**, 3850 (1989)
52. Pachpinde, A.M., Langade, M.M., Lohar, K.S., Patange, S.M., Shirsath, S.E.: Chem. Phys. **429**, 20–26 (2014)
53. Lwin, N., Othman, R., Sreekantan, S., Fauzi, M.N.A.: J. Magn. Magn. Mater. **385**, 433–440 (2015)
54. Gul, I.H., Abbasi, A.Z., Amin, F., Anis-ur-Rehman, M., Maqsood, A.: J. Magn. Magn. Mater. **311**, 494–499 (2007)
55. Shirsath, S.E., Toksha, B.G., Jadhav, K.M.: Mater. Chem. Phys. **117**(1), 163–168 (2009)
56. Fan, X.F., Ren, H.P., Zhang, Y.H., Guo, S.H., Wang, X.L.: Rare Metals. **27**, 287–291 (2008)
57. Dunn, I.H., Jacobo, S.E., Bercoff, P.G.: J. Alloys Compd. **691**, 130–137 (2016)